ANKARA YILDIRIM BEYAZIT UNIVERSITY

GRADUATE SCHOOL OF NATURAL AND APPLIED SCIENCES



EXPERIMENTAL AND FINITE ELEMENT ANALYSIS OF RESIDUAL STRESSES IN COLD TUBE DRAWING WITH A FIXED MANDREL FOR AISI 1010 STEEL

Ph.D. Thesis by

JABBAR KASIM JABBAR GATTMAH

Department of Mechanical Engineering

May, 2017

ANKARA

EXPERIMENTAL AND FINITE ELEMENT ANALYSIS OF RESIDUAL STRESSES IN COLD TUBE DRAWING WITH A FIXED MANDREL FOR AISI 1010 STEEL

A Thesis Submitted to

The Graduate School of Natural and Applied Sciences of

Ankara Yıldırım Beyazıt University

In Partial Fulfillment of the Requirements for the Degree of Doctor of Philosophy in Mechanical Engineering, Department of Mechanical Engineering

by

Jabbar Kasim Jabbar GATTMAH

May, 2017

ANKARA

Ph.D. THESIS EXAMINATION RESULT FORM

We have read the thesis entitled **"EXPERIMENTAL AND FINITE ELEMENT ANALYSIS OF RESIDUAL STRESSES IN COLD TUBE DRAWING WITH A FIXED MANDREL FOR AISI 1010 STEEL"** completed by **JABBAR KASIM JABBAR GATTMAH** under supervision of **PROF. DR. SADETTİN ORHAN** and Co-supervisor **ASSOC. PROF. DR. FAHRETTİN ÖZTÜRK** and we certify that in our opinion it is fully adequate, in scope and in quality, as a thesis for the degree of Doctorate of Philosophy in Mechanical Engineering.

Prof. Dr. Sadettin ORHAN	Assoc. Prof. Dr. Fahrettin ÖZTÜRK
(Supervisor)	(Co-Supervisor)
Prof. Dr, Adem ÇİÇEK	Prof. Dr, Mehmet Ali GÜLER
(Jury Member)	(Jury Member)
Prof. Dr, Zafer EVİS	Prof. Dr, Ömer KELEŞ
(Jury Member)	(Jury Member)

Prof. Dr. Fatih V. ÇELEBİ

(Director)

Graduate School of Natural and Applied Sciences

ETHICAL DECLERATION

I hereby declare that, in this thesis which has been prepared in accordance with the Thesis Writing Manual of Graduate School of Natural and Applied Sciences,

- All data, information and documents are obtained in the framework of academic and ethical rules,
- All information, documents and assessments are presented in accordance with scientific ethics and morals,
- All the materials that have been utilized are fully cited and referenced,
- No change has been made on the utilized materials,
- All the works presented are original,

and in any contrary case of above statements I accept to renounce all my legal rights.

ACKNOWLEDGMENTS

I would like to thanks to my supervisor Prof. Dr. Sadettin Orhan for his guidance, support and valuable comments for this thesis study. I am grateful to my co-supervisor Assoc. Prof. Dr. Fahrettin Ozturk for his endless effort, support, and guidance to make this work perfect, without him this study would never come to life.

I also would like to thank to Ankara Yıldırım Beyazıt University Staff especially to Prof. Dr. Fatih Vehbi Çelebi who had great help and support during my Ph.D. study.

My sincere thanks are for Prof. Dr. Adem Çiçek for his help during construction of the experimental set-up. Many thanks to Asst. Prof. Dr. Fatih Göncü for his help in finite element modelling.

I also would like to thank to Dr. Serkan Toros for his help during the completion of practical experiments and simulation models.

Many thanks to Antes Company Staff to help in the experimental setup and the tube production.

I would like to thank to my family for their continuous support to complete my Ph.D. study. Thanks again to my family to understand my madness and to leave me by myself during the last painful months.

I would also like to thank to my close friend Dr. Asaad Al-shouk for his support, sincere conservations, and endless smiling face.

Finally, I would like to thank to my dear wife Rana Mahdi for her all support, patience, and lifelong love. It is her love that makes everything possible for me.

This study is supported by Graduate School of Natural Sciences at Ankara Yıldırım Beyazıt University under BAP project # 2641.

2017, 16 May **Jabbar Kasim Jabbar GATTMAH**

EXPERIMENTAL AND FINITE ELEMENT ANALYSIS OF RESIDUAL STRESSES IN COLD TUBE DRAWING WITH A FIXED MANDREL FOR AISI 1010 STEEL

ABSTRACT

In this thesis, analysis of tube drawings with a fixed mandrel and residual stress measurements inside the tube wall are made. Dies and mandrels were designed and manufactured to produce AISI 1010 steel tubes at the reduction of areas of R=16% and 23%. Tube drawing was efficiently performed under lubricated conditions by a bench chain-driven cold drawing machine. Some of the most common defects that occur through the cold tube drawing process are non uniform, undesired deformations of the material. Determining residual stress inside the tube wall is quite important in order to decide the final quality of the product. In this study, various measurement methods are utilized to measure residual stresses. Besides a new innovative technique with using removing layer method (RLM) is developed to measure residual stress within the tubular shape. The RLM using milling process is performed on the inner and outer surfaces of the tubes while measuring the developed strains at the outer and the inner surfaces, respectively. The slitting method (SM) is proposed to determine the residual stress in one direction while X-Ray diffraction (XRD) are used to identify residual stresses at five orientations below the inner and the outer surfaces of the tube. A finite element model (FEM) with an axisymmetry is developed to evaluate drawing force vs. displacement and residual stress according to the distance from the outer to the inner surfaces. The FEM is also improved to determine optimum drawing parameters that may lead to minimized drawing stress. The results of the experimental approach are shown to be in good agreement and the RLM is the most appropriate method to measure residual stresses inside the tube wall. The results showed that residual stresses present inside the tube wall are completely different for R=16% and 23%.

Keywords: AISI 1010 steel tube, Cold tube drawing, Residual stress, Removing layer method (RLM), Slitting method (SM), X-Ray diffraction (XRD), Finite element method (FEM).

AISI 1010 ÇELİĞİNİN SABİT MANDREL İLE SOĞUK BORU ÇEKME İŞLEMİNDE OLUŞAN KALINTI GERİLMELERİNİN DENEYSEL VE SONLU ELEMANLAR ANALİZİ

ÖZET

Bu tezde sabit mandrel ile boru çekme işleminin analizi ve boru cidarı içindeki kalıntı gerilmelerin ölçümleri yapılmıştır. AISI 1010 çelik boruları 16% ve 23% kesit daralmalarında çekmek için kalıplar tasarlanmış ve mandreller imal edilmiştir. Boru çekme işlemi yağlı olarak zincir tahrikli soğuk çekme makinesi ile etkili bir şekilde gerçekleştirilmiştir. Boru çekme işlemi sırasında karşılaşılan bazı çok yaygın kusurlar, düzensiz (non uniform), istenmeyen malzeme deformasyonlarıdır. Ürünün son kalitesine karar verebilmek için boru cidarı içindeki kalıntı gerilmesini belirlemek oldukça önemlidir. Bu çalışmada, kalıntı gerilmelerini ölçmek için farklı ölçüm metotları kullanılmıştır. Bunun yanında, kalıntı gerilmelerini ölçmek için borunun içinde tabaka kaldırma metodunu (RLM) kulanan yenilikçi bir teknik geliştirilmiştir. Borunun dış ve iç yüzeylerinde oluşan birim deformasyonlar frezede RLM yöntemi kullanılarak borunun iç ve dış yüzeylerinde sırasıyla ölçülmüştür. Tek yönde kalıntı gerilmesini belirlemek için yarma metodu (SM) kullanılırken boru cidarı içinde olduğu gibi, boru iç ve dış yüzeylerinin altında beş konumda kalıntı gerilmesini ölçmek için X-Işını kırınımı (XRD) kullanılmıştır. Yer değiştirmeye karşılık, çekme kuvvetini ve kalıntı gerilmelerini dış yüzeyden iç yüzeydeki bir mesafeye göre belirlemek için simetrik eksenli sonlu eleman modeli (FEM) geliştirilmiştir. Oluşturulan model çekme gerilmesinin azalmasına neden olan optimum çekme parametrelerini belirlemek için de iyileştirilmiştir. Deney sonuçlarının iyi bir uyum içinde olduğu ve boru cidarı içindeki kalıntı gerilmelerini ölçmek için ise RLM metodunun en iyi metot olduğu görülmüştür. Sonuçlar, R=16% ve 23% kesit daralmalarında borunun iç yüzeyinde kalıntı gerilmelerinin tamamen farklı olduğunu göstermiştir.

Anahtar Kelimeler: AISI 1010 çelik boru, Soğuk boru çekme, Kalıntı gerilmesi, Tabaka kaldırma metodu (RLM), Yarma metodu (SM), X-Işını kırınımı (XRD), Sonlu eleman metodu (FEM).

TABLE OF CONTENTS

Ph.D THESIS EXAMINATION RESULT FORM……..…….…….....ii
ETHICAL DECLERATION……iii
ACKNOWLEDGMENTS iv
ABSTRACT v
ÖZET vi
TABLE OF CONTENTS vii
LIST OF TABLES xi
LIST OF FIGURES xiii
NOMENCLATURE xviii
LIST OF ABBREVIATIONS xxii

CHAPTER 1- INTRODUCTION 1
1.1 Background 1
1.2 Definition of the Problem Statement 1
1.3 Thesis Objectives and Contributions 3
1.4 Scope of the Thesis 5

CHAPTER 2- TUBE DRAWING, RESIDUAL STRESSES, AND LITERATURE REVIEW 6
2.1 Introduction 6
2.2 Tube Drawing Processes 6
2.2.1 Tube Drawing without a Mandrel (Tube Sinking) 7
2.2.2 Tube Drawing with a Fixed Mandrel (Fixed Plug) 7
2.2.3 Tube Drawing with a Floating Plug 8
2.2.4 Tube Drawing with a Moving Mandrel 9
2.3 Tools and Machines of Tube Drawing with a Fixed Mandrel 9
2.3.1 Tube Drawing Die 9
2.3.2 Fixed Mandrel Tube Drawing 10
2.3.3 Bench Machine Tube Drawing 11
2.4 Parameters Affecting the Tube Drawing Process with a Fixed Mandrel 11
2.4.1 Reduction of Tube Area 11
2.4.2 Nib Die Geometry 12

2.4.3 Mandrel Geometry (Plug Geometry) 13
2.4.4 Drawing Speed 13
2.4.5 Lubrication 13
2.5 Phenomena that Occur During Tube Drwaing Process with a Fixed Mandrel 14
2.5.1 Plasticity 14
2.5.1.1 Isotropic and Anisotropic Yield Functions 15
2.5.1.2 Flow Rule 15
2.5.1.3 Hardening Constitutive Equations 16
2.5.2 Friction 16
2.5.3 Heat Generation 18
2.6 Analysis of Tube Drawing Process with a Fixed Mandrel 19
2.6.1 Analytical Methods 19
2.6.2 Finite Element Method (FEM) 20
2.6.2.1 Introduction to FEM 20
2.6.2.2 Axisymmetric Finite Element Model (AFEM) 21
2.7 Residual Stresses 22
2.7.1 Destructive Technique 23
2.7.2 Semi Destructive Technique 23
2.7.3 Non Destructive Technique 24
2.8 Literature Review 25
2.8.1 Literature Review of Tube Drawing Process 25
2.8.2 Literature Review of Residual Stress inside Tube Wall 31

CHAPTER 3- EXPERIMENTS: TESTS, MEASUREMENTS, AND PROCEDURES 38
3.1 Introduction 38
3.2 Raw Material of AISI 1010 Steel Tube 38
3.2.1 Spectral Test 39
3.2.2 Tensile Test 39
3.2.3 Macro Hardness Test 40
3.3 Designing and Manufacturing of Tools Tube Drawing with a Fixed Mandrel 41
3.3.1 Dies 41
3.3.2 Mandrels 42
3.4 Experimental of Tube Drawing Process with a Fixed Mandrel 44

3.5 Residual Stress Measurement within Tube Wall Thickness Using Destructive Technique (The RLM and The SM Methods) 49
3.5.1 TRSG for the Determine Residual Stress 49
3.5.1.1 Surface Sample Preparation..... 52
3.5.1.2 Attaching of the TRSG on the Bonding Area 53
3.5.1.3 Soldering Extension Lead Wires with the TRSG..... 54
3.5.1.4 Insulating and Covering of the TRSG 55
3.5.1.5 Connecting Extension Lead Wires with Data Logger Device..... 56
3.5.2 Residual Stress Measurement Using Milling Process..... 57
3.5.2.1 Residual Stress Measurement by the RLM to Mill Layers from the Inner and the Outer Surfaces of the Tube Wall..... 58
3.5.2.2 Residual Stress Measurement by the SM Using Milling Process 61
3.6 Residual Stress Measurement Using Non Destructive Technique by XRD Method 63

CHAPTER 4- FINITE ELEMENT SIMULATION BY ABAQUS..... 67
4.1 Introduction..... 67
4.2 Axisymmetric Tube Drawing with a Fixed Plug Model..... 67
4.2.1 Geometrical and Material Model 68
4.2.2 Assembly of Model and Step 71
4.2.3 Interaction and Boundary Conditions 73
4.2.4 Element and Mesh..... 74
4.3 Three Dimension Tube Drawing with a Fixed Plug Model..... 77

CHAPTER 5- RESULTS AND DISCUSSION 79
5.1 Introduction..... 79
5.2 Chemical Composition Results..... 79
5.3 Tensile Test Results 81
5.4 Macro Hardness Results..... 82
5.5 Results of Compression and Drawing Force with Displacement..... 82
5.5.1 Experimental and FEM Results of Force with Displacement by Compression Process 83
5.5.2 FEM Results of Force with Displacement by Drawing Process..... 86
5.6 Residual Stress Results within the Tube Wall 89

5.6.1 Results of Residual Stress by the RLM 89
5.6.2 Results of Residual Stress by the SM 95
5.6.3 Results of residual Stress by the XRD 97
5.6.4 Results of Residual Stress by the FEM 100
5.7 Comparison of Residual Stress Results 104
5.7.1 Axial Residual Stress by the FEM and the RLM 104
5.7.2 Hoop Residual Stress by the FEM, the SM, the RLM, and the XRD 106
5.8 Results of Optimum Parameters for Drawing Process by the FEM 109
5.8.1 Effect Semi Die/Plug Angles on Plastic Deformations 109
5.8.2 Effect Semi Die Angle on Drawing Force 110
5.8.3 Effects Semi Die Angle on Drawing Stress at Different Coefficients of Friction 111
5.8.4 Effects Semi Plug Angles on Drawing Stress at Different Coefficients of Friction 113

CHAPTER 6- CONCLUSION AND FUTURE WORKS 114
6.1 Conclusion 114
6.2 Future Works 116

REFERENCES 118

APPENDICES 126
Appendix A- S9 Atlantis Device for the Spectral Test 127
Appendix B- Macro Hardness Tester with Cross Slide (Q250) 128
Appendix C- Reduction of Areas Calculation 129
Appendix D- Tee Rosette Strain Gage (TRSG) 130
Appendix E- Data Logger Device (Dewe 43 A) 131
Appendix F- Multipurpose XRD System (Ultima IV) 132
Appendix G- Material Properties of AISI 1010 Steel 134
Appendix H- Stable Time Increment Calculation 136
Appendix I- Energy Output Using ABAQUS 138
Appendix J- Effect the Velocity on Drawing Force 143
Appendix K- External Work Calculations for the Compression Process 144

CURRICULUM VITAE (CV) 147

LIST OF TABLES

Table 3.1 Dimensions for two dies 42

Table 3.2 Dimensions for two mandrels 43

Table 3.3 Rotations of Ψ°and 2θ° axes 66

Table 4.1 Simulation model units 67

Table 4.2 Mechanical properties of AISI 1010 steel 70

Table 4.3 Mechanical properties of cemented carbide 70

Table 5.1 Chemical composition of AISI 1010 steel tube 80

Table 5.2 Macro hardness results 82

Table 5.3 Results of average axial microstran by the RLM from the outer to the inner surface for R=16 90

Table 5.4 Results of average axial microstran by the RLM from the inner to the outer surface for R=16% 90

Table 5.5 Results of average hoop microstran by the RLM from the outer to the inner surface for R=16% 91

Table 5.6 Results of average hoop microstran by the RLM from the inner to the outer surface for R=16% 91

Table 5.7 Results of average axial microstran by the RLM from the outer to the inner surface for R=23% 92

Table 5.8 Results of average axial microstran by the RLM from the inner to the outer surface for R=23% 92

Table 5.9 Results of average hoop microstran by the RLM from the outer to the inner surface for R=23% 93

Table 5.10 Results of average hoop microstran by the RLM from the inner to the outer surface for R=23% 93

Table 5.11 Results of average hoop microstran by the SM for R=16% 96

Table 5.12 Results of average hoop microstran by the SM for R=23% 96

Table 5.13 Results of relative drawing stress for all simulations 112

Table (A) Specifications of Q250 128

Table (B) Specifications of TRSG 130

Table (C) Specifications of Dewe 43 A 131

Table (D) Specifications of Ultima IV 133

Table (E.1) Chemical composition of the AISI 1010 carbon steel 134

Table (E.2) Mechanical properties of the AISI 1010 carbon steel 134

Table (E.3) Thermal properties of the AISI 1010 steel 134

Table (E.4) True stress, true total strain, and effective plastic strain of the AISI 1010 steel..... 135

Table (F) Force and displacement values for five point..... 144

LIST OF FIGURES

Figure 2.1 Tube drawing without a mandrel (tube sinking)..... 7
Figure 2.2 Tube drawing with a fixed mandrel (fixed plug drawing)..... 8
Figure 2.3 Tube drawing with a floating plug..... 8
Figure 2.4 Tube drawing with a moving mandrel..... 9
Figure 2.5 Tube drawing die..... 10
Figure 2.6 Fixed mandrel tube drawing (cylindrical plug)..... 10
Figure 2.7 Tube drawing by a bench machine[4]..... 11
Figure 2.8 Nib die geometry..... 12
Figure 2.9 Conical plug geometry..... 13
Figure 2.10 Description of frictional contact for tube drawing with a fixed cylindrical mandrel..... 18
Figure 2.11 Strains and corresponding stresses in an axisymmetric solid..... 22
Figure 2.12 Tangential strain in an axisymmetric model..... 22
Figure 2.13 Meshes of the tube made by Superform software [41]..... 26
Figure 2.14 Straight and stepped mandrel geometry [42]..... 26
Figure 2.15 Tubes production according to the redesigned drawing [43]..... 27
Figure 2.16 The sinker and the die drawing with a fixed mandrel..... 28
Figure 2.17 (a) Machine that draws the tube, and (b) lubrication procedure [48]..... 29
Figure 2.18 (a) Hollow sinking process, and (b) mandrel drawing process..... 30
Figure 2.19 Tube drawing process by a conical mandrel..... 30
Figure 2.20 Arc-type and Bezier curve-type drawing dies..... 31
Figure 2.21 A lath machine to measure residual stress by saw mounted [54]..... 32
Figure 2.22 Deformed tube by residual stress after slitting (a) Schematic illustration of slits, (b) without a plug sample, (c) with a plug sample, and (d) curvature calculation [56]..... 33
Figure 2.23 Strain gages bonding fixed on the outer surface of the tube [57]..... 33
Figure 2.24 Residual stress procedure by the ND of SF-copper tube [59]..... 34
Figure 2.25 (a) Point measurement, and (b) measuring points over circumference [61]..... 35
Figure 2.26 Metal ring that is harmed due to the residual stress [62]..... 36
Figure 2.27 Directions of the internal stresses inside tube wall..... 36
Figure 2.28 Residual stress measurement by ND on the forming zone [64]..... 37
Figure 3.1 (a) Raw material of tube and (b) the spectral test..... 39
Figure 3.2 Sample dimensions of tensile test..... 40

Figure 3.3 Macro hardness test of the raw material 40
Figure 3.4 Section of die drawing 41
Figure 3.5 Picture of die drawing produced outer diameter of 76 mm tube 42
Figure 3.6 Section of the fixed straight mandrel 43
Figure 3.7 Picture of the mandrel with outer plug diameter 70 mm 44
Figure 3.8 Schematic representation of the die support, die, tube, and mandrel 45
Figure 3.9 Picture of die located in the die support 46
Figure 3.10 Pictures of mandrel tolerance for the nib die with die support 46
Figure 3.11 Pictures of initial tube covered by the commercial mineral oil 46
Figure 3.12 Pictures of the chain driven cold tube drawing process 47
Figure 3.13 Die and plug setup for compression process 47
Figure 3.14 Compression test to measure force 48
Figure 3.15 Tube samples after the compression (a) R=16% and (b) R=23% 48
Figure 3.16 Cleaning bonded area with M-prep conditioner A and M-prep neutralizer 5A 52
Figure 3.17 Bonding areas after the cleaning for both of external and internal surfaces of tube 53
Figure 3.18 TRSG bonded by transparent sticker then by M-Bond 200 adhesive. 53
Figure 3.19 Final bonding for the TRSG at the outer and the inner surfaces of tube 54
Figure 3.20 Soldering extension lead wires with the TRSG at the outer and the inner surfaces of tube 54
Figure 3.21 TRSG covered by M-coat A 55
Figure 3.22 TRSG covered by DOW CORNING 3145 RTV MIL-A-46146 56
Figure 3.23 Data logger device (DEWE 43 A) [66] 56
Figure 3.24 Connections of the wires and two bridges with a data logger device 57
Figure 3.25 Removing layer from the inner surface of tube 58
Figure 3.26 Removing layer from the outer surface of tube 58
Figure 3.27 Cutting tool for the inner and the outer surfaces of the tube 59
Figure 3.28 The RLM by internal milling using CNC machine to measure strain 60
Figure 3.29 The RLM by external milling using CNC machine to measure strain 60
Figure 3.30 Measurement system of axial and hoop strain by data logger 61
Figure 3.31 Slitting method according to the TRSG 61
Figure 3.32 Carbide milling cutter with 4 mm diameter 62
Figure 3.33 The SM using CNC milling machine 62
Figure 3.34 Preparing samples for XRD measurements 63

Figure 3.35 Sample positioned in the X-Ray holder machine 64
Figure 3.36 XRD stress measurement inside the tube wall. (a) Ψ=0, (b) $\Psi \neq$ 0..... 65
Figure 4.1 Axisymmetric dimensions of nib die by ABAQUS at R=23% 68
Figure 4.2 Axisymmetric dimensions of plug by ABAQUS at R=23% 69
Figure 4.3 Axisymmetric dimensions of initial tube by ABAQUS 69
Figure 4.4 Assembly of the AFEM (the nib die, the plug, and the initial tube)..... 71
Figure 4.5 Adaptive mesh with adaptive mesh controls options in ABAQUS..... 72
Figure 4.6 Boundary condition of the AFEM 74
Figure 4.7 Finite elements meshing of the AFEM..... 74
Figure 4.8 Mesh sensitivity analysis by axial stress at 0.75 s 75
Figure 4.9 Mesh sensitivity analysis by hoop stress at 0.75 s..... 75
Figure 4.10 Energy output by ABAQUS for R=23% 76
Figure 4.11 Kinetic energy by ABAQUS for R=23% 76
Figure 4.12 3DFEM meshing of the nib die at R=23% 77
Figure 4.13 3DFEM meshing of the plug at R=23% 78
Figure 4.14 3DFEM meshing of the initial tube 78
Figure 5.1 Eng. stress vs. eng. strain of AISI 1010 steel tube..... 81
Figure 5.2 True stress vs. effective plastic strain plot of AISI 1010 steel tube..... 82
Figure 5.3 Von mises stress distribution by compression process (a) R=16% and (b) R=23% 83
Figure 5.4 Comparison between the experiment and the FEA at R=16% for the compression process..... 84
Figure 5.5 Comparison between the experiment and the FEA at R=23% for the compression process..... 85
Figure 5.6 PEEQ contours by compression process (a) R= 16% and (b) R=23%.... 85
Figure 5.7 Max. principal stress distribution (a) AFEM and (b) 3DFEM 86
Figure 5.8 Min. principal stress distribution (a) AFEM and (b) 3DFEM..... 86
Figure 5.9 Plots of drawing force vs. displacement obtained numerically 88
Figure 5.10 PEEQ contours by drawing process (a) R= 16% and (b) R=23%..... 88
Figure 5.11 Residual stress measurement of final tube by RLM at R=16%..... 94
Figure 5.12 Residual stress measurement of final tube by RLM at R=23%..... 95
Figure 5.13 Hoop residual stress measurement of final tube by the SM 97
Figure 5.14 Hoop residual stress measurements by the XRD below of the inner surface of the tube at R=16% 98

Figure 5.15 Hoop residual stress measurements by the XRD below of the inner surface of the tube at R=23% 99

Figure 5.16 Residual stress measurements of final tube by the XRD 100

Figure 5.17 Distribution of the axial stress during the drawing process at R=16% by the FEM 101

Figure 5.18 Distribution of the hoop stress during the drawing process at R=16% by the FEM 101

Figure 5.19 Distribution of the axial stress during the drawing process at R=23% by the FEM 102

Figure 5.20 Distribution of the hoop stress during the drawing process at R=23% by the FEM 102

Figure 5.21 Residual stress of final tube by the FEM at R=16% 103

Figure 5.22 Residual stress of final tube by the FEM at R=23% 104

Figure 5.23 Comparison between the FEM and the RLM according to the axial residual stress at R=16% 105

Figure 5.24 Comparison between the FEM and the RLM according to the axial residual stress at R=23% 106

Figure 5.25 Comparison between the FEM, the SM, the RLM, and the XRD according to the hoop residual stress at R=16% 107

Figure 5.26 Comparison between the FEM, the SM, the RLM, and the XRD according to the hoop residual stress at R=23% 108

Figure 5.27 PEEQ axisymmetric finite element models at semi die angle of 12° and semi plug angle of 0° 109

Figure 5.28 PEEQ axisymmetric finite element models at semi die angle of 7° and semi plug angle of 4° 110

Figure 5.29 Relationship between drawing force and displacement at different semi die angles 111

Figure 5.30 Relationship between the drawing stress and the semi die angle at different friction coefficients 112

Figure 5.31 Relationship between the drawing stress and the semi plug angle at different friction coefficients 113

Figure (A) S9 Atlantis 127

Figure (B) 250Q Macro hardness tester 128

Figure (C) TRSG 130

Figure (D) Ultima IV 133

Figure (E) Smallest element dimension for R=23% model 136

Figure (F.1) Dimensions of axisymmetric for the initial tube 138

Figure (F.2) Energy output for R=16% 139

Figure (F.3) Kinetic energy for R=16%..... 139
Figure (F.4) External work for R=16%..... 140
Figure (F.5) Energy obtained by force and displacement integration for R=16%.. 140
Figure (F.6) Energy output for R=23%..... 141
Figure (F.7) Kinetic energy for R=23%..... 141
Figure (F.8) External work for R=23%..... 142
Figure (F.9) Energy obtained by force and displacement integration for R=23%.. 142
Figure (G) Effect the velocity on drawing force for R=16%..... 143
Figure (H.1) Force vs. Displacement of R=16 % obtained experimentally by compression process..... 144
Figure (H.2) Comparsion between FEM and EXP according to the external work at R=16% 146
Figure (H.3) Comparsion between FEM and EXP according to the external work at R=23% 146

NOMENCLATURE

Roman Letter Symbols

A_f	Cross section area of the final tube
A_i	Cross section area of the initial tube
b	Width of the nut for the mandrel
b_1	Diameter of the bolt for the mandrel
cd	The dilatational wave speed
d	The lattice spacing of crystal planes
d_o	Lattice spacing with stress free
d_1	Hole diameter of the nib die
d_2	Outer diameter of the nib die
d_3	Outer diameter of the die block
$d_{\emptyset\Psi}$	Spacing between the lattice planes measured
$d\lambda$	A scalar coefficient
D_o	Outer diameter of the tube before drawing
D_i	Outer diameter of the tube after drawing
E	Young's modulus
E_v	Exciting voltage
E_y	Modulus at yield
f	Dissipative potential for same yield function
f_y	Isotropic yield function
F_{dr}	Drawing force
F_n	Normal force
F_t	Tangential force
g	Dissipative potential for different yield function
h	Thickness of the nib die
hkl	Family of crystalline planes
H%	Reduction of tube thickness
i	Length of nut
I_1	Exit length of the nib die
I_2	Bearing length of the nib die
I_3	Die block length from the nib die

K	Strength coefficient
K_f	Gage factor
L_{min}	Smallest element dimension in the mesh
m	Mass of part
m_1	Outer plug diameter
m_2	Rod diameter of the mandrel
m_3	Inner plug diameter
n	An integer denoting the order of diffraction
n	Strain hardening
N	Normal direction to the surface
t	Thickness of die block
t_i	Wall thickness of tube after drawing
t_m	Wall thickness of tube after polishing
t_o	Wall thickness of the tube before drawing
p	Penetration depth
P_f	Power of friction
q	Contact length
R	Radius of the nib die entry
R_g	Gage resistance
R_o	Resistance before strain generation
R_1	Resistance section1 of TRSG
R_2	Resistance section2 of TRSG
R%	Reduction of cross section area of the tube
S	X-ray source
u	Displacement
v	Poisson's ratio
V	Volume of part
V	Velocity of drawing
z_1	Fillet of nut
$\mathrm{z}_1 + \mathrm{z}_2$	Length of screw
z_3	Length of plug
z_4	Length of rod for the mandrel
$(e_{eff})_{plastic}$	Effective plastic strain

e_{eng}	Engineering strain
$(e_{true})_{total}$	True strain

Greek Letter Symbols

β	Ratio of the thermoplastic heating
ϵ_o	Prior deformation
ϵ_p	Plastic strain
ϵ_{11}	Parallel strain
ϵ_{33}	Strain out of plane perpendicular
$\dot{\epsilon_p}$	Plastic strain rate
ϵ_{ij}^{P}	Plastic strain rate component
$\epsilon_{\emptyset\Psi}$	Strain measured by XRD
ε	Strain measured
$\varepsilon_\theta, \varepsilon_{rr}, \varepsilon_{zz}$	Components of strain
μ	Friction coefficient
μ_1	Friction coefficient between metal and nib die
μ_2	Friction coefficient between metal and plug
σ	Stress component
σ_d	Drawing stress
σ_{eng}	Engineering stress
σ_{ij}	Principal stresses with i and j equal (1, 2, 3)
σ_o	Material yield stress
σ_r	Relative drawing stress
σ_{true}	True stress
σ_{xx}	Stress measured with x direction
σ_y	Yield stress in stress in uniaxial tension
σ_{yy}	Stress measured with y direction
$\sigma_1, \sigma_2, \sigma_3$	Principal stresses
$\sigma_\emptyset$	Surface stress at any direction
$\sigma_\theta, \sigma_{rr}, \sigma_{zz}$	Stress components
$(\sigma_n)_d$	Normal stress due to friction between nib die and metal
$(\sigma_n)_p$	Normal stress due to friction between plug and metal
$(\sigma_t)_d$	Tangential stress due to friction between nib die and metal

$(\sigma_t)_p$	Tangential stress due to friction between plug and metal
ρ	Density of material
δ	Radial of spring-back
$\emptyset$	Angle surface of sample
τ	Shear stress
τ_{zr}	Shear stress in *z* and *r* directions
$\vec{v}_s$	Sliding velocity
γ_{zr}	Shear strain in *z* and *r* directions
λ	X-ray wavelength
Ψ	Tilt angle between the normal to the diffracting lattice planes and sample surface
α	Semi die angle
αp	Semi plug angle
Δt	Stable time increment
$\dot{Q}_p$	Thermoplastic heat
$\dot{W}_p$	Plastic work rate
Δe	Output voltage due to the strain
ΔR	Resistance change due to the strain
2β	Inner die block angle
2θ	High diffraction angle from the surface of a stressed sample for two orientations of the sample relative to the X-ray beam
2α	Die drawing angle
2γ	Exit die angle
2∂	Outer block angle

LIST OF ABBREVIATIONS

AFEM	Axisymmetric finite element model
ALE	Arbitrary lagrangian-eulerian
ALLIE	Internal energy according to the ABAQUS output
ALLKE	Kinetic energy according to the ABAQUS output
ALLWK	External work according to the ABAQUS output
BRSLM	Block removal/splitting/layering method
CDV	Critical damage value
CM	Contour method
CHD	Center hole drilling
DHD	Deep hole drilling
EDM	Electric discharge method
FEM	Finite element method
HDM	Homogenous deformation method
MBN	Magnetic Barthausen noise
ND	Neutron diffraction
PEEQ	Equivalent plastic strain
RC	Ring core
RLM	Removing layer method
SBM	Sach's boring method
SD	Synchrotron diffraction
SDM	Slab drawing method
SEM	Scanning electron microscopy
SGR	Strain gage rosette
SIS	Steering input shaft
SM	Slitting method
TRSG	Tee rosette strain gage
UBT	Upper bound theory
UTS	Ultimate tensile strength
XRD	X-ray diffraction
YS	Yield strength
3DFEM	Three-dimension finite element method

CHAPTER 1

INTRODUCTION

1.1 Background

Tube products have widely been used in many applications such as water and oil transportation, heating and cooling systems, buildings, and components of vehicles. Qualities of tube products depend on many factors in manufacturing including reduction of area, die and plug geometries, velocity, and lubrication.

There are several types of manufacturing operations to produce the tubes such as casting, piercing, rolling, bending or extrusion. These manufacturing methods have restricted usefulness and clear limitations in terms of tube production, while a drawing process enables the production of longer tubes with thinner walls, smaller diameters, better surface finish, more precise dimensional tolerances, better mechanical properties, more diverse final shapes of the product, and more diverse final diameters and thicknesses from end to end. The quality of tube products and obtaining a good surface finish of the outer and the inner walls represent big challenges in cold tube drawing processes.

There are various types of tube drawing processes; a cold tube drawing process with a fixed mandrel (plug) is used to produce tubes where the outside is formed by a drawing die hole and the inside by a plug or a rod. Therefore, the best products can easily be produced with a good design and manufacture of both the dies and the mandrels, as well as through appropriate choice of lubricants and drawing velocity.

1.2 Definition of the Problem Statement

The tube drawing process is one of the most significant metal forming processes used to produce tubes with accurate dimensions. Tube drawing with a fixed mandrel (plug) is used to ensure obtaining a good product with the best possible inner and outer surfaces. Metal forming processes commonly generate a non homogeneous deformation in the workpiece, thus the final product contains residual stress patterns.

In tube drawing with a fixed mandrel, there are different phenomena that occur due to the drawing force applied to draw the metal to the forming zone. First, during the forming process, irreversible material deformation takes place because of a result of plastic deformation. Second, the sliding of contacting materials causes friction. As a side effect, heat is generated because the material deforms and friction between two materials causes a change in temperature, which can influence the material properties and generate thermal strains. According to these phenomena, residual stresses will be created within the tube wall. The residual stresses are locked in complex patterns because of the circumferential material flow that occurs during the process due to the effect of reduction of the inner and the outer walls of the tube. These stresses may affect the mechanical properties and fatigue behavior of the final product. Hence, there is a great need to measure residual stresses within the tube wall.

For tube drawing processes with a fixed mandrel (plug), most of previous researches have been carried out using analytical and numerical methods, while few studies have been done experimentally because it is prohibitively expensive. Therefore, continued research using experiments and real-life measurements during and after the tube drawing process with a fixed mandrel is necessary to obtain dependable results.

Internal stresses or residual stresses are defined the system of stresses in equilibrium that remains in a solid material without external load. It is difficult to predict residual stresses within a body because of a complex behavior of stress distribution. However, choosing the appropriate process for measuring residual stresses can give a real perception of the effect of these stresses on mechanical properties and fatigue life than fracture.

For residual stress measurements relating to the tube wall, all of the literature indicate that destructive, semi destructive and non destructive techniques have been utilized to estimate the residual stresses. Although non destructive techniques are the most common methods to measure residual stress within the tube wall, they are restricted and limited in measuring the depth of residual stress, and in addition, these techniques require special devices that causes the cost increase. Destructive and semi destructive techniques have also disadvantages in measuring the residual stress with circular

sections; some of them are restricted in depth and the others have difficulty during the cutting process.

1.3 Thesis Objectives and Contributions

Tube drawing with a fixed mandrel (plug) is a complex operation because of the plastic deformation produced in the forming zone due to the reduction of area (R%) and the friction factor between the metal and tools. Designing and manufacturing of dies and mandrels were one of the main goals in this study, since they were used in production of the tube products with R=16% and 23%. The procedure of the tube drawing process can enable linking the parameters of the drawing process with the drawing stress.

In this study, residual stresses within the tube wall of an AISI 1010 steel tube were measured using four methods. First, Removing Layer Method (RLM) when layers of the tube wall were removed from the inner and the outer surfaces using milling process with a CNC machine. Residual strains were then measured according to the Tee Rosette Strain Gages (TRSG) with longitudinal and circumferential directions. Second, Slitting Method (SM) in the form of a slot was longitudinally made in the tube wall using milling process with a CNC machine. Residual strains were consequently recorded in the circumferential direction. Third, X-Ray Diffraction (XRD) was applied to measure residual stress below the inner and the outer surfaces as well as the inside of the tube wall according to the five orientations. Finally, the Finite Element Method (FEM) was performed to determine residual stress within the tube wall by simulating axisymmetric models.

The FEM has been extensively used in order to solve metal forming problems. A tube drawing process with a fixed plug was presented using the FEM with ABAQUS 6.14-2 software to study the effect of semi die angle, semi plug angle, and friction coefficient on drawing stresses to identify optimum geometries of tools. An Axisymmetric Finite Element Model (AFEM) was improved to decrease the time of analysis. The non linear analysis is very important to obtain the levels of plastic strain. A contact element (Master and Slave) is used to simulate a tube model with an Explicit/Dynamics analysis that has the ability to solve complex contact interaction;

this gives more accurate results with respect to other analytical methods. The main objectives are as follow:

- Designed and manufactured dies and fixed mandrels were used in tube production where the outer diameter, the inner diameter, and the wall thickness were reduced.
- Drawing of AISI 1010 steel tubes with different dimensions where the R= 16% and 23% were performed.
- Experimental force vs. displacement plots using the compression process were determined for R=16% and 23%.
- Axial and hoop residual stress measurements were conducted within the tube wall by removing layers from the inner and outer surfaces of the tube using a milling CNC machine.
- Hoop residual stress measurements were conducted inside the tube wall by making a slot in the tube wall using a milling CNC machine.
- Hoop residual stresses below the tube surfaces and within the tube wall using XRD were evaluated in the five different orientations.
- Drawing force vs. displacement plot was numerically estimated by the AFEM for R=16% and 23%.
- Axial and hoop residual stresses inside the tube wall were numerically identified by the AFEM.
- Effects of process parameters (semi die angle, semi plug angle and friction coefficients) on drawing stress were numerically predicted by the AFEM at R=23%.

The contribution of this thesis is the use of a CNC milling machine to remove layers of the tube wall to measure residual stresses. First, a cutting tool mills removed layers from the inner surface of the tube while the TRSG was fixed on the outer surface of

the tube. Second, the TRSG was put on the inner surface of the tube and the cutting tool mills removed layers from the outer surface. In both cases, the TRSG was surrounded by insulating and covering materials to protect it from the effect of coolant fluid and chips during the cutting process.

1.4 Scope of the Thesis

This thesis investigates the AISI 1010 steel tube manufacturing process used in various mechanical applications. Tube products that are manufactured using a fixed mandrel (plug) require specialized laboratories and high control to obtain high productivity with an ideal time consumption. These products because of the forming process have residual stresses. For a better understanding of the tube drawing process with a fixed mandrel (plug) and the state of residual stresses within the products, experimental tests and measurements were performed. At an industrial scale, experimental operations enable measuring different parameters easily; drawing force, velocity, displacement, and dimensions. On the other hand, measurement of residual stress requires special methods depending on the geometries and dimensions of the product as well as the stress location that needs to be measured. The finite element method appears to be an active tool to analyze mechanical engineering problems. The first objective of the finite element modeling is to achieve a large number of tests with short time. The second objective is the ability to obtain more results that cannot be measured experimentally such as strains and stresses during and after drawing.

CHAPTER 2

TUBE DRAWING, RESIDUAL STRESSES AND LITERATURE REVIEW

2.1 Introduction

This chapter deals with the tube drawing process, residual stress measurement, and literature review. A description of the underlying principles of tube drawing and types of tube drawing processes were introduced, and weight is put on a tube drawing process with a fixed mandrel. The parameters of the effects of tools on the tube drawing process with a fixed mandrel were presented. The different physical phenomena that happen during the process were explained in detail. Analytical methods of the tube drawing process and residual stress measurement were shown. The finite element method applied axisymmetrically was presented. Techniques of residual stress measurement with different methods were given. Previous works that have been related to the analysis of tube drawing and residual stress measurement were displayed.

2.2 Tube Drawing Processes

Tube drawing is the process of pulling a workpiece through tooling causing a reduction of the outer and the inner dimensions. The tools of the tube drawing process are the die and mandrel. The die has a nib die to calibrate the outer diameter of the tube while the inner diameter of the tube can be formed with different techniques according to the type and shape of mandrels. The tools of the process are made of a hard material in order to resist the force of friction during the drawing process.

Using the tube drawing process means many advantages compared with other metal forming processes and it is in the forefront of producing high-quality tubing with precise dimensions as well as a good surface finish. It also has the added advantage of strengthening the material through cold working [1]. Since tube drawing is so versatile, it is suitable for both large and small-scale production [2]. Four kinds of tube drawing

processes are generally used; drawing without a mandrel (tube sinking), drawing over a stationary mandrel (a fixed mandrel or a fixed plug) that is used in this thesis, drawing over a floating plug, and drawing over a moving mandrel [3].

2.2.1 Tube Drawing without a Mandrel (Tube Sinking)

There is no internal support to insert inside of the tube as shown in Fig. 2.1**.** The forming occurs on the outer surface of the tube by a nib die whereas the inner surface of the tube is free. This type of drawing is applied to reduce the outside and the inside diameters with constant wall thickness and uses a long bearing to achieve the correct size and optimal smoothness of the outer surface. Smaller internal diameters only are reduced by using this type while the process does not give the best surface finish. As the tube wall thickness increases, the quality of the surface finish decreases. Tube sinking is the most economical, especially for thick-walled tubes and tubes smaller than 12 mm in diameter. Some applications can use multiple sinking operations such as low-cost lawn furniture.

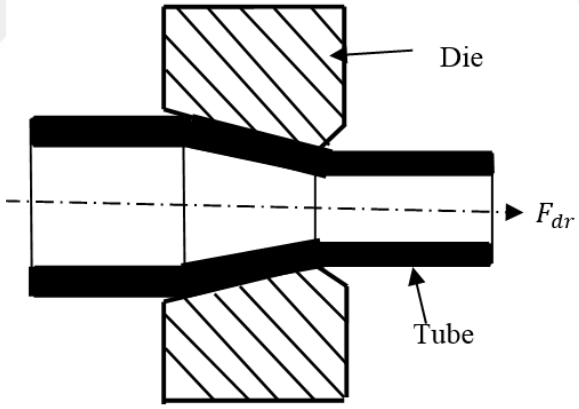


Figure 2.1 Tube drawing without a mandrel (Tube Sinking)

2.2.2 Tube Drawing with a Fixed Mandrel (Fixed Plug)

The forming takes place at the outer and the inner surfaces of the tube as displayed in Fig. 2.2. In this study, this type of drawing was considered. In this type, a ring die (nib die) is utilized to deform the outer surface of the tube and a mandrel (fixed plug) is used to deform the inner surface of the tube. A cylindrical and conical plug can be

employed to reduce the inner dimensions. The reduction of area is limited and this operation is slow but it gives the best inner surface finish in comparison with other types of tube drawing.

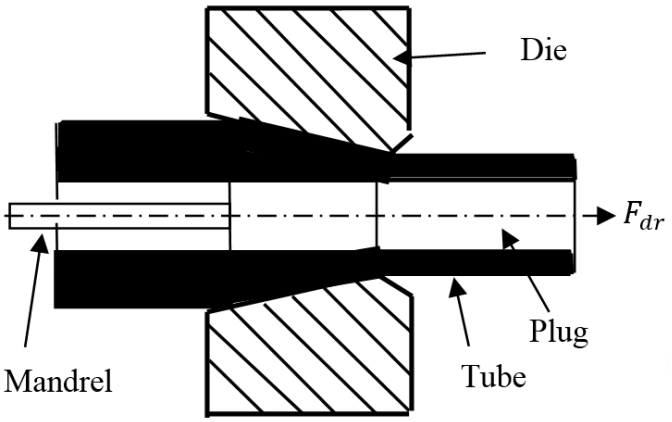


Figure 2.2 Tube drawing with a fixed mandrel (Fixed plug drawing)

2.2.3 Tube Drawing with a Floating Plug

The tools look the same as the setup for tube drawing with a fixed plug as described in Fig. 2.3. It can decrease the reduction of the area until reaching 45% in the die throat of the die if the mandrel floats are selected accurately. The mandrel is set up with a plug and since the plug is conical in shape, it is pushed ahead of the forming event. There is friction between the mandrel and the tube, the plug is floating free and stays located in proximity of the die.

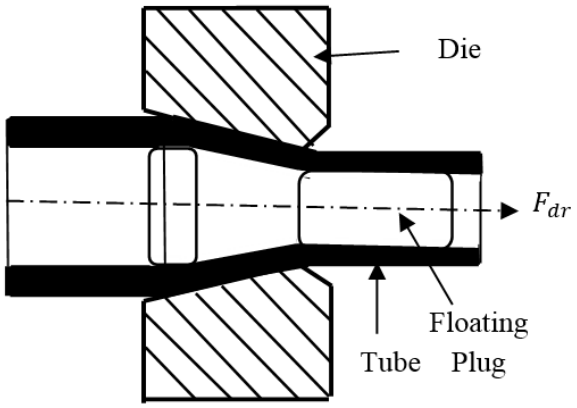


Figure 2.3 Tube drawing with a floating plug

2.2.4 Tube Drawing with a Moving Mandrel

Fig. 2.4 depicts the use of a moving mandrel in the tube drawing process. In this type, there is a long mandrel instead of a plug and this mandrel moves together with the tube in the direction of the drawing. While it can form a good surface, the drawbacks are the maximum length of the tube product allowed by the mandrel length and the drawing bench lengths as well as needing an additional operation to remove the mandrel.

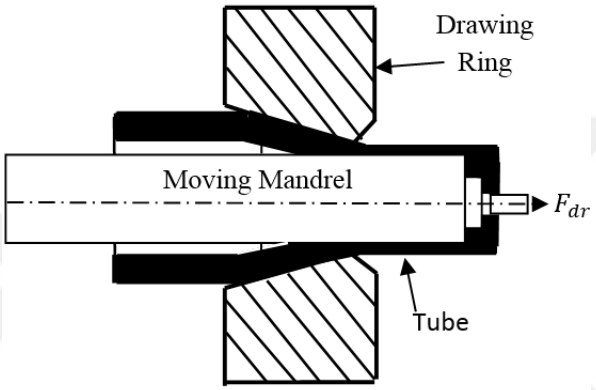


Figure 2.4 Tube drawing with a moving mandrel

Based on the types of tube drawing process that are explained above, the tube drawing process with a fixed mandrel was performed in this Ph.D. thesis experimentally and numerically.

2.3 Tools and Machines of Tube Drawing with a Fixed Mandrel

2.3.1 Tube Drawing Die

A die is a specialized tool and includes two parts: the first is called a nib die and contains the die geometry (back relief, bearing or land, approach angle and bell) as depicted in Fig. 2.5. The nib die must have high fatigue strength and a high wear resistance to retain hardness at a high surface temperature of the die. In this study, cemented carbide material is used for the die material. The second is the die block that surrounds the nib die and is made of a steel casting.

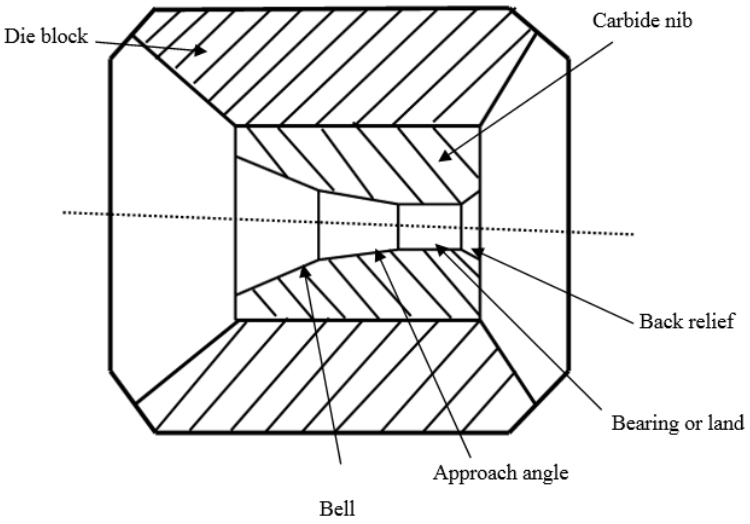


Figure 2.5 Tube drawing die

2.3.2 Fixed Mandrel Tube Drawing

The function of the fixed mandrel or fixed plug is to carry out wall reduction and control the size of the hole for the tube. When the semi plug angle is zero, the tool is called cylindrical mandrel (cylindrical plug). If the semi plug angle is non zero, the tool is said to be a conical mandrel (conical plug). The material of the plug depends on the material type of the tube. In this study, cemented carbide is also utilized to resist the wear and compression forces during the process. A steel nut is used to fix the plug with the steel rod as displayed in Fig. 2.6.

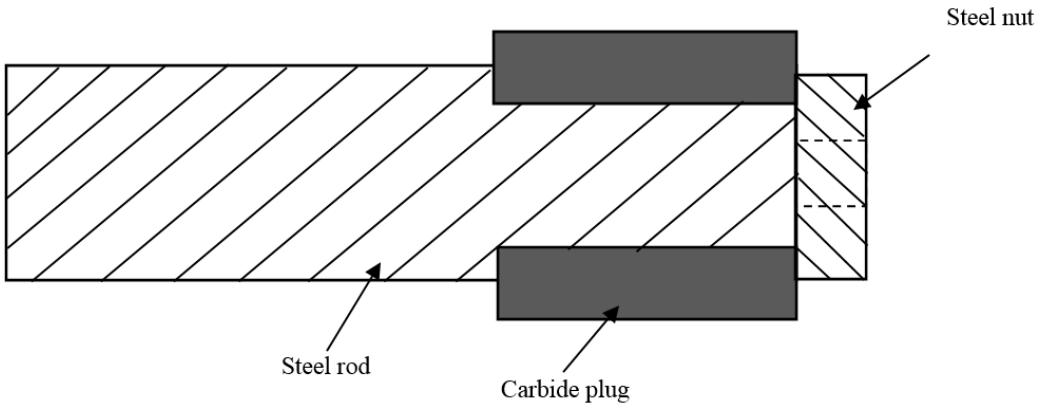


Figure 2.6 Fixed mandrel tube drawing (cylindrical plug)

2.3.3 Bench Machine Tube Drawing

A drawing bench is a machine that apply the drawing force to draw the tube. In tube drawing with a fixed mandrel, the bench is applied to decrease tube wall thickness at cold temperature. A straight chain bench is used to catch a part of the tube and the tube is then pulled [4]. The speed of drawing can be chosen according to the gearbox. Fig. 2.7 displays a sketch for a tube drawing bench.

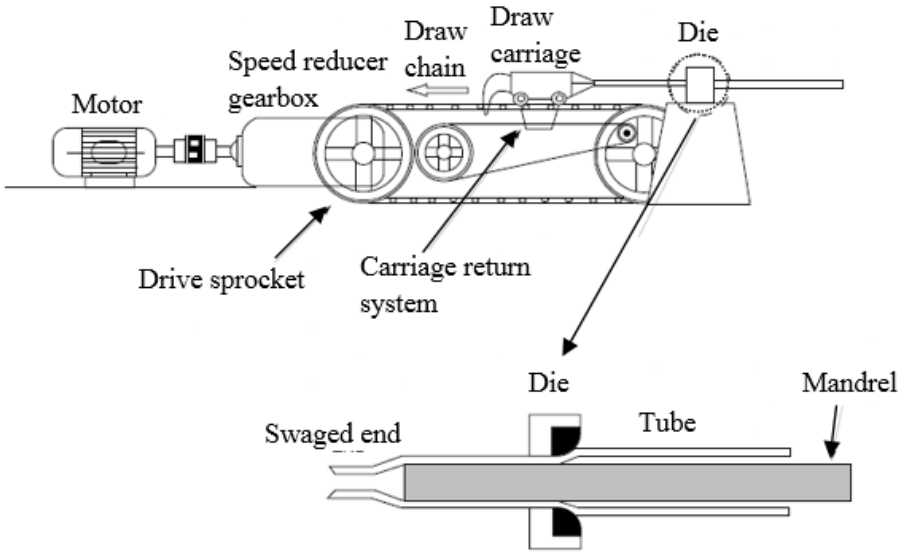


Figure 2.7 Tube drawing by a bench machine [4]

2.4 Parameters Affecting the Tube Drawing Process with a Fixed Mandrel

In tube drawing with a fixed mandrel process, there are several parameters that affect the drawing process through a direct impact on plastic deformation, inducing high stress that is generated in the forming zone. These parameters directly affect drawing and residual stresses [5].

2.4.1 Reduction of Tube Area

Reduction of area represents the ratio of the change in tube section area through the drawing process to the initial tube section area. The material type of the product, the final shape of the product and the number of drawing passes are the primary criteria in

the selection of the reduction of area [6]. The effect reduction of area has on the drawing process can be described through an increase of plastic deformation in the contact area between the metal and the nib die, the metal and the fixed plug. In the tube drawing process, the reduction of area can be found according to the outer diameter and the wall thickness of the final tube to the initial dimensions of the outer diameter and the tube wall thickness.

$$\mathrm{R}\% = 1 - \frac{D_i^2 - (D_i - 2t_i)^2}{D_o^2 - (D_o - 2t_o)^2} \qquad (\mathbf{2.1})$$

D_i and t_i represent outer diameter and tube thickness, respectively after drawing, while D_o and t_o are outer diameter and tube thickness before drawing.

2.4.2 Nib Die Geometry

The nib die geometry contains semi die angle, bearing length, and the entry radius as presented in Fig. 2.8 [7]. A semi die angle is defined as the slant of the die wall to the drawing direction and it strongly affects the force needed for drawing since the minimum drawing force can be obtained by optimum die angle [8]. A semi die angle produces differences in the friction during the operation as well as having the effect of redundant plastic deformation [9]. The redundant deformation results from both the friction and shear deformation. This is called radial strain heterogeneity since the tensile strain and localized shear do not contribute to section reduction.

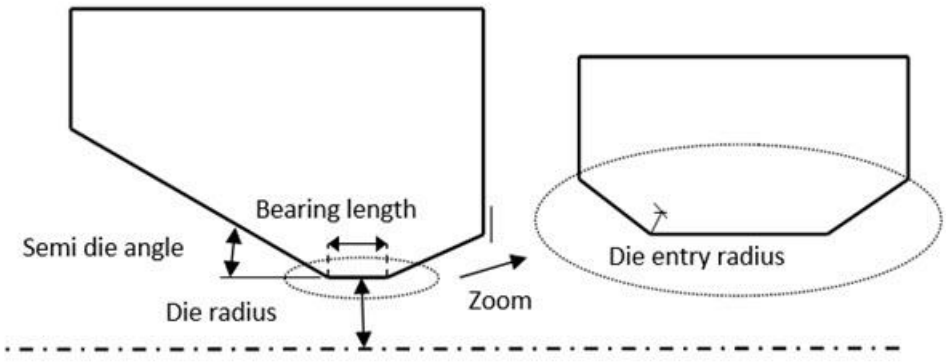


Figure 2.8 Nib die geometry

2.4.3 Mandrel Geometry (Plug Geometry)

Cylindrical and conical plug geometry are used to deform the inner diameter. For the conical, the plug geometry includes semi plug angle and nib. Semi plug angle is the amount of slant of the plug wall in the drawing direction as displayed in Fig. 2.9. It is used to obtain a good surface finish of the inner diameter of the tube. The semi plug angle is between 2°- 4° smaller than the semi die angle, for example, the optimum semi die angle is 12°- 15° in cooperation with a semi plug angle of 10°- 11° for a conical plug [10].

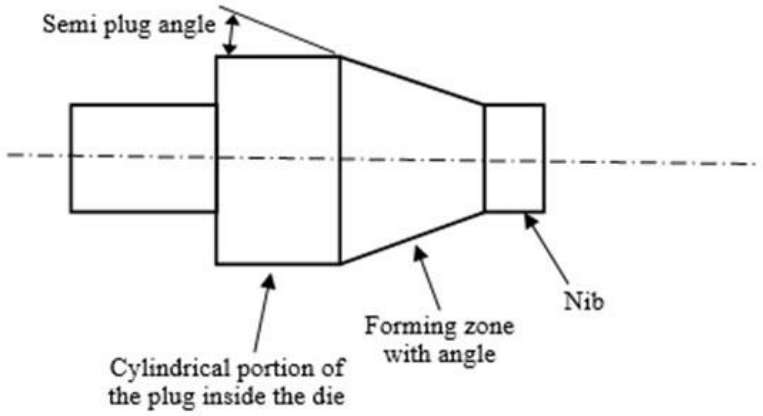


Figure 2.9 Conical plug geometry

2.4.4 Drawing Speed

In a tube drawing process with a fixed mandrel, the drawing speed is slow and it can influence the friction and the material behavior if the material behavior is viscoplastic. In this study, a constant drawing speed was selected.

2.4.5 Lubrication

Lubrication is the most important parameter that affects the tube drawing process. A good lubrication is used to improve the life of the nib die and plug, and the product surface finish. On the other hand, lubrication of tools and metal during the process can reduce drawing force and temperature. The overall goal is to ensure that the nib die and the fixed plug will work to produce as much end product as possible with a

minimum amount of maintenance due to degradation from excessive heat and abrasion. Therefore, it can be thought that lubrication is the very base of reducing friction between the tube and drawing tools, preventing the occurrence of defects and at the same time, it functions to decrease heat as plastic deformation increases [7]. In metal forming operations, fluids are generally categorized into four main types: water-based, oil based, synthetic or semi synthetic and solid (dry) film. In this study, an oil based fluid was considered as a lubricant throughout the tube drawing process.

2.5 Phenomena that Occur During Tube Drawing Process with a Fixed Mandrel

In metal forming processes, three different phenomena occur due to the rush of material through the forming zone and the tube drawing process with a fixed mandrel is subject to these phenomena during the process. First, the plasticity that takes place as plastic deformation due to the movement of material in the drawing direction. Second, the sliding between the material and tools causes the friction. Finally, as the plastic deformation takes place, friction causes heat. The generated heat is then transferred to the nib die, the fixed plug, the tube, and to the surrounding environment. Study of these phenomena is essential to show the strains, the stresses and to provide a systematic control method to obtain high quality products with high efficiency.

2.5.1 Plasticity

A tube drawing process with a fixed mandrel is subject to the theory of plasticity due to the movement of material through the forming region between the nib die and a fixed plug that produce plastic deformations by slipping mechanism at slip planes. The slip plane is defined as the sliding of adjacent blocks of the crystals along definite crystallographic planes. The material starts to convert from an elastic state to a plastic state because of the effect of the drawing force. The plastic deformations occur because of the material motion toward the forming zone and these plastic deformations represent a linear defect in the organization of crystals. A preferred orientation is produced since the crystallographic directions gradually rotate toward more stable orientations that represent the drawing direction and this leads to the transformation of

an isotropic material into an anisotropic material which has new mechanical properties in the new direction [11]. Three constitutive equations describe the phenomenon of plasticity. First, yield condition that represents isotropic and anisotropic yield functions. Second, a flow rule or stress-strain components in relation to time is called plastic strain rate. Third, a hardening law considered as expansion and translation, or both.

2.5.1.1 Isotropic and Anisotropic Yield Functions

In isotropic yield functions, the crystals appear to have the same mechanical properties with different loading directions and oriented in random directions, while if the material in the testing direction exhibits grains, it is said to be anisotropic. Isotropic yield function is the most common than anisotropic equation because anisotropy is too complex for development with cold working as a result of the strain hardening, so that isotropic yield function is used in the mathematical theory of plasticity throughout the deformation regardless of the degree of complexity for the cold working [11]. The Tresca and von Mises have defined the isotropic yield function.

$$\text{Tresca: } f_y = max\ \{|\sigma_1 - \sigma_2|\ , |\sigma_2 - \sigma_3|, |\sigma_3 - \sigma_1|\} - \sigma_y = 0 \qquad (\mathbf{2.2})$$

$$\text{Von mises: } f_y = \frac{1}{2}\sqrt{(\sigma_1 - \sigma_2)^2 + (\sigma_2 - \sigma_3)^2 + (\sigma_3 - \sigma_1)^2} - \sigma_y = 0 \qquad (\mathbf{2.3})$$

$(\sigma_1, \sigma_2, \sigma_3)$ are principal stresses and σ_y is the yield stress in uniaxial tension.

2.5.1.2 Flow Rule

In plastic strain rate, there are two equations that can be expressed to show the flow rule. The first equation is called non associative and represents the flow rule due to the difference of dissipative potential from the yield function. The second is the associative equation when the flow rule and dissipative plastic potential equal yield function.

$$\text{Non associative flow rule: } \epsilon_{ij}^{P} = d\lambda \frac{\partial g}{\partial \sigma_{ij}} \qquad (\mathbf{2.4})$$

Associative flow rule: $$\epsilon_{ij}^{P} = d\lambda \frac{\partial f}{\partial \sigma_{ij}} \quad (\mathbf{2.5})$$

where ϵ_{ij}^{P} represents the plastic strain rate component while $d\lambda$ is a scalar coefficient and σ_{ij} indicates the principal stresses with i and j equal (1,2,3) finally, g represents the dissipative potentials at different yield functions, and *f* is the dissipative potential at the same yield function respectively.

2.5.1.3 Hardening Constitutive Equations

Hollomon's and Ludwik's equations mathematically are applied to describe the phenomenon of work hardening. Hollomon's equation is an effective law to show the relationship between stress and plastic strain.

$$\sigma = K\epsilon_p^n \quad (\mathbf{2.6})$$

σ is the stress, K is strength coefficient, ϵ_p is the plastic strain and n is the stain hardening. The Ludwik's considers the same law with Hollomon's equation and just adding the yield stress.

$$\sigma = \sigma_y + K\epsilon_p^n \quad (\mathbf{2.7})$$

In other cases, the material is subject to the effect of prior deformation during low temperature, so that there is a factor or term that is added which depends on the magnitude of prior deformation ϵ_o.

$$\sigma = \sigma_y + K(\epsilon_o + \epsilon_p) \quad (\mathbf{2.8})$$

2.5.2 Friction

Friction is one of the important phenomena that occur during the tube drawing process due to the sliding between metal and tools. In tube drawing with a fixed mandrel process, there are two areas of friction due to the metal sliding on the walls of the nib die and the plug. Several factors affect friction such as sliding speed, the contact normal pressure, and properties of the contacting material with material roughness [7]. The reaction forces are generated vertically on the internal surface of the nib die and

external surface of the plug because of the sliding between metal and tools. These reaction forces are trying to hinder the movement of material in the drawing direction and this causes a high temperature in the forming zone and thus leads to an increase in plastic deformation. Friction includes the friction coefficient with normal and tangential forces. Determination of the friction coefficient experimentally is complex in the cold working process. Normal force F_n is usually applied and tangential force F_t is measured when the metal starts to be plastically deformed by the indenter. The friction coefficient can be calculated according to a function of the spring-back as shown in Eq. 2.9 [12].

$$\mu = \left(\delta - p + q\frac{F_t}{F_n}\right) \div \left(q - (\delta - p)\frac{F_t}{F_n}\right) \qquad (\mathbf{2.9})$$

μ is friction coefficient, δ is the radial of spring-back, p represents penetration depth and q the contact length.

The Coulomb and Tresca friction laws are widely used to analyze a bulk metal forming process [13], [14]. Fig. 2.10 describes the friction contact for tube drawing with a fixed mandrel process. It shows two contact regions, first between the metal and the nib die, and second between the metal and the mandrel (fixed plug). The metal is sliding during velocity $\vec{v}_s$. For each contact region, two stress components occur due to the sliding and act at the interface. $(\sigma_n)_p$ and $(\sigma_t)_p$ are normal contact and shear contact stresses respectively as a result of the sliding between the metal and plug as presented in Fig. 2.10 semi plug angle is zero (cylindrical plug). The semi die angle α is not to equal zero. $(\sigma_n)_d$ and $(\sigma_t)_d$ represent normal contact and shear contact stresses respectively as the sliding between the metal and nib die. The Coulomb friction and Tresca friction models are expressed by Eq. 2.10 and 2.11.

$$(\sigma_t)_p \le \mu(\sigma_n)_p \, , (\sigma_t)_d \le \mu(\sigma_n)_d \qquad (\mathbf{2.10})$$

For the condition sliding $(\sigma_t)_p = \mu(\sigma_n)_p \, , (\sigma_t)_d = \mu(\sigma_n)_d$ and μ is the friction coefficient.

$$(\sigma_t)_p \le \mu\frac{\sigma_y}{\sqrt{3}} \, , (\sigma_t)_d \le \mu\frac{\sigma_y}{\sqrt{3}} \qquad (\mathbf{2.11})$$

The sliding occurs when $(\sigma_t)_p = \mu\frac{\sigma_y}{\sqrt{3}}$, $(\sigma_t)_d = \mu\frac{\sigma_y}{\sqrt{3}}$ and m represents the Tresca friction coefficient.

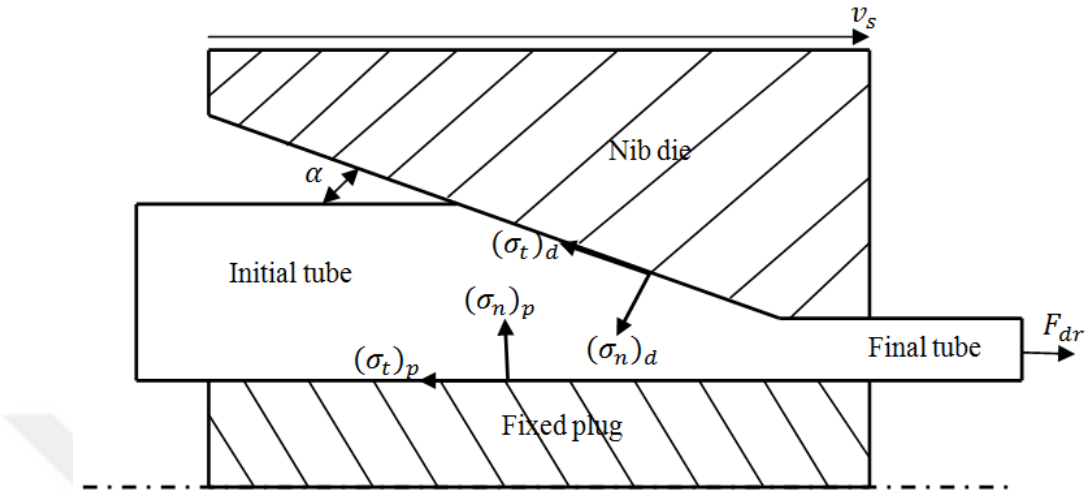


Figure 2.10 Description of frictional contact for tube drawing with a fixed cylindrical mandrel

2.5.3 Heat Generation

Heat generation in tube drawing with a fixed mandrel is produced during plastic deformation imposed by tools and the friction between metal and tools. The effect of plastic deformation on the metal forming process can be extended and depends on mechanical properties of the material and the level of developed stress. In a metal forming process, the fraction of energy is estimated by the Taylor-Quinney coefficient β that is equal to the ratio of the thermoplastic heating [15].

$$\dot{Q_p} = \beta \dot{W_p} \qquad (\mathbf{2.12})$$

$\dot{Q_p}$ is the thermoplastic heat and $\dot{W_p}$ plastic work rate. $\dot{W_p} = trace(\sigma\dot{\epsilon_p})$, where σ is components of stress and $\dot{\epsilon_p}$ plastic strain rate.

Frictional heating is frictional contact that transforms into heat. The increase of frictional heating leads directly to the influence on the behavior of metal and failure of sliding components. Frictional heating results in most metal forming processes such as tube drawing with a fixed mandrel. Heat generation by friction has been studied in some metal forming processes, for example hot extrusion processes. The power of

friction P_f can be calculated by Eq. 2.13 according to shear stress τ and the sliding speed $\|\overrightarrow{v_s}\|$

$$P_f = \tau\|\overrightarrow{v_s}\| \quad (\mathbf{2.13})$$

2.6 Analysis of Tube Drawing Process with a Fixed Mandrel

In recent years, concerns to formalize the tube drawing process have increased because of the growing need for optimizing the production time using different methods. Analytical and numerical methods are commonly used to determine the optimal parameters of the nib die and the plug. Those include reduction of area, semi die angle, semi plug angle, and friction factor, while tests can be conducted on the small scale or directly achieved by using an industrial drawing bench.

2.6.1 Analytical Methods

The Homogeneous Deformation Method (HDM), the Slab Drawing Method (SDM), and the Upper Bound Theory (UBT) are analytical methods that are used in calculations of the drawing stress to determine the drawing force and final tube section. However, these methods are limited to the approximate expression of drawing stress [7].

The HDM is very simplified and just depends on the geometrical shape through the imposition of the plastic deformation caused by external force. Two elements have flat surfaces and these elements represent the initial elements before deformation and the final elements after deformation regardless of intermediate deformation. Therefore, this method is restricted since it neglects the effect of friction and the redundant shear deformation as well as merely depending on yield stress of the material instead of a flow stress model.

$$\sigma_d = \frac{F_{dr}}{A_f} = \sigma_o ln\frac{A_i}{A_f} \quad (\mathbf{2.14})$$

σ_d is drawing stress, F_{dr} represents drawing force, σ_o is the material yield stress and both of A_i and A_f are the initial and final tube section, respectively.

The SDM has been widely applied through plane strain and axisymmetric problems for the metal forming processes such as extrusion and drawing. The main principle of this method is the hypothesis of workpiece deformation on a series of slabs. The deformation path does not change according to the slab shape as well as the stress distribution within the slab not being affected by friction that is generated via shear stress when the force is in a state of equilibrium [16]. As the function of tube wall coordinates, components of normal stress can be varied in the drawing direction according to the yield criterion and the flow rule for a rigid- perfectly-plastic material. In tube drawing with a fixed mandrel, both friction and homogenous deformation are the bases of stress equilibrium in a slab element and by integration of stress components that are obtained via expressions along the tube surface. The drawing stress can be determined by expression Eq. 2.15.

$$\sigma_d = \sigma_y \frac{1+B}{B}\left[1-\left(\frac{t_i}{t_o}\right)^B\right] \quad with\ B = \frac{\mu_1+\mu_2}{tan\,\alpha - tan\,\alpha p} \qquad (\mathbf{2.15})$$

t_o and t_i thickness of tube before and after drawing respectively, μ_1 and μ_2 friction coefficients between metal with the nib die and with the plug respectively, α is semi die angle and αp semi plug angle.

The UBT is one of the common methods to analyze the stresses and strains by calculating the energy that is required for forming and the energy consumed due to the friction between the metal surfaces and tools surfaces. The UBT method gives good results in comparison with other analytical methods, and it can be used to analyze the three-dimensional model. Three aspects are taken into consideration using this method: homogenous deformations, friction, and redundant deformation [17].

2.6.2 Finite Element Method (FEM)

2.6.2.1 Introduction to FEM

Numerical methods, particularly finite element analysis represents a qualitative leap in metal forming operations. FEM is used to solve the problems of engineering and mathematical physics as well as being a more powerful tool for analysis of complicated geometries, loadings, material properties, and contact problems in comparison to

analytical methods [18]. FEM has been used to study many aspects that cannot be applied using analytical methods such as mechanical, thermal, and contacts in a short time. The solution to any problem can be represented by a mathematical function through the subdivision of a region into smaller regions or elements. These elements connect together by nodes and by assuming approximation of a displacement function; actual displacement for each element can thereby be determined [19]. The equations of equilibrium according to the principle of virtual work are obtained from the shape function. The displacements are the basis of solving the models by adding boundary conditions, the stresses and strains for these displacements are calculated. FEM has the ability of obtaining geometry optimization by simulation of many models that include a large number of parameters [20].

2.6.2.2 Axisymmetric Finite Element Model (AFEM)

The AFEM uses the analysis of the circular structures under axisymmetric loading. A three-dimensional problem for circular sections can be solved using a two-dimensional representation while applying an axisymmetric element [21]. Tube drawing with a fixed mandrel is one of the mechanical applications that can be analyzed using the AFEM since a generation cross section can be rotated $360°$ about an axis and it can be called rotationally symmetric.

The strain-displacement relationship according to the axisymmetric element includes a fourth component of strain ε_θ, ε_{rr},ε_{zz} and γ_{zr}. These components are related to the displacement u and v. The component of stress also contains σ_θ, σ_{rr},σ_{zz} and τ_{zr}. Fig. 2.11 shows strains and corresponding stresses in an axisymmetric solid while Fig. 2.12 presents tangential strain.

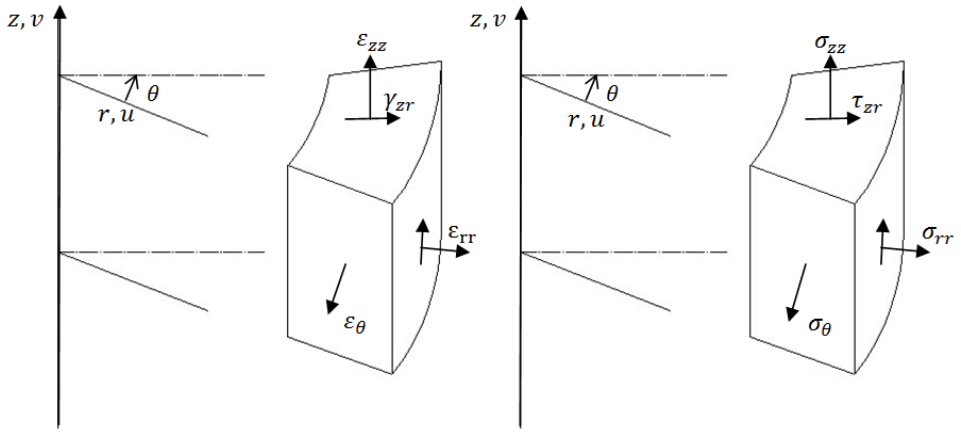


Figure 2.11 Strains and corresponding stresses in an axisymmetric solid

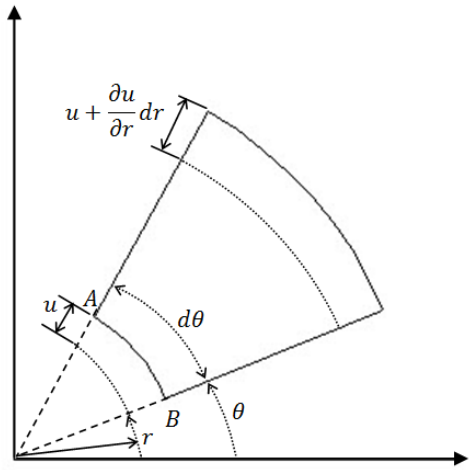


Figure 2.12 Tangential strain in an axisymmetric model

2.7 Residual Stresses

Manufacturing processes generate residual stresses within a body after production or processing in the absence of external forces or thermal gradient [22]. Tube products that are formed using a fixed mandrel include residual stresses due to the non homogeneous plastic deformations in the workpiece through the drawing process. These residual stresses cannot be observed during the process but there is a great need to determine residual stress distribution inside the tube wall. A high-quality product can be obtained when the optimum geometries of the nib die and the fixed plug are

chosen. Destructive, semi-destructive and non destructive techniques can be applied experimentally to estimate residual stresses.

2.7.1 Destructive Technique

The destructive technique is applied to determine residual stresses when the specimen is cut or destroyed and this method is commonly used in a wide range of engineering components [23]. Many different destructive techniques have been found to evaluate residual stress: the Contour Method (CM), the Slitting Method (SM), the Block Removal/Splitting/Layering Method (BRSLM), and Sach's Boring Method (SBM). These methods completely rely on a strain release principle during the measurement of the deformed shape of the specimen while cutting to relax the residual stresses. The relationship between the magnitude of the deformation and magnitude of the released stress is an exploitable linear [24]. In the CM, residual stress is determined by carefully cutting a specimen into two parts using a wire Electric Discharge Machine (EDM) to measure the resulting deformation and the data of displacement is then recorded [25]. The SM is applied to evaluate residual stress along one direction and there are three steps to apply this method: application of a strain gage, incremental slitting, and monitoring near-slit strain change and data recording [26]. On the other hand, the BRSLM is applied to measure strain components during removal of a layer of a specimen and then residual stresses are calculated [27]. SBM specializes in determining axisymmetric residual stress in cylindrical components in the axial and circumferential directions [28-29].

2.7.2 Semi Destructive Technique

Sometimes this technique is called hole drilling strain gage. This method is very similar to the destructive technique but the drill removes a small amount of the material. This method is considered simple and quick compared with other methods. There are three methods that can be applied: Deep Hole Drilling (DHD), Center Hole Drilling (CHD) and Ring Core (RC). In DHD, the residual stress fields are measured in very thick components by using a small diameter hole that is drilled [30-31]. This method is commonly applied to isotropic materials. The CHD is used to measure the surface strain by incremental machining of the shallow hole in a component [32]. By

attaching the Strain Gage Rosette (SGR) concentrically around the drilled hole, the surface strains can be measured and a SGR is generally used. The residual stresses are calculated according to the measuring of relaxed deformation and the maximum depth of drilling during various steps [33]. The RC is applied to estimate the uniform and non uniform residual stresses within a wall and it is similar to the hole drilling method but a notch is milled around the SGR instead of drilling a hole through the middle of the SGR [34].

2.7.3 Non Destructive Technique

The main idea of the non destructive technique is summed up in determining the relationship between the residual stresses and their effects on crystallographic properties of the measured of material. Many different methods are used to determine macroscopic stresses in the material. These methods are: Neutron Diffraction (ND), Synchrotron Diffraction (SD), X-Ray Diffraction (XRD), Ultrasonic, and Magnetic. The ND is used for the bulk measurement within thick specimens [35], while the SD is applied to shallow depths of specimens [36]. Neither the ND nor the SD can be in-situ investigations and they are only available in some 30 facilities worldwide while XRD is suitable for surface measurement [37]. In this study, the XRD was used for the measurements. The XRD depends on the measure of strain in the crystal lattice and on elastic constants, assuming a linear elastic distortion of the specific crystal lattice plane as the associated residual stress is evaluated [38]. There are many grains and crystals that will contribute to the measurement due to the X-Rays over an area being impinged. The measure of surface stress and through volume stress can be determined using the ultrasonic method by detecting variations of ultrasonic wave speed and correlating them with crystallographic [39]. The Magnet Method or Magnetic Barkhausen Noise (MBN) is limited to ferromagnetic materials since it is magnetic in nature and its magnetic properties vary sensitively according to stress due to the phenomenon of magnetostriction [40].

2.8 Literature Review

Increasing demand for high quality tube products led to the emergence of many studies that deal with tube manufacturing processes during designing and manufacturing of the tools as well as analysis of the tube drawing process. The previous research on analysis of tube drawing has been recorded for many years. In the past, UBT was widely applied for analyzing mechanical applications by means of the velocity field but it is limited, and require a long time. For the reason, in this study, they were not taken into consideration. The rapid development in computer technology led to the emergence of many programs that were directly connected with the FEM such as ANSYS, ABAQUS, MARC, NASTRAN, and MSC SUPERFORM that helped researchers use this method. Few researchers have studied tube-drawing processes experimentally since it is expensive. Despite the presence of these studies, tube drawing with residual stresses has been linked in the last few years to an increase in the quality and mechanical properties of products. These studies are based on numerical methods, destructive, semi-destructive and non destructive methods. In our study, both experimental and the FEM were investigated for analyzing the tube drawing process with a fixed mandrel and determine residual stress inside the tube wall.

2.8.1 Literature Review of Tube Drawing Process

The process of tube drawing started in 1935 since then have investigated by several authors using analytical methods. Because of the development in the use of modern techniques in the last few years, we decided to start going back to 2005. In 2005, Neves et al. [41] used the analytical, numerical and experimental method to analyze tube drawing with a fixed plug for A304 stainless steel tubes. The model was simulated using the FEM with MSC Superform software as displayed in Fig .2.13 to determine the best geometry of the die and the plug that lead to reducing the drawing force. In addition, the UBT was studied to determine drawing stress. In this study, a tool device was designed specially to reduce the drawing force by using two dies to draw the metal under lubrication. The study showed that the tube drawing with a fixed plug by this

tool device can be done and this tool was aided by application of pressurized lubrication.

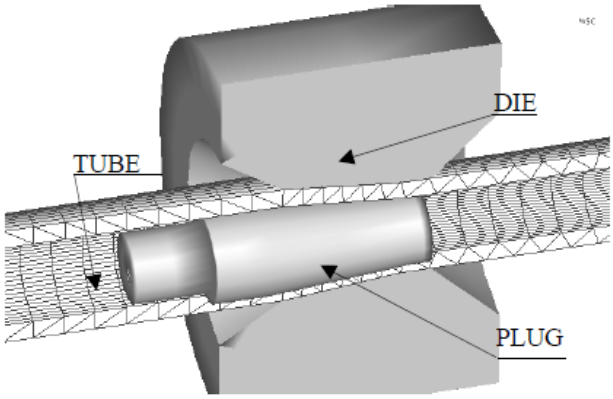


Figure 2.13 Meshes of the tube made by Superform software [41]

In tubular material, forming energy and deformation behavior depend on the shape of the die and the mandrel. Kim et al. [42] designed a stepped and a straight mandrel (cylindrical mandrel) as shown in Fig. 2.14 to produce the automotive Steering Input Shaft (SIS) without any defects. This study concluded that the stepped mandrel type gives good results for the distribution of stress concentration without any failure of transmission of drawing force compared with the straight type mandrel.

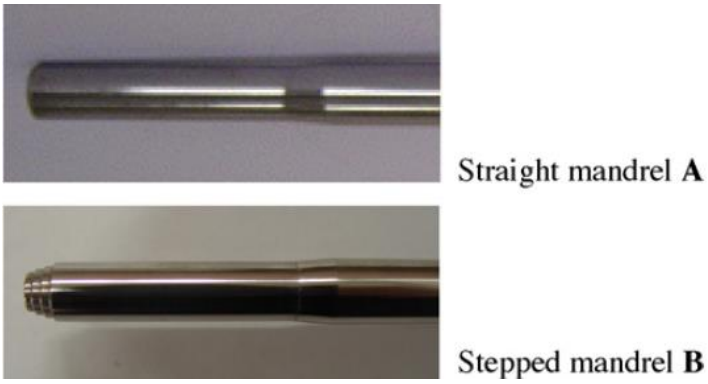


Figure 2.14 Straight and stepped mandrel geometry [42]

Lee et al. [43] evaluated a Critical Damage Value (CDV) in the tube drawing process during a simple compression test to select an appropriate die shape that prevents material fracture. The study analyzed the AISI1045 SIS by using the FEM and

experimental method under lubricated conditions with MoS_2 for friction 0.1. In this work, the most appropriate die was selected through the straight shape die with semi die angle of 10.0° while finite element results gave less than 0.700 CDV as a maximum damage value of the tube material.



Figure 2.15 Tubes production according to the redesigned drawing [43]

The backward flow forming process (tube drawing) was analyzed by Moreira et al. [44] using the finite element method with ABAQUS code to simulate two dimensional plane strain and three dimensional models according to the implicit and the explicit integration techniques. Flow forming in the as-received state after quenching and tempering heat treatment was used while conical rollers produced a tube blank. The internal diameter and wall thickness of a tube 320 mm and 9.53 mm respectively were used to apply the uniaxial tensile experimental tests for an AISI 41B30H. The results showed that the as-received condition resulted in a slightly lower drawing force in comparison to the quenching and tempering.

Danckert and Endelt [45] modelled tube drawing with a floating plug by applying the FEM by LS-DYNA to simulate two dimensions with rotational symmetry using the implicit time integration. The study concluded that both the length and the shape of the bearing channel depend on the drawing force with conventional tooling while Beland et al. [46] applied the FEM to determine the optimization of tool geometry by using LS_DYNA to reduce maximum stress level for AL 6063 T4 tubes. This study was performed using a hydraulic industrial bench and used three tools for the fixed plug drawing process, which are a sinker, die, a drawing die, and cylindrical plug as

shown in Fig. 2.16. The study showed that it can draw three tubes at the same time with the maximum length of 12 m which was tested on different tube diameters and wall thicknesses.

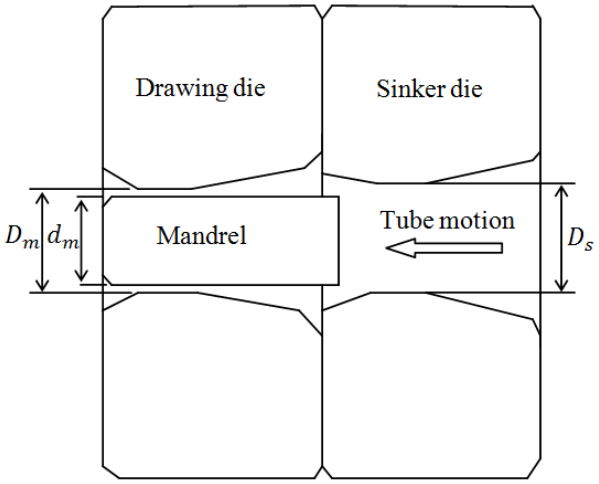


Figure 2.16 The sinker and the die drawing with a fixed mandrel

Tube production by mixing both the sinking and the fixed mandrel tube drawing methods together was presented by Bihamta et al. [47] to study the effect of initial tube geometry according to the FEM and showed acceptable agreement compared with experiments results. The study revealed that initial wall thickness and initial outer diameter in most cases are dependent on the maximum and the minimum of final the tube wall thicknesses. Results showed that the effect of drawing force is larger than the effect of the initial thickness.

Bui et al. [48] estimated the formability limit by both theoretical and experimental methods of a single pass for aluminum tubes that are used for transportation purposes. For the analytical method, the UBT was investigated and a new experimental methodology was applied using the conical mandrel and a special control system to determine mandrel displacement during the process while the tube pulling axis was controlled at a constant speed. The drawing process was achieved by a small hydraulic tube drawing machine. For lubrication, Magnus CAL 70-2 oil was injected inside of the tube and utilized in multi-jets around the tube in front of the die for outside lubrication as pointed out in Fig. 2.17. The study concluded that tube products can be

obtained using a moving conical mandrel and when the tube reaches its formability limit, the minimum wall thickness will be determined.

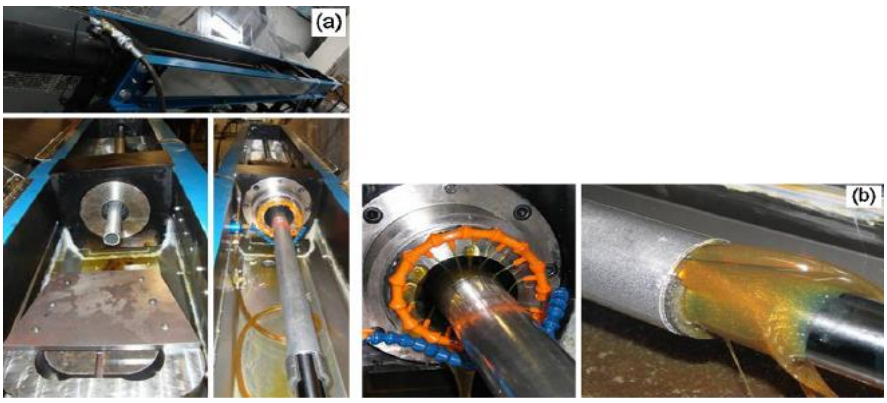


Figure 2.17 (a) Machine that draws the tube, and (b) lubrication procedure [48]

Bihamta et al. [49] studied the parameters of tools during tube drawing and they showed the effect of die angle, mandrel angle, and die fillet radius on the maximum possible tube deformation by using a newly developed procedure. In this study, FEM with an in-house code was used to simulate AL 6063-0 tube for the variables of the mesh on the tube wall automatically. The prototype tube drawing was performed using the D-optimal method, which was selected as an experimental design. The study showed that the FEM for optimization of metal forming processes can be used to choose optimum geometry.

Palengat et al. [50] improved the quality of the finished tubes during the study of cold tube drawing with and without a plug (mandrel drawing and hollow sinking respectively) as presented in Fig. 2.18. The FEM was developed according to different test results. The physical parameters were determined experimentally through a proposed thermo-mechanical study of the drawing process to identify the constitutive equation, the inelastic heat friction and the convection of heat transfer. The study revealed that the temperature variation and interface properties have a large influence on the local behavior of the material.

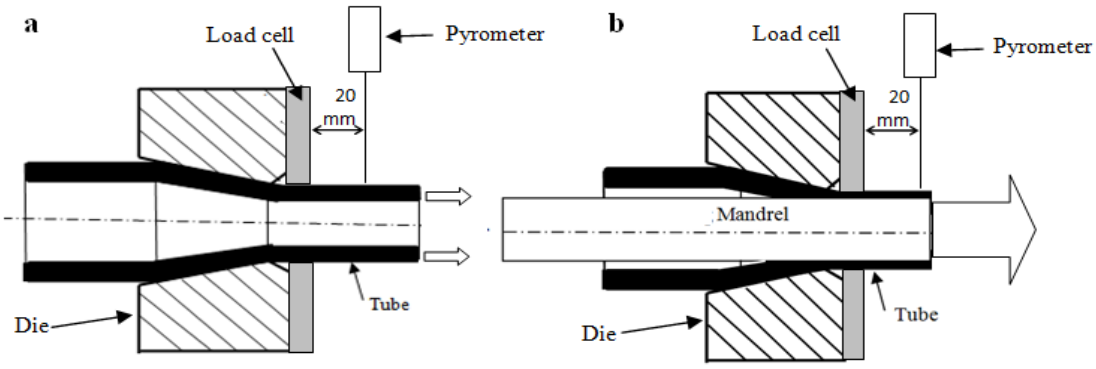


Figure 2.18 (a) Hollow sinking process, and (b) mandrel drawing process

Biomedical tools are considered some of the important components that can be produced by metal forming operations. Linordon et al. [51] displayed both numerical and experimental method to design a conical mandrel with small cone angle to draw tubes, which is used especially for steel in biomedical tools as depicted in Fig. 2.19. The local stress and strain data were determined using the FEM and it is a tool for process optimization. Experimental conditions for the drawing test were developed to evaluate ductile failure criteria by Scanning Electron microscopy (SEM) fractography, which enable understanding of the fracture locus and the propagation direction of the fracture. Eleven failure criteria, which were selected to study the deformability of cobalt-chromium alloy tubes were developed. Several mandrels with different diameters were examined to identify the tube drawing limit in a series of drawing tests.

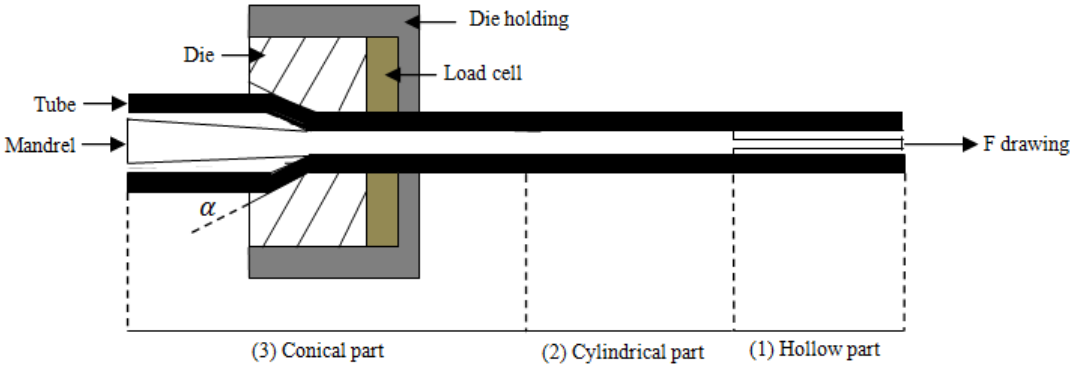


Figure 2.19 Tube drawing process by a conical mandrel

Sheu et al. [52] designed an optimum drawing die profile with two types of die orifices using an arc-type and Bezier curve type profile as displayed in Fig. 2.20. The FEM was also used to run 18 trails to determine strain deviation and maximum drawing force. The study concluded that two types of tube drawing die design methods are able to give best results of load drawn and the effective strain deviation along the radial direction on the tube exit section.

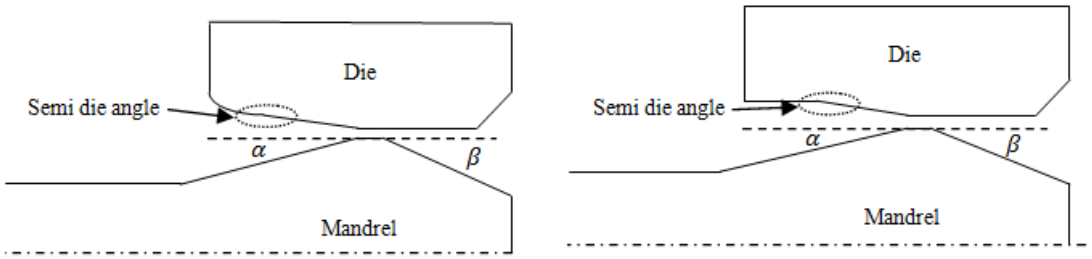


Figure 2.20 Arc-type and Bezier curve-type drawing dies

Trana et al. [53] correlated a numerical with an experimental approach to determine the drawing efficiency of 6082 0-temper aluminum alloy for cartridge tube manufacturing. The plane stress and plane strain specimens were performed with tensile, compression, and shear tests for various samples. The plastic strain and graph of the material envelope were used to find zero Lode parameters. A FEM with a 3D LS-DYNA model was examined using a solid element type, which gives plastic strain correlation. The cartridge tube was carefully examined for fracture, dimension, and shape at the end of the drawing operation. The study proved that the safe drawing force can be determined by experimental test when processing a thin cartridge tube subjected to inner pressure.

2.8.2 Literature Review of Residual Stress inside Tube Wall

In the last few years, there was a significant increase the number of studies, which specialize in determining the residual stress within the tube wall thickness of the manufactured products. The simple technique to measure residual stress in a wound composite tube was founded by Casari et al. [54] using the cutting method and classical equations of solid mechanics. All layers of the tube are removed on which strain gages are bonded. Strain follows a non monotonic evolution that depends on the order of

cutting operations when a series of cuts is performed. This simple technique gave good results with a short time to show effects of manufacturing and moisture on the internal multi-axial stress level.

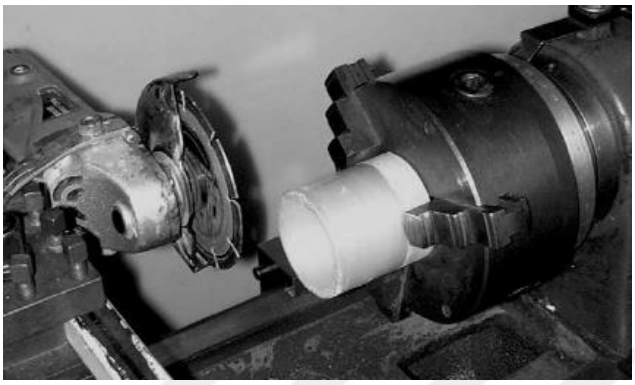


Figure 2.21 A lath machine to measure residual stress by saw mounted [54]

Balalov et al. [55] evaluated residual stresses in cylindrical shells and tubes with external diameters less than 60 mm implementing both the hole drilling method and reflection hologram interferometry during the development of the technique for deriving residual stress component values within 5% accuracy in an absence of stress gradients over the probe hole diameter. The study showed that in thin walled cylindrical shell a determination of actual stresses can be obtained while in a thick-walled cylindrical tube, residual stress distribution at the proximity of welded joint can be determined.

Kuboki et al. [56] developed numerical analysis and experimental method to study the effect of a plug on residual stress in tube drawing process. Residual stresses with and without a plug were examined by using AFEM with commercial code ELFEN in the changing of tube wall thickness. The SM was involved in evaluating residual stress experimentally by dividing the tubes into eight pieces at an even 45° and the displacements of the tube were measured. Residual stress by respective bending of the tube wall at the approach and bearing according to the analytical results was estimated.

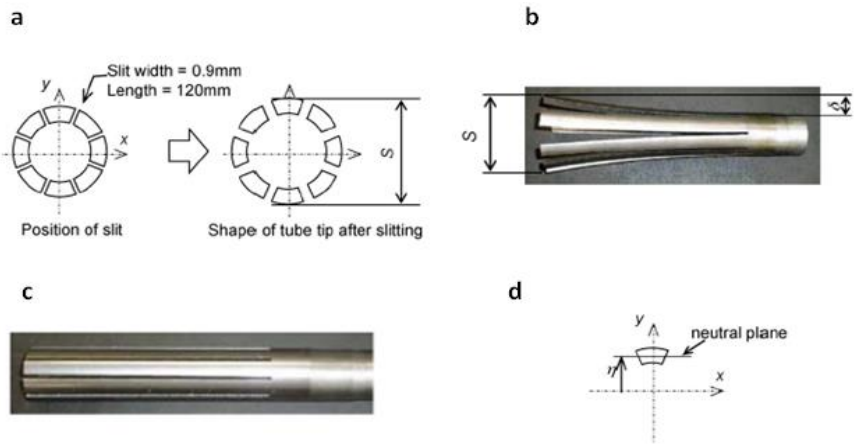


Figure 2.22 Deformed tube by residual stress after slitting (a) Schematic illustration of slits, (b) without a plug sample, (c) with a plug sample, and (d) curvature calculation [56]

A shell finite element according to the total Lagrangian formulation framework and a specific experimental process were improved by Grognec et al. [57] to show the effect of residual stresses and geometric imperfections on the elastoplastic buckling and post-buckling of thin cylindrical tubes under external pressure and axial compression. Axial and circumferential residual stresses were experimentally determined when the strain gages were bonded to the inner wall of the tube then; the strains were progressively released by chip removal on the outer wall surface using a turning machine. The results showed good agreement and the study concluded that plasticity and all imperfection types related to the initial state of stresses have a rather limited influence.

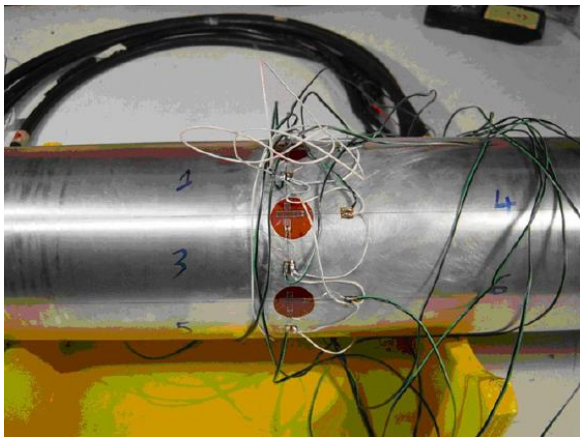


Figure 2.23 Strain gages bonding fixed on the outer surface of the tube [57]

Delgadillo et al. [58] investigated using a hole drilling rosette to determine residual distribution along five cross sections for one short segment of a VOE-SAW thin walled pipe. Combined state of stress was evaluated by using a special device. Soil movement was the base to determine the live load acting on the pipe section and measurement of strains as well as the calculation of associated loads during the blind-hole residual stress measurement. The study showed that the conventional strain gage or residual stress technique can be applied to estimate the exit loads. The distributions of residual stresses were in complex shape and these distributions were similar for cross section that were very close to each other.

The numerical method by three dimensional FEM and a non destructive technique by neutron strain imaging measurement were investigated to calculate residual stresses for the SF-copper tube in the center of the wall Pirling et al. [59]. The ND method in the three orientations was performed by assuming the principal axes to correspond to the sample symmetry, axial, radial, and hoop directions. The study revealed that the effect of stress evolution is not important for neither the thinnest nor thickest wall parts of the tube except a small shifting in the position of zero stress while the behavior at the outer side of the tube is effected where the plateau is flat.

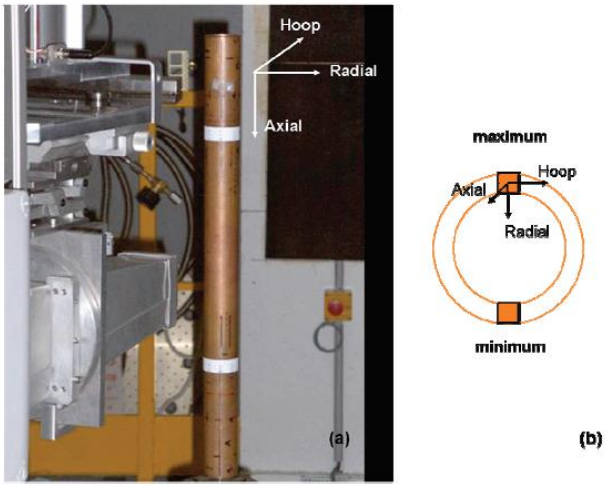


Figure 2.24 Residual stress procedure by the ND of SF-copper tube [59]

Farrahi et al. [60] analyzed residual stress of re-autofrettage in thick-walled tubes. The behavior of high strength steel DIN1.6959 under loading, unloading was estimated and

modified. Chabche's hardening model was used when loading-unloading was applied to simulate a re-autofrettage process by the FEM. In this study, the surface was prepared when yield criterion as a function of the first stress invariant and Lode angle parameter. The unloading behavior was determined according to the damage, first stress invariant and the pervious plastic deformation history. The results proved that the residual stress distribution with a high autofrettage percentage can be improved and an autofrettage process is not beneficial with low autofrettage percentage for residual stress improvement.

Palkowski et al. [61] did a study on tube cold drawing with and without a plug to evaluate residual stress numerically and experimentally. Three dimensional finite element models (3DFEM) with ABAQUS software was developed to link the wall thickness and eccentricity with residual stress. A non destructive neutron strain imaging method was performed to measure the residual stress profile on a series of the SF-copper tubes drawn under controlled and reproducible laboratory conditions. The study gave a good agreement between the FEM and the ND method for the tube drawing process with and without a plug.

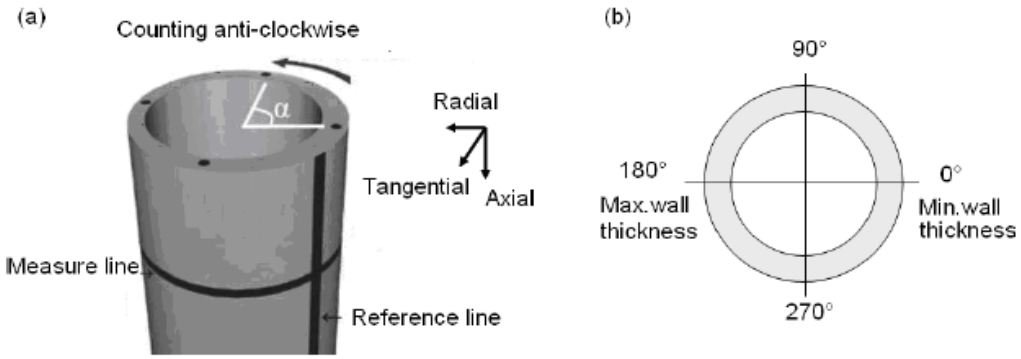


Figure 2.25 (a) Point measurement, and (b) measuring points over circumference [61]

Shekoofa et al. [62] applied a metal ring model with different sizes using the AFEM by running COMSOL software to estimate residual stresses of a mismatched seal between borosilicate glass 3.3 and stainless steel as well as validation of results in relation to the experiment results. The work showed that residual stress levels are strongly influenced as the metal ring thickness decreases and as the glass tube wall thickness increases.

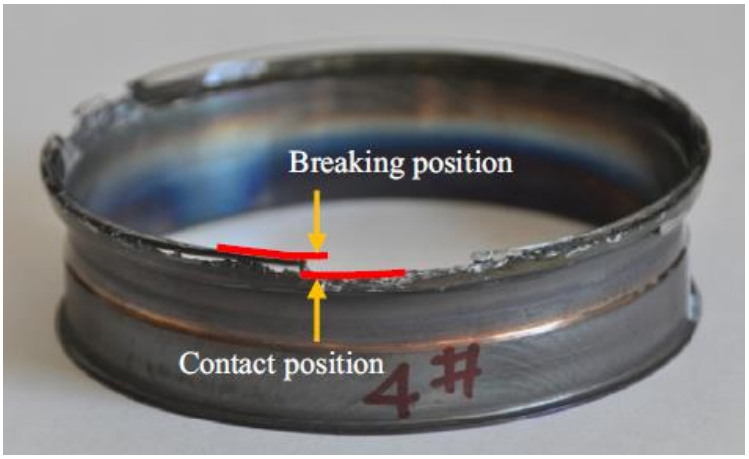


Figure 2.26 Metal ring that is harmed due to the residual stress [62]

Foadian et al. [63] applied the FEM, hole drilling, and ND methods using as-received tubes to study the effect of tilting of the die and shifting of the tube on the eccentricity and residual stress. The residual strains according to the axial, radial, and hoop directions were determined as presented in Fig. 2.28. The study proved that an increase of the tilting angle lead to diminishing increases in residual stress.

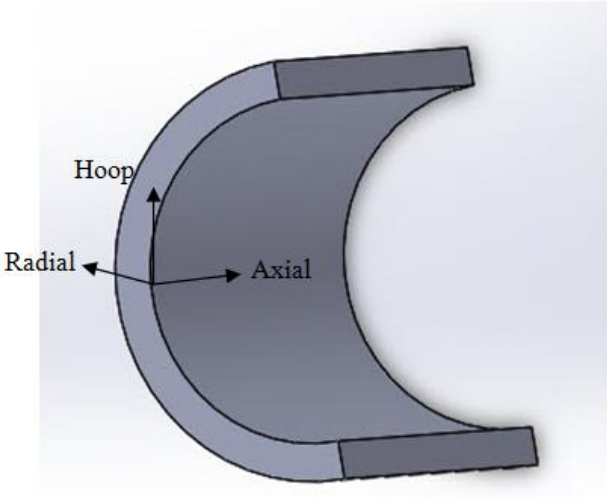


Figure 2.27 Directions of the internal stresses inside tube wall

Foadian et al. [64] measured residual stress over the wall thickness in cold drawn copper tubes using the ND and the FEM. The residual stresses in the axial, radial, and hoop directions were determined from an as-received state in the deformation zone with tilted dies. In an ND procedure, -5° tilted die was measured that was validated

with FEM, then other tilted dies were used. The results showed that there was a good agreement between the measurements and calculations of residual stress.

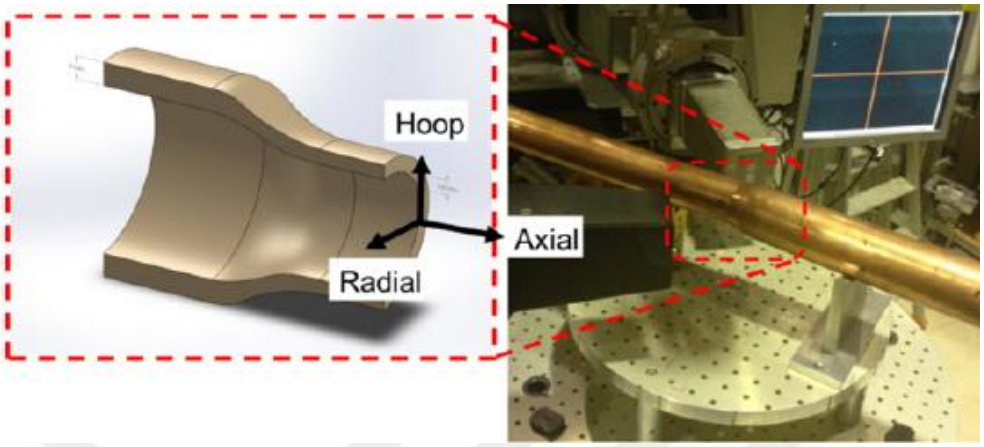


Figure 2.28 Residual stress measurement by ND on the forming zone [64]

According to the previous studies that were presented in this chapter, there are significant deficiencies when determining the residual stress inside the tube wall thickness experimentally as well as difficulty in understanding the behavior of these residual stresses. Some of these studies completely depend on the FEM while the majority of experimental studies focus on using nondestructive techniques that are prohibitively expensive to measure the residual stresses. However, these have limitations in the measurement of residual stress within the depth of the tube wall. Few studies applied destructive and semi destructive methods to determine residual stresses within the tube wall. That being said, the exact depth of residual stress inside the tube wall needs to be determined to a high level of accuracy. The parameters of the nib die and the fixed plug needs to be linked with drawing stress. Therefore, for this Ph.D. study the analysis of tube drawing with a fixed mandrel has been chosen to determine residual stress distribution within the tube wall utilizing various methods.

CHAPTER 3

EXPERIMENTS: TESTS, MEASUREMENTS, AND PROCEDURES

3.1 Introduction

This chapter deals with all experiments that include measuring, designing, and manufacturing as well as residual stress measurement using various techniques. A spectrographic test, tensile test, and a macro hardness test for the raw material of an AISI 1010 steel tube are presented. Design and manufacture of both the dies and mandrels are shown. A tube drawing process with a fixed mandrel having two reduction areas is displayed under lubricated condition. Compression test to measure force with time is given. A macro hardness test for the nib die, the plug, and final tubes produced with R= 16% and 23% is presented. According to the TRSG, residual strain measurements within the tube wall using milling process are explained. The steps of preparation of surface samples at the outer and inner surfaces of the tube are shown. The installation steps of the TRSG at the outer and the inner surfaces of the tube are given in details. The connections of wires to the data logger device by quarter bridges and on to the TRSG are depicted. Two methods, RLM and SM, are introduced to measure residual strain where after the residual stress is determined. In addition, residual stress measurements below the tube surface using the XRD in the five orientations are explained.

3.2 Raw Material of AISI 1010 Steel Tube

Before embarking on the design and manufacture of the tube drawing tools, it is necessary to identify the type of raw material and variable dimensions for the initial tubes. Since the raw material of the tubes is subject to the loads and heat during the preparation, the raw material must be examined by three procedures, which are: the spectrographic test to find the chemical composition, the tensile test and the hardness test to determine mechanical properties.

3.2.1 Spectral Test

The spectrographic test was investigated to evaluate chemical composition for each element that was found in the raw material of the tubes using an S9 Atlantis device as described in the Appendix A. Five samples were prepared and measured where after the average for each element was calculated to show the type of material. The samples were taken from the raw material of the initial tube. These samples were then tested using a spectrographic device that has software enabling reading of the ratio of each element. Fig. 3.1a and 3.1b refer to the raw material and spectrographic test respectively.

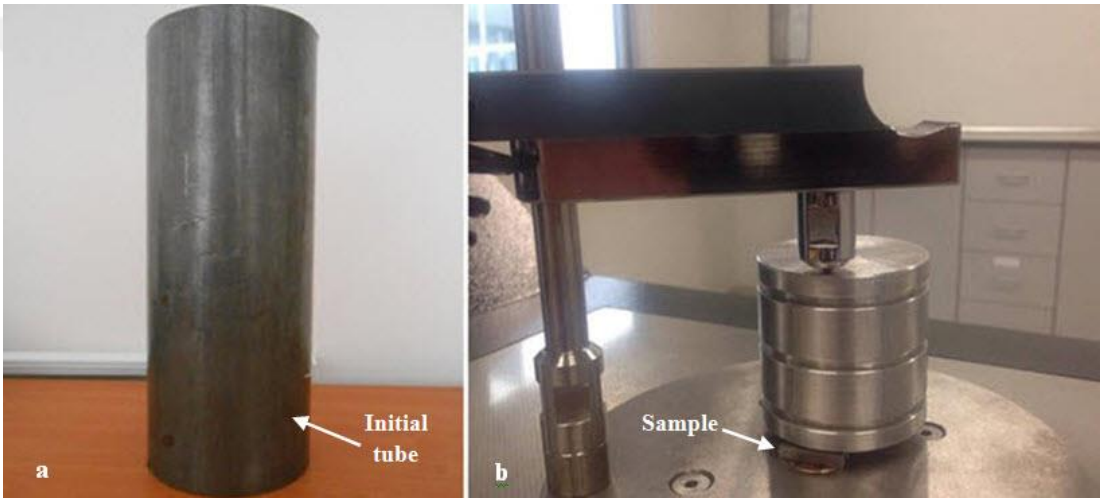


Figure 3.1 (a) Raw material of tube, and (b) the spectral test

3.2.2 Tensile Test

A tensile test was carried out at room temperature in order to estimate yield stress, ultimate tensile stress, and engineering stress vs. engineering strain plot using a tensile device that has a maximum force of 10 ton. In this study, the sample for tensile testing was prepared by sectioning raw material using CNC water jet cutting from the initial tube as shown Fig. 3.2.

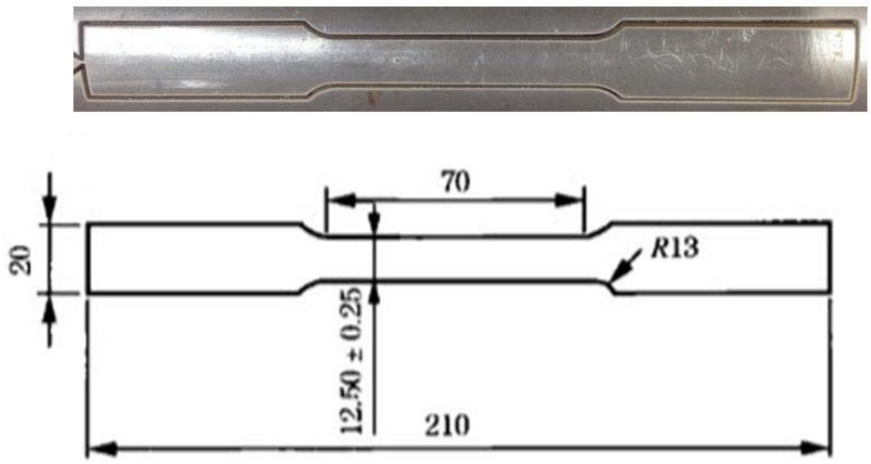


Figure 3.2 Sample dimensions of tensile test

3.2.3 Macro Hardness Test

A macro hardness test was performed to determine the hardness of the initial tube using a macro hardness tester. The device Q250 MS that standardizes hardness testing was used since it has the ability to measure hardness of materials with the Vickers, Brinell, and Rockwell tests. Because the type of raw material for the initial tube is AISI 1010 low carbon steel, Brinell (HBW) was selected and the measurements were repeated three times as pointed out in Fig. 3.3. The Q250 MS hardness device is displayed in Appendix B.



Figure 3.3 Macro hardness test of the raw material

3.3 Designing and Manufacturing of Tools Tube Drawing with a Fixed Mandrel

3.3.1 Dies

The die includes two parts as presented in Fig. 3.4: first, a nib die that performs the main part of the tube drawing process since the contact occurs between the internal surface of the nib die and the external surface of the tube. In other words, the selection of the nib die parameters is very important. The parameters of the nib die are as follows: die drawing angle, radius of the nib die entry and bearing length. The die drawing angle strongly affects the drawing process, especially on drawing force [46]. It is selected according to the type of tube material, drawing velocity, and lubrication, while the radius of the nib die entry depends on the outer diameter of the initial tube to ensure the smooth entry of the metal to the forming area throughout the drawing process. Bearing length must be larger than twice or three times of the final tube wall thickness to obtain a high smoothness of the metal at the exit of the forming area (die 2 and die 1) as shown in Table 3.1. The second part is the die block that surrounds the nib die. Fig. 3.5 presents a die that produces a tube with an outer diameter of 76 mm.

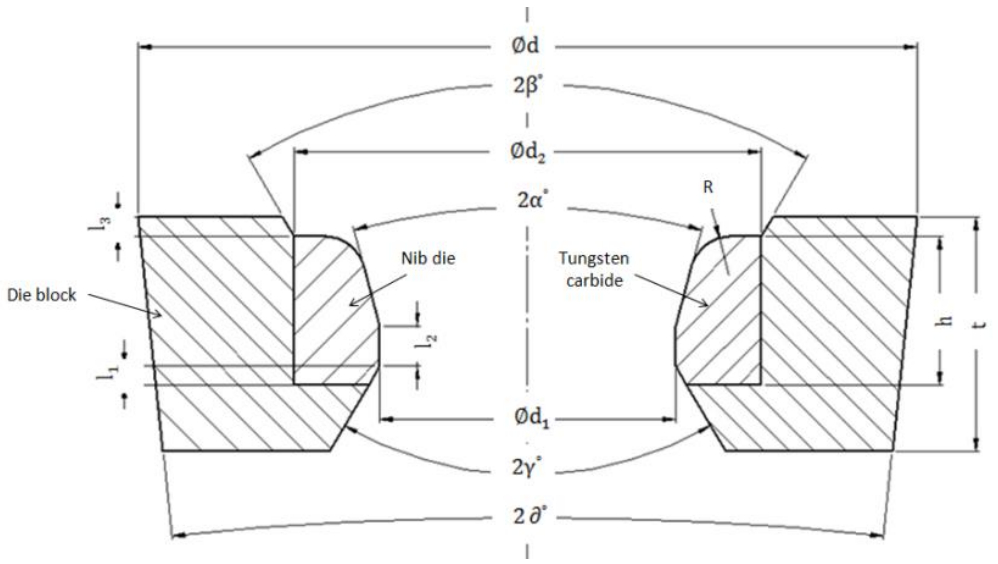


Figure 3.4 Section of die drawing

Table 3.1 Dimensions for two dies

Symbol and Description	Die 1	Die 2	Symbol and Description	Die 1	Die 2
d_1 : hole diameter of the nib die	76 mm	70 mm	I_3 : block length from the nib die	5 mm	3.5 mm
d_2: outer diameter of the nib die	120 mm	105 mm	2α: die drawing angle	30°	30°
d_3 : outer diameter of the die block	200 mm	185 mm	2γ: exit die angle	60°	60°
h: thickness of the nib die	38 mm	35 mm	2β: inner block angle	60°	60°
t: thickness of the die block	60 m	52.5 mm	2∂: outer block angle	12°	12°
I_1: exit length	5 mm	3.5 mm	R : radius of the nib die entry	10 mm	7 mm
I_2: bearing length	10 mm	7 mm			

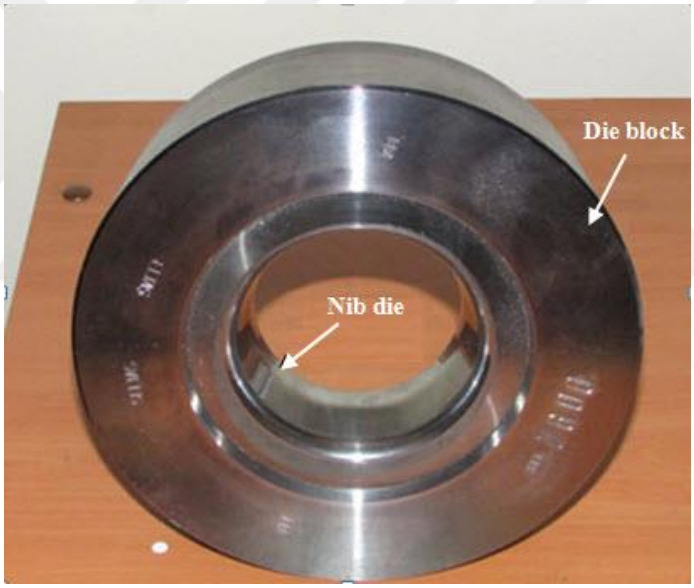


Figure 3.5 Picture of die drawing produced outer diameter of 76 mm tube

3.3.2 Mandrels

For the fixed straight mandrel (cylindrical mandrel) as shown in Fig. 3.6, there are three parts: rod, fixed plug, and nut. The main part is the fixed plug because of the contact between the external surface of the plug and the internal surface of the tube during the drawing process. The thickness and length of the plug depend on the inner diameter of the final tube and length of the nib die. In this study, the length of the plug

is larger than the length of the nib die is selected to allow for further uses with different nib dies in future plans as introduced in Table 3.2. The rod consists of three parts, the first one that has the largest diameter, which represents the arm. The second part has a smaller diameter where the plug is superimposed, while the third part is the one with the smallest diameter and has a screw to be connected with a nut to fixate the plug to the rod. Fig. 3.7 displays the mandrel that was manufactured with an outer plug diameter of 70 mm.

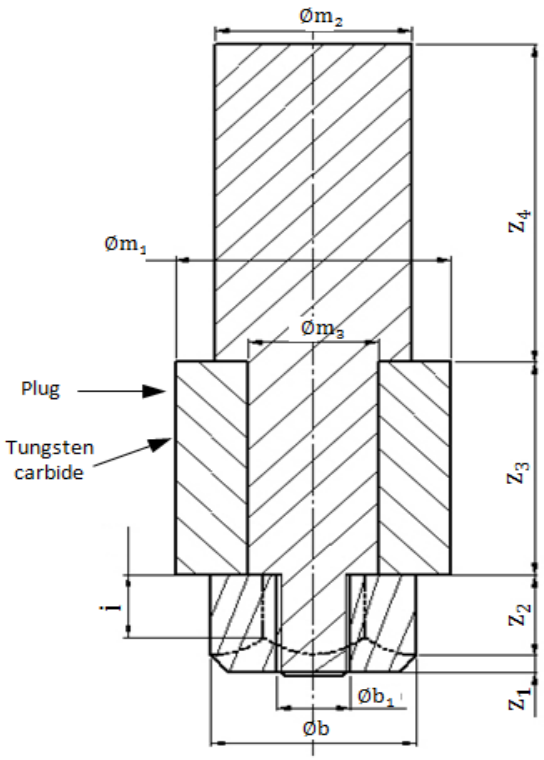


Figure 3.6 Section of the fixed straight mandrel

Table 3.2 Dimensions for two mandrels

Symbol and Description	Mand 1	Mand 2	Symbol and Description	Mand 1	Mand 2
m_1: outer plug diameter	70 mm	64 mm	z_3: length of plug	61 mm	53.5 mm
m_2: rod diameter	50 mm	44 mm	z_4: length of rod (arm)	91 mm	83 mm
m_3: inner of plug diameter	33 mm	30 mm	b_1: diameter of bolt	18.5 mm	16.8 mm
z_1 : fillet of nut	5 mm	4.6 mm	b: width of nut	52 mm	48 mm
$z_1 + z_2$: length of screw	28 mm	25.6 mm	i: length of nut	18 mm	16.5 mm

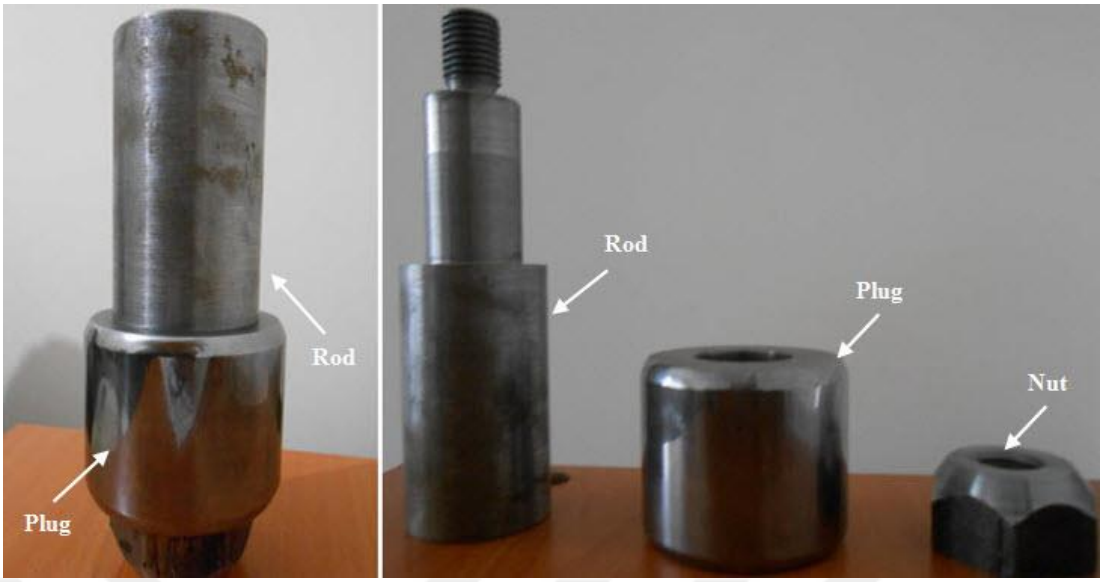


Figure 3.7 Pictures of the mandrel with outer plug diameter 70 mm

The nib die and the fixed plug were made of cemented carbide since it has the ability to resist abrasion while 4140 steel was used to manufacture the die block and rod of the mandrel. The mechanical properties of cemented carbide are as follows: density 15.59 g/cm^3,Poisson's ratio 0.21 and Young's modulus 650 GPa while the density of 4140 steel is 7.85 g/cm^3, Poisson's ratio 0.3 and Young's modulus 210 GPa. Because the tools are made of cemented carbide, macro hardness test using Rockwell (HRC) was also performed to test the nib die and the plug.

3.4 Experimental of Tube Drawing Process with a Fixed Mandrel

Initial tube dimensions were 78×3.5 mm and 71 mm (outer diameter × wall thickness and inner diameter) and were reduced to final dimensions 76×3 mm and 70 mm respectively which represent R=16% with reduction of tube wall thickness H=14.2% as reported in Tables 3.1 and 3.2 with die1 and mandrel1, respectively. In addition, the dimensions of the initial tube were decreased to 70×3 mm and 64 mm that represent R=23% with H=14.2% as displayed in Tables 3.1 and 3.2 with the die2 and mandrel2, respectively. According to the available material, there were three different initial tube lengths: 3.8 m, 2.0 m, and 4.1 m. The first two were drawn to stretch a final length of 4.6 m, 2.4 m respectively with R=16%, while the third was drawn to a final length of 5.47 m with R= 23%. R=16% and 23% were calculated according to Eq. 2.1 that was

shown in chapter two, Appendix C presents calculations for R=16% and 23%. Before assembling the tools and tube with die support, the area of the initial tube was reduced to allow the tube to pass through the nib die.

Three steps must be followed to assemble the tools with a bench drawing system. First, the tooling was assembled during connection of the die block with the die support. Second, the tube was placed inside the nib die. Both die support, and tube cavity were covered by mineral oil to decrease friction during the process. Finally, the mandrel was positioned inside the tube. Fig. 3.8 illustrates the assemble die, tube, and mandrel inside the die support.

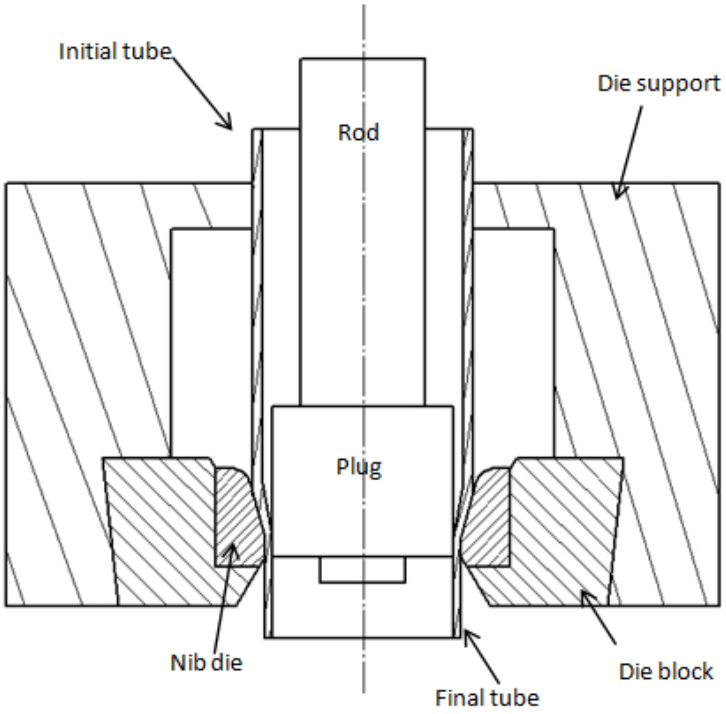


Figure 3.8 Schematic representation of the die support, die, tube and mandrel

The tube location was between the nib die and the plug, and then the chain-driven cold drawing machine started to draw the tube. Tubes were drawn at a constant speed of 4.25 m/min at different lengths for two reductions of area and at the constant reduction of tube wall thickness H=14.2%. A commercial mineral oil was used as a lubricant during the process.

Fig. 3.9 shows the die located in the die support (bench machine) while Fig. 3.10 refers to the mandrel tolerances in the nib die with die support and die bench.

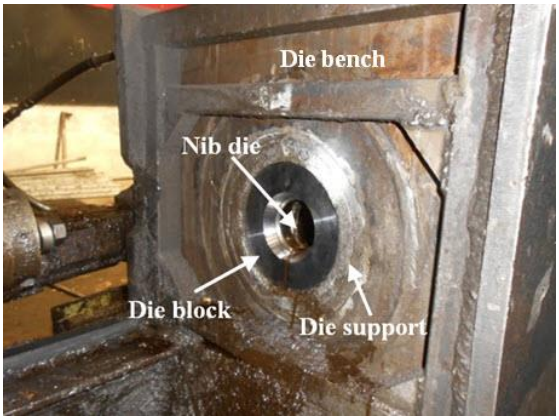


Figure 3.9 Picture of die located in the die support



Figure 3.10 Pictures of mandrel tolerance for the nib die with die support

Fig. 3.11 presents initial tube placed inside of the nib die with a commercial mineral oil then mandrel is fixed inside of tube.



Figure 3.11 Pictures of initial tube covered by the commercial mineral oil

Fig. 3.12 displays the tube drawing process using a chain driven cold drawing machine.

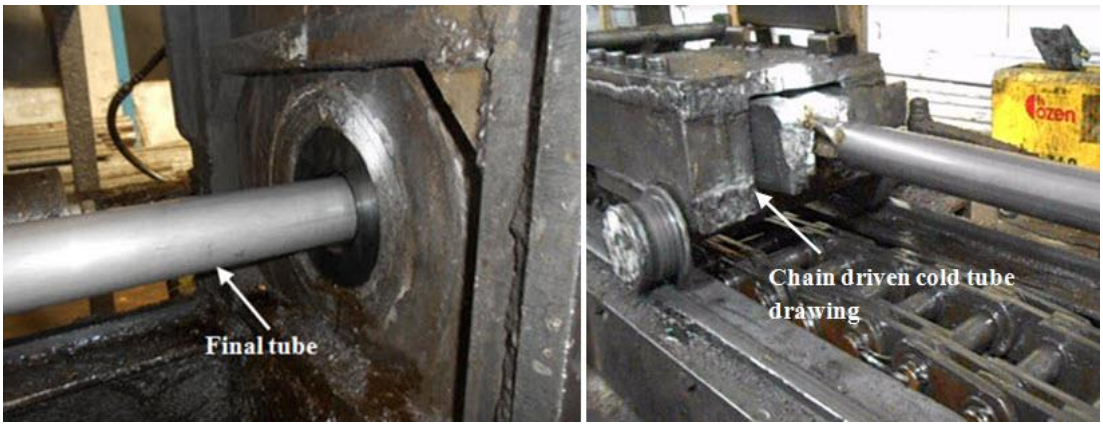


Figure 3.12 Pictures of the chain driven cold tube drawing process

The macro hardness test using Brinell (HBW) tester was performed for the final tubes that were produced with R=16% and 23% to show the changes in hardnesses of tubes after the production.

Due to the difficulty of using a load cell with a chain-type cold drawing machine, the compressive test was conducted to identify the force with time under the same drawing conditions. According to the variable press and because of the difficulty in setup of the tools with compression device, low velocity 0.0286 mm/s was applied for R=16% while 0.03 mm/s was used for R= 23% to compress the initial tube. In this test, just the die and fixed plug were used as illustrated in Fig. 3.13.

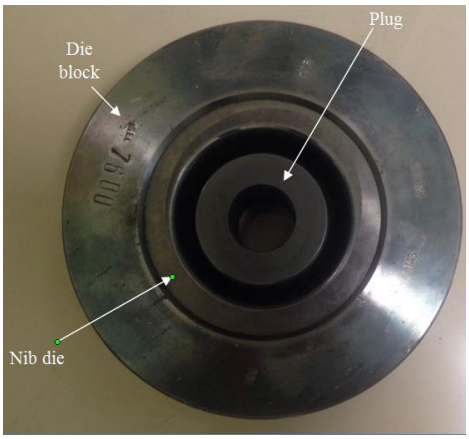


Figure 3.13 Die and plug setup for compression process

The length of initial tube is 70 mm and after compression, the tube moves to 20 mm for R=16% and moves to 16.5 mm for R=23% to ensure that buckling will not occur during the test. Fig. 3.14 shows the compression test for the initial setup. Moreover, Fig. 3.15 presents the tube samples after compression for R=16% and 23%.

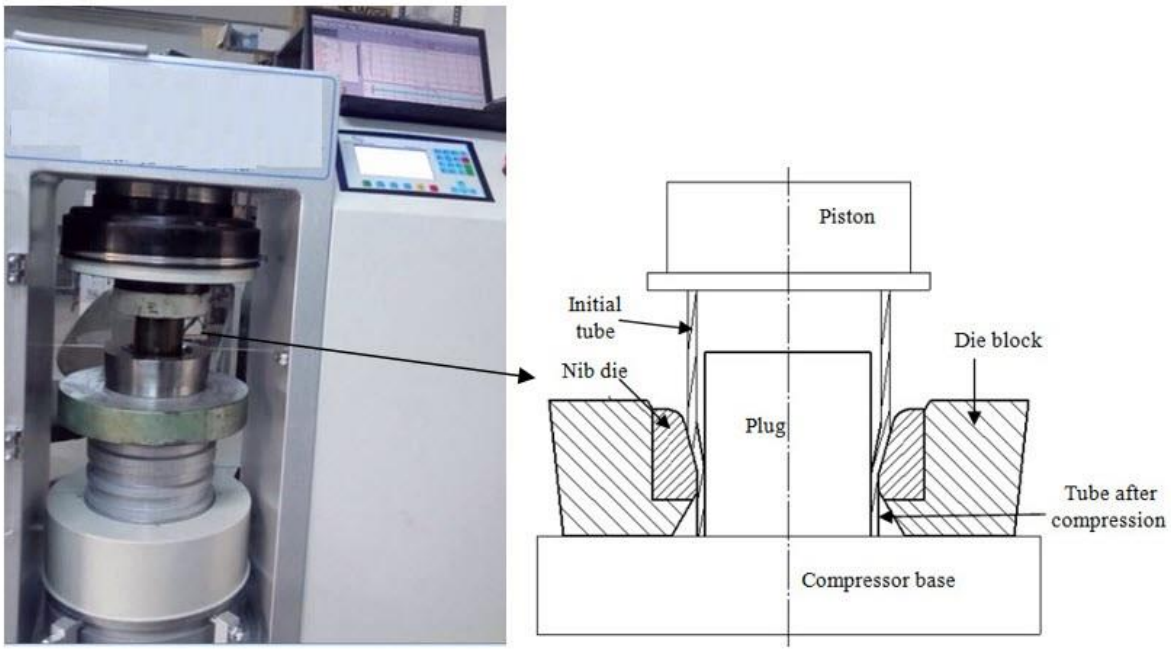


Figure 3.14 Compression test to measure force

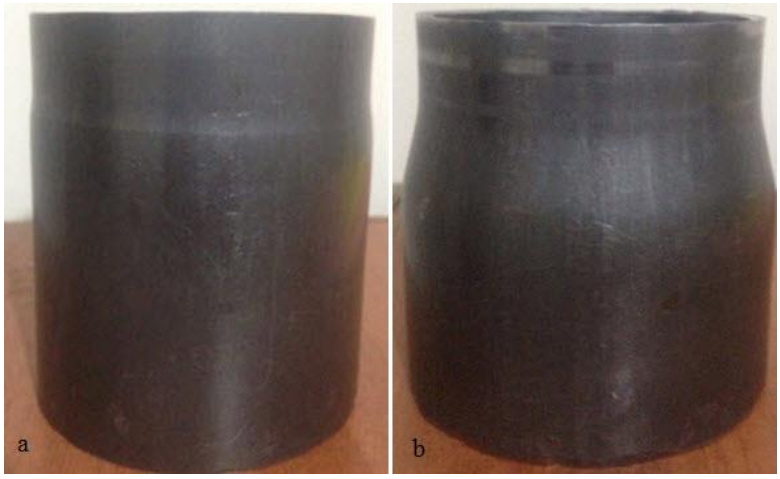


Figure 3.15 Tube samples after the compression (a) R=16% and (b) R=23%

3.5 Residual Stress Measurement within Tube Wall Thickness Using Destructive Technique (The RLM and The SM Methods)

Residual stresses tend to introduce a reduction of stability in strength and leads to fatigue and eventually to fractures. Measurements of residual stresses in the various phases of the tube drawing process permit approximate predication of magnitudes and distributions while experimental methods are the most important for reaching dependable, real-world conclusions. Therefore, residual stresses within the tube wall were measured experimentally using the destructive technique by using two methods. The first, the RLM using a milling process was used to measure axial and hoop residual strains by applying the TRSG. The second, the SM was performed to measure residual stress in one direction. Appendix D introduces the specifications of the TRSG.

3.5.1 TRSG for the Determine Residual Stress

The longitudinal (axial) strain and tangential (hoop) strain inside the tube wall can be determined by Eq. 3.1 and 3.2 [28].

$$\varepsilon_L = \frac{L_1 - L_o}{L_o} \qquad (\mathbf{3.1})$$

$$\varepsilon_T = \frac{D_1 - D_o}{D_o} \qquad (\mathbf{3.2})$$

where ε_L and ε_T are longitudinal and tangential strain respectively, $L_1 - L_o$ represents the change in the length of the tube, and L_o is the original length. While $D_1 - D_o$ is known the change in the diameter of the tube, and D_o represents the original diameter of the tube.

The change in length and diameter of the tube can be measured by the micrometers with low accuracy. Strain gage can give high accuracy in the strain measurement if the setup of the strain gage on the sample surface is correctly fixed with accurate directions.

Although, the RLM and the SM need strain gages with two and one directions respectively, the available strain gage type was a TRSG 120 Ω that suited the available data logger device. Taking this into consideration, the TRSG was applied with the RLM and the SM.

A TRSG application is based on a strain measurement that can describe residual strain within the tube wall according to the change in dimensions. A TRSG or $\boldsymbol{xy}$ strain gages have 2 measuring grids arranged at a 90° offset each other. Typical applications for this type contain analysis of principal strains when the principal directions are known. There are important characteristics which must be taken into consideration in the selection of strain gage. Optimal choice of gage length and grid width are very important in the measurement operation. A TRSG was applied with gage length 3.18 mm and grid width was 4.19 mm for each section. For metal, a gage length of 2-6 mm can be used.

When strain is measured in a specimen by the strain gage, which is attached to the surface, the strain is relayed via the gage base (electrical insulation) to the resistance wire in the gage. As a result, in the fine wire there is a variation in electrical resistance. This variation is exactly proportional to the strain.

$$\varepsilon = \frac{\Delta L}{L} = \frac{\Delta R / R_g}{K_f} \qquad (\mathbf{3.3})$$

where ε is strain measured, R_g represents the gage resistance, ΔR indicates to the resistance change due to the strain and K_f is the gage factor. For metal, K_f can be taken 2-5.

Normally, this resistance change is very small and requires a Wheatstone bridge circuit to convert it to voltage output. For a TRSG, two bridges must be used.

$$R_1 = R_o + \Delta R \qquad (\mathbf{3.4})$$

$$R_2 = R_o - \Delta R \qquad (\mathbf{3.5})$$

$$\Delta e = \frac{E_v}{2} K \varepsilon \qquad (\mathbf{3.6})$$

R_o is the resistance before stain generation, ΔR refers to the resistance change due to the strain, Δe indicates to the output voltage due to the strain and E_v is exciting voltage.

According to the Hooke's law, the strain can be calculated according to the Eq. 3.7, 3.8, and, 3.9 for the isotropic material.

$$\varepsilon_{xx} = \frac{1}{E}\left[\sigma_{xx} - v\left(\sigma_{yy} + \sigma_{zz}\right)\right] \quad (\mathbf{3.7})$$

$$\varepsilon_{yy} = \frac{1}{E}\left[\sigma_{yy} - v(\sigma_{xx} + \sigma_{zz})\right] \quad (\mathbf{3.8})$$

$$\varepsilon_{zz} = \frac{1}{E}\left[\sigma_{zz} - v\left(\sigma_{xx} + \sigma_{yy}\right)\right] \quad (\mathbf{3.9})$$

In tube section, ε_{zz} is very close to zero, so that the residual stress by *z*-axis is neglected. In Eq. 3.7, because the residual stress acts in the *x*-direction, the σ_{yy} and σ_{zz} equal zero. Also in Eq.3.8, the residual stress acts in the *y*-direction the σ_{xx} and σ_{zz} are zero. The stresses that act of their directions are shown in Eq. 3.10, 3.11. [65].

$$\sigma_{xx} = E\varepsilon_{xx} \quad (\mathbf{3.10})$$

$$\sigma_{yy} = E\varepsilon_{yy} \quad (\mathbf{3.11})$$

σ_{xx} and σ_{yy} are stresses with *x* and *y* directions respectively, ε_{xx}, ε_{yy} represent strains measurements with *x* and *y* directions, and E is Young modulus. In this study E for AISI 1010, steel is 200 GPa.

In this study, three procedures were followed to investigate the measurements. The first procedure is the sample surface preparation for the bonding area of the tube before the attaching of the TRSG. The second procedure is the installation of the TRSG and connecting it to the quarter bridge and data logger. The final procedure is the use of a CNC milling machine to measure residual strain by the RLM and by the SM, where after residual stresses are calculated.

3.5.1.1 Surface Sample Preparation

18 samples were prepared to measure residual stresses; the length of each sample being 30 cm. 9 samples were produced by R=16% and the other calibrated by R=23%. For each reduction of area, nine samples were provided for using both the RLM and SM. 12 samples were equipped to fix the TRSG at the outer surfaces of the tube, six of them for R=16% and the others for R=23%. 6 samples were provided to put the TRSG at the inner surfaces of the tube, three of them with R=16% and the others with R=23%.

The bonding area needs a good preparation to obtain an accurate measurement. All grease, rust, paint, pitting, scratches, and protrusions were removed from the bonding area using 4130 abrasive paper, which is used with alloy steel components. Industrial tissue paper with a cloth soaked in a small quantity of M-prep conditioner A-metal cleaner and M-prep neutralizer 5A were applied to clean the bonding area of the tube surface as pointed out in Fig. 3.16. 3M novec electronic degreaser was also used to clean and to remove all grease.

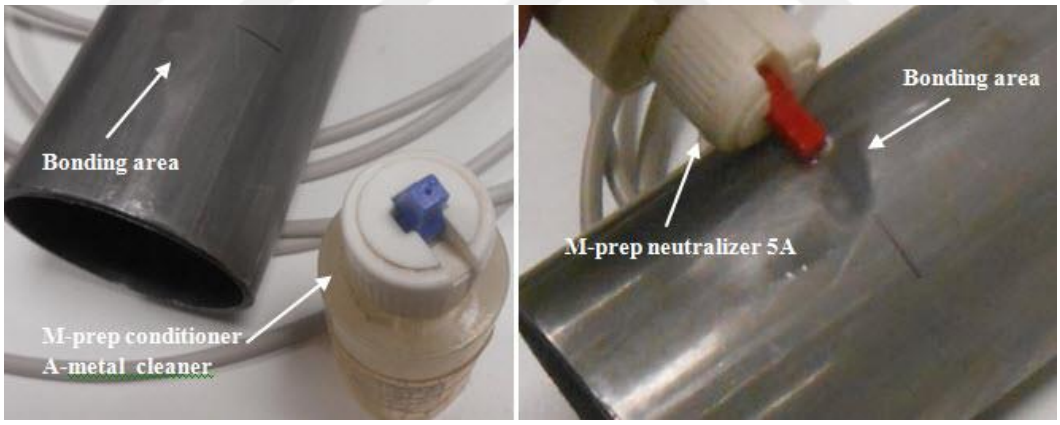


Figure 3.16 Cleaning bonded area with M-prep conditioner A and M-prep neutralizer 5A

The cleaning continued until a new tissue or cloth came away completely free of contamination. This procedure was repeated three times for each sample on the inner and outer surfaces to obtain a good bonding area as shown in Fig. 3.17. Following the surface preparation, the TRSG must be attached before the surface becomes covered with an oxidizing membrane or contamination.

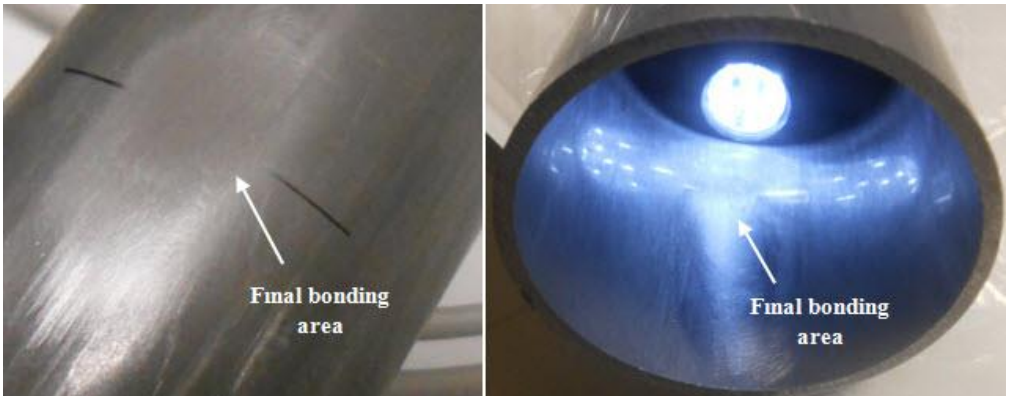


Figure 3.17 Bonding areas after the cleaning for both of external and internal surfaces of tube

3.5.1.2 Attaching of the TRSG on the Bonding Area

Installation of the TRSG is a delicate process that needs high accuracy when attaching it onto the surface. In this study, the TRSG was fixed to both the outer and the inner surfaces of the tubes. For the outer attachment on the bonding area, the location of the TRSG was selected 5.5 cm from the edge of the tube while for the inner fixing on the bonding area, a location for the TRSG was chosen 3.5 cm from the edge of the tube.

The position of the TRSG should be at the exact location of the gage direction while also ensuring that the bonding area is totally clean without contamination. For final installation, the M-Bond 200 adhesive is placed at the bonding area as displayed in Fig 3.18.

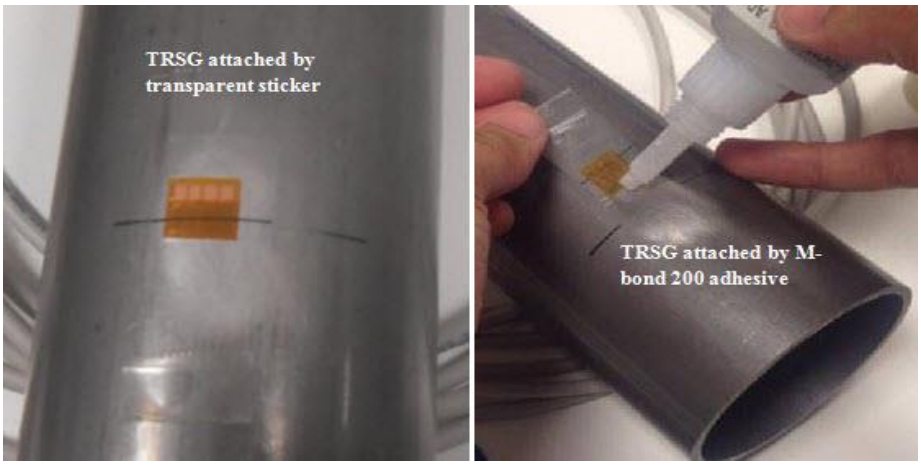


Figure 3.18 TRSG bonded by transparent sticker then by M-Bond 200 adhesive

After fully fixing of the TRSG on the bonding area, it was checked using an RMS Multimeter to ensure accurate functioning. Fig. 3.19 illustrates the final bonding of the TRSG at the outer and the inner surfaces of the tube.

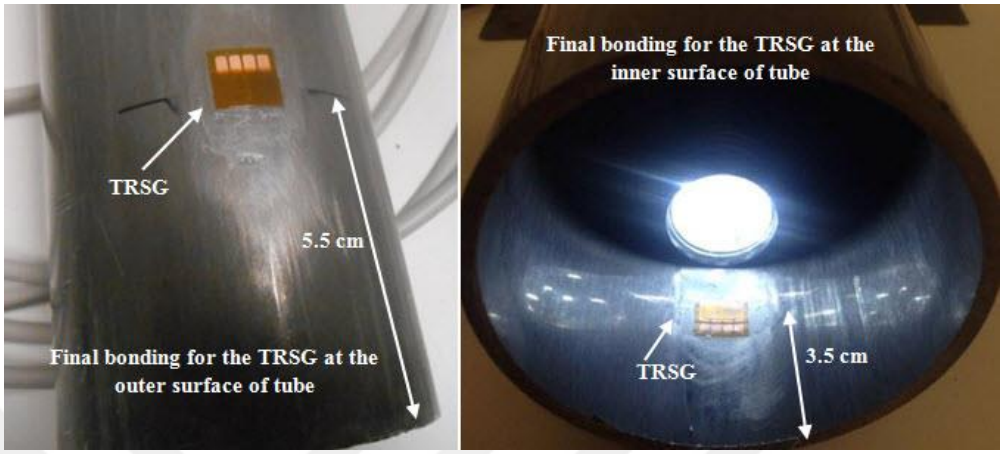


Figure 3.19 Final bonding for the TRSG at the outer and the inner surfaces of tube

3.5.1.3 Soldering Extension Lead Wires with the TRSG

With the TRSG, a cable with three paralleled wires for each section must be selected. It is very important to estimate extension lead wires with the TRSG. Fig. 3.20 refers to the soldering of lead wires with the TRSG.

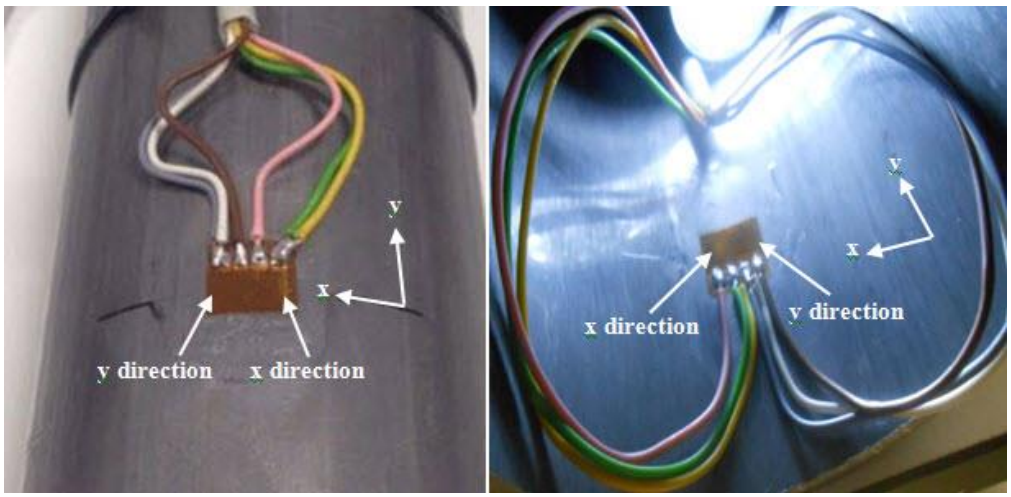


Figure 3.20 Soldering extension lead wires with the TRSG at the outer and the inner surfaces of tube

As show in Fig. 3.20, directions of strain were determined in the *x* direction (hoop strain) and *y* direction (axial strain). After the wires were soldered, the TRSG was cleaned again. Consequently, the wires were checked using a RMS Multimeter to ensure accurate connections.

3.5.1.4 Insulating and Covering of the TRSG

In this Ph.D. study, a strain gage was used to measure strain by removing layer on the tube incrementally using a CNC milling machine. This process necessitates the use of fluid coolant to prevent the heat generation that can produce thermal stress during the process with a high speed cutting tool. There is a great need to protect the strain gage from the coolant fluid and chips to ensure accurate readings of strains during the milling of layers. For this purpose, two materials were applied for the insulation and cover of the strain gage. The first material is M-coat A to isolate the TRSG from the coolant fluid. Fig. 3.21 shows TRSG covered by M-coat A.

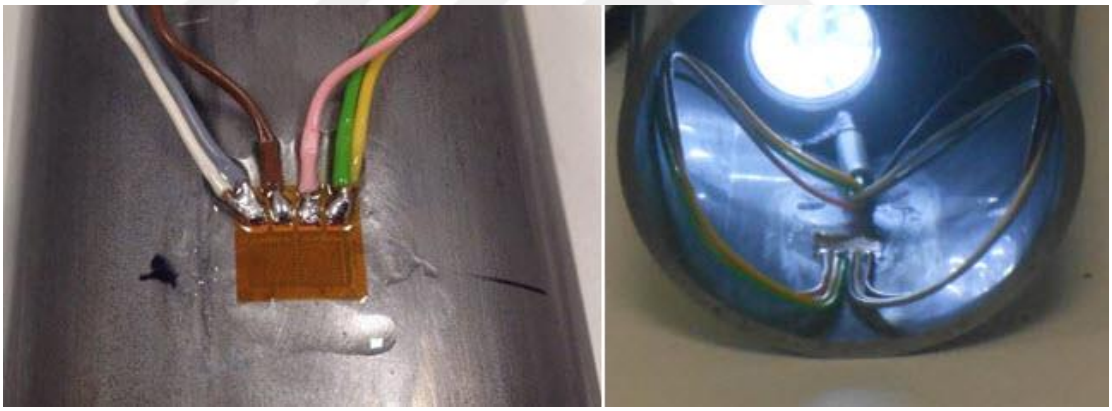


Figure 3.21 TRSG covered by M-coat A

The second material was DOW CORNING 3145 RTV MIL-A-46146 Adhesive/Sealant. This material represents the main layer of protection that is directly in contact with the coolant fluid and chips through the process. The TRSG was completely covered by this material and has the ability to prevent the coolant fluid from reaching the inside of the strain gage as pointed out in Fig. 3.22. The samples were left for 24 hours until the coating cured.

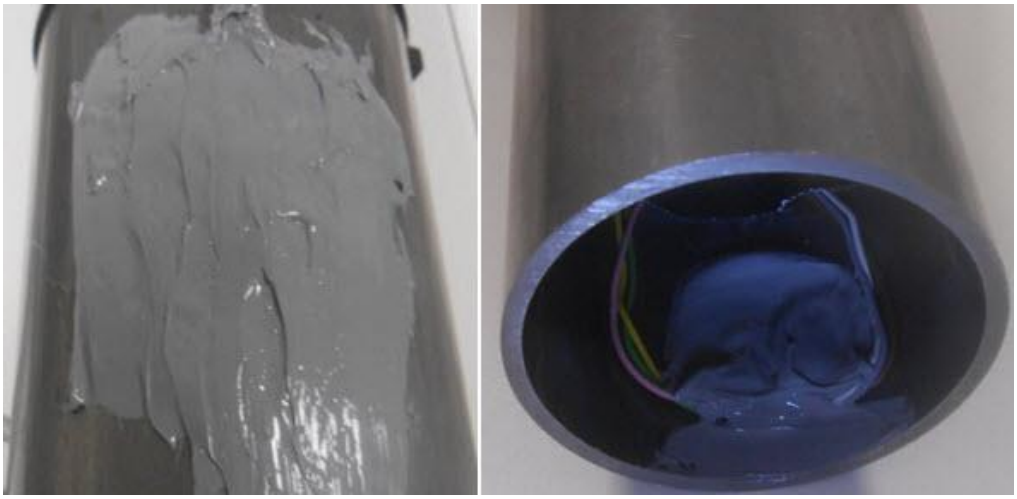


Figure 3.22 TRSG covered by DOW CORNING 3145 RTV MIL-A-46146

3.5.1.5 Connecting Extension Lead Wires with Data Logger Device

After the TRSG were installed at the outer and the inner surfaces of the tube for the different samples, the wires of the other sides must be connected with quarter bridges and then to the data logger device. This connection connects to the bridge that converts resistance to strain. Before the wires are connected, the quality and specifications of the device that is used in the measurements must be identified. In this study, DEWE 43-A was utilized to measure the strains with a 120 Ω resistance on the quarter bridges. Specifications of DEWE 43 A are displayed in Appendix E. The TRSG connects with a cable that includes three wires: two wires for signal transmission and another for the excitation. The connections between each TRSG, quarter bridges, and data logger must be compatible. Fig. 3.23 presents the data logger DEWE 43 A.



Figure 3.23 Data logger device (DEWE 43 A)[66]

From the Fig. 3.23, it can be seen that there are 8 channels that can be used to measure resistance. Strain can be measured by using bridges. On the side of the data logger, there are connections for a power adapter, a USB adapter connected to the computers, common GND for electrical safety, and Sync for connections with other devices. According to the DEWE 43 A software, the values of strain can be read and recorded for each section in the gage.

The wires from the bridge sides must be soldered to an analog adapter that includes a 9-pin D-SUB female to connect with a quarter bridge that has an analog adapter and includes an 9-pin D-SUB male.

Fig. 3.24 shows the full connections for the wires and two-quarter bridges with data logger.

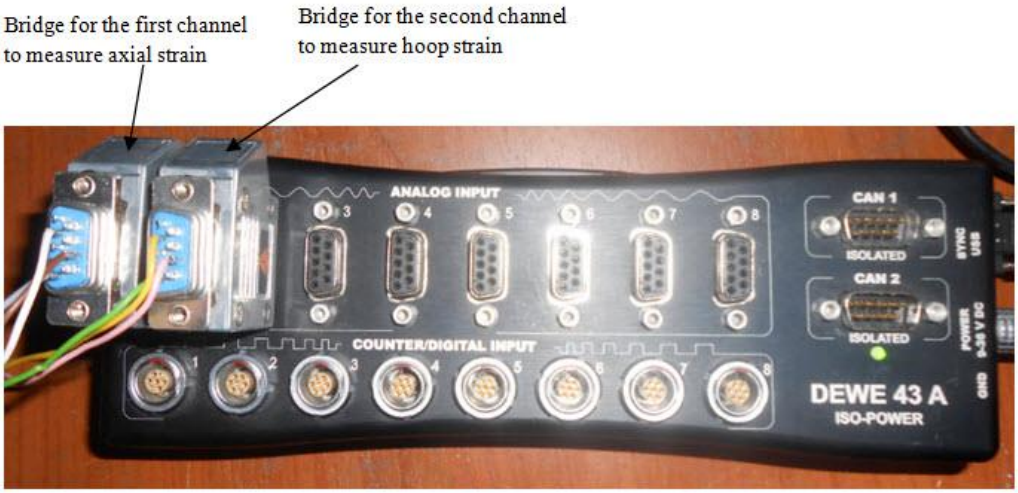


Figure 3.24 Connections of the wires and two bridges with a data logger device

3.5.2 Residual Stress Measurement Using Milling Process

In this study, a CNC milling machine under lubricated conditions was used to mill the tube walls of the final tubes using two methods. First, the RLM was utilized to remove layers from the inner and the outer surfaces as the TRSG at the outer and the inner surfaces of the tubes were respectively attached. Second, the SM was used to make a slot on the upper part of the tube wall, and a TRSG was fixed at the bottom of the outer surface of the tube wall.

3.5.2.1 Residual Stress Measurement by the RLM to Mill Layers from the Inner and the Outer Surfaces of the Tube Wall

The RLM was used to measure strain with circumferential (hoop) and longitudinal (axial) directions. In using this method, two procedures were applied for the measurements. In the first procedure, a cutting tool on a CNC milling machine was utilized to remove layers from the inner surface of the tube while the TRSG was attached at the outer surface of the tube as depicted in Fig. 3.25.

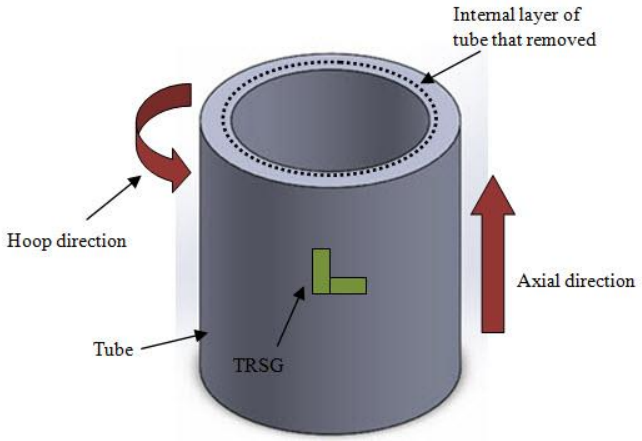


Figure 3.25 Removing layer from the inner surface of tube

In the second procedure, layers of tube wall from the outer surface were removed by the cutting tool on a CNC milling machine and the TRSG being fixed on the inner surface of the tube as shown in Fig. 3.26.

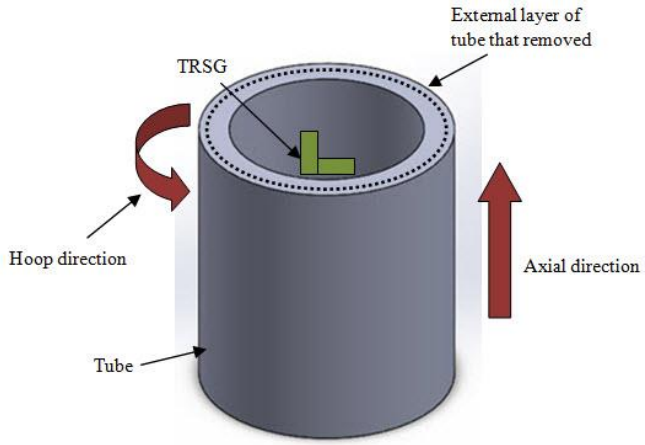


Figure 3.26 Removing layer from the outer surface of tube

For the two procedures, 0.25 mm of tube wall was removed for each milled layer. Hoop and axial strains were measured according to the change in diameter and length of the tube when the cutting tool was milled. The depth of milling was incrementally recorded for each measurement. The cutting speed was 314 mm/min and a feed rate of 2345 mm/min for internal milling was chosen. For external milling, a cutting speed of 314 mm/min and a feed rate of 2888 mm/min were applied. The diameter of the cutter was 50 mm and the cutting tool was WKP35 that is used for steel and cast iron. The lengths of the layers which were removed were 120 mm internally and 100 mm externally. Fig. 3.27 illustrates the cutting tool that was used to remove layers from the inner and the outer surfaces of the tube.



Figure 3.27 Cutting tool for the inner and the outer surfaces of the tube

For internal milling, removal of layers started incrementally from the inner surface for all samples. The tube thickness of 3 mm was decreased to be 1.5 mm with least measurement. For each layer that was removed, hoop and axial strain and timing data were recorded according to the quarter bridges after which the average value was taken for each measurement in connection with the milling depth. This process was performed for three samples of the tube, which were produced with R=16%, and three samples that were formed with R=23%. Fig. 3.28 presents the RLM by internal milling of the tube wall using CNC machine.

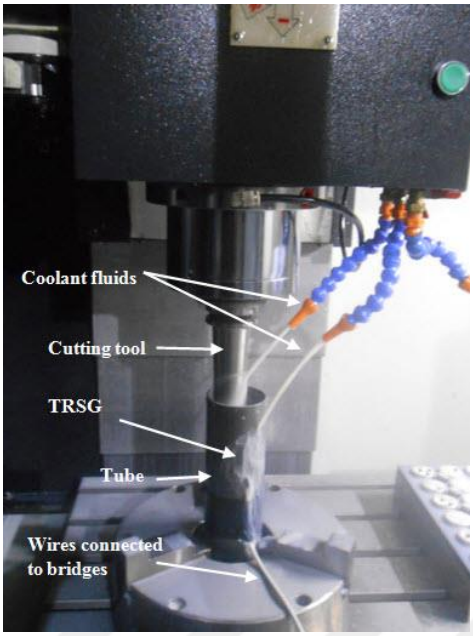


Figure 3.28 The RLM by internal milling using CNC machine to measure strain

The same procedure that was indicated for internal measurements was performed for the external measurements except for the removal of layers starting from the outer surface. The final tube wall thickness also came to 1.5 mm with the last milling of the layers. This process was also done for three samples, which were calibrated with R=16%, and three samples that were obtained with R= 23%. Fig. 3.29 displays the RLM by external milling of the tube wall using a CNC machine.

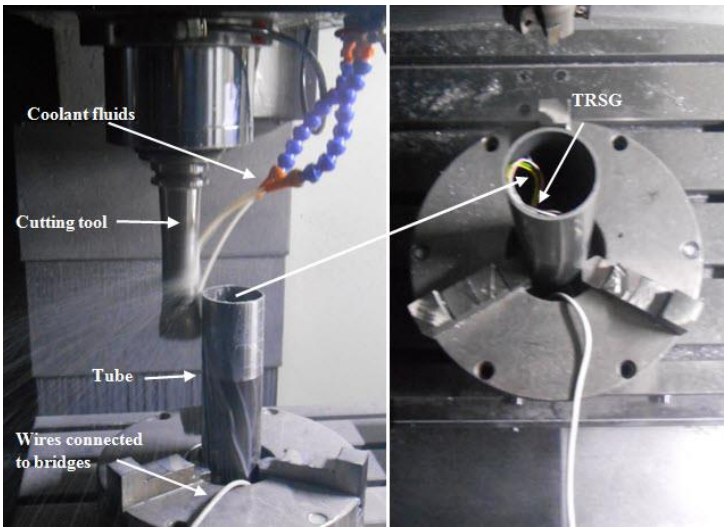


Figure 3.29 The RLM by external milling using CNC machine to measure strain

Fig. 3.30 refers to the connections for the wires to the bridges with the data logger and further connected to a computer (measurement system). It can be seen that the computer screen displays the behavior of the axial and hoop strain and timing data.

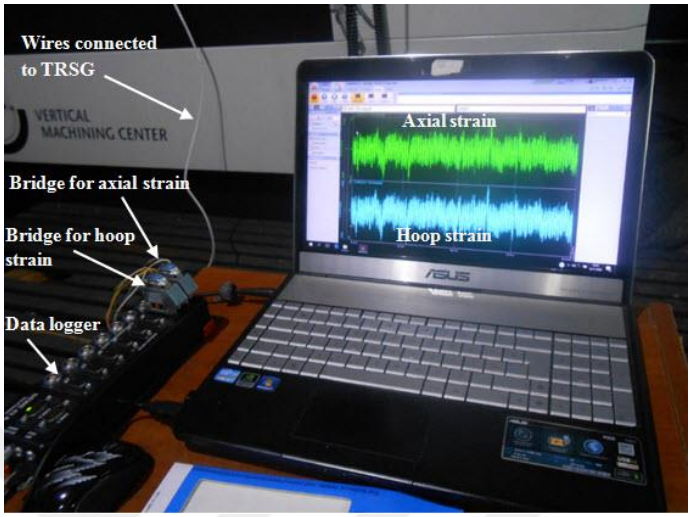


Figure 3.30 Measurement system of axial and hoop strain by data logger

3.5.2.2 Residual Stress Measurement by the SM Using Milling Process

The SM is a method for residual stress measurement in the specimen wall by cutting a thin slot incrementally deep through the wall and measuring the result as a function of slit depth. In this study, a CNC milling machine was used to make a slot on the outer surface of the tube when the TRSG was fixed at the bottom of the outer surface of the tube to measure hoop strains as pointed out in Fig. 3.31.

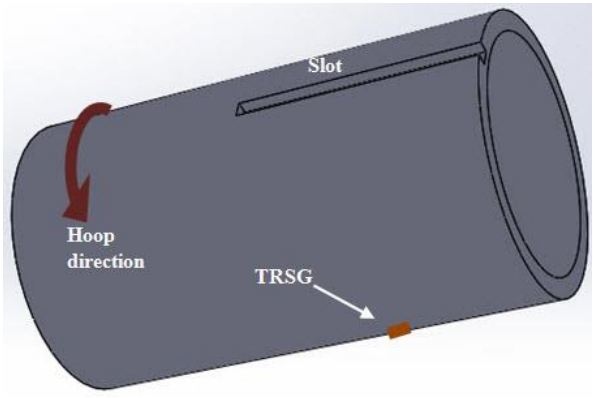


Figure 3.31 Slitting method according to the TRSG

The experimental measurement by this method was achieved for six samples. Three samples, which were formed with R=16%, and the other produced with R=23%. A carbide-milling cutter with a diameter of 4 mm was utilized to make a slot with cutting speed 56 mm/min and feed 143 mm/min. The carbide cutter is shown in Fig. 3.32.



Figure 3.32 Carbide milling cutter with 4 mm diameter

In the procedure of the SM, a 0.3 mm depth of milling from the tube wall for each measurement was made. The length of the slot was 120 mm for all measurements. The strain measurements for the hoop direction were recorded according to the change in the diameter of the tube. Fig. 3.33 illustrates slotting using a CNC milling machine to measure strains.

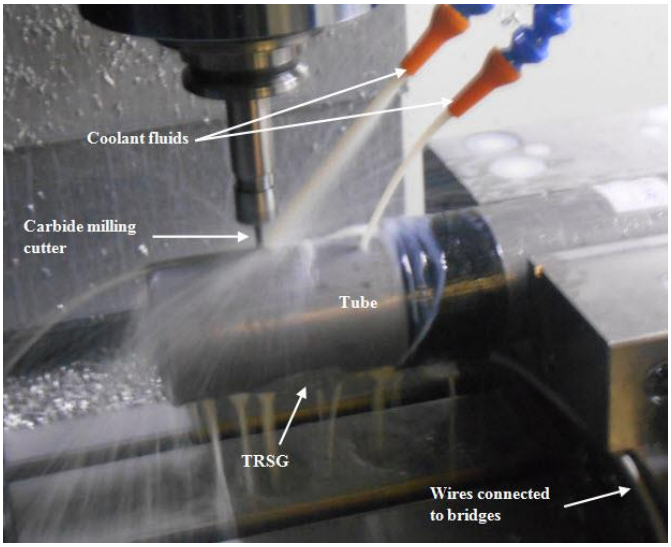


Figure 3.33 The SM using CNC milling machine

3.6 Residual Stress Measurement Using Non Destructive Technique by XRD Method

A non destructive X-Ray diffraction (XRD) technique was used to determine residual stress below the tube surface. In the XRD measurement, the crystalline structure of the sample is subjected to X-Rays, the maximum angles at which these are diffracted are then measured and the interplanar spacing of the crystals can be obtained using Bragg's law Eq. 3.12.

$$n\lambda = 2d\ sin\theta \qquad (\mathbf{3.12})$$

where n is an integer denoting the order of diffraction, λ is the x-ray wavelength, and d is the lattice spacing of crystal planes.

In this study, samples were prepared to determine residual stress below the outer and the inner surfaces of the tube as well as inside of the wall for the samples that were produced with R=16 % and 23%. For surface sample preparation, the area of the tube $400\ mm^2$ $(20\times20mm)$ was selected then the samples for the measurement were sectioned with their original convex upper surfaces and concave bottom surfaces preserved as displayed in Fig. 3.34.

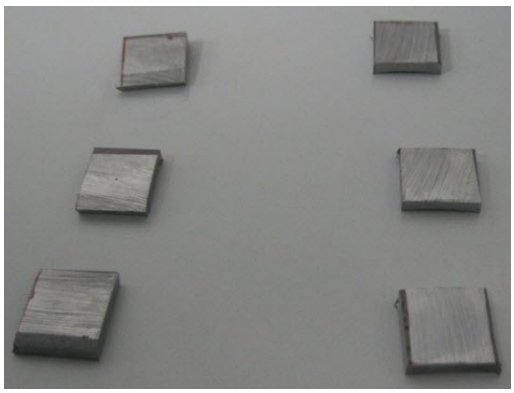


Figure 3.34 Preparing samples for XRD measurement

Because of the range of XRD measurement 10-20 μm below of surface depending on the material, polishing process can be used to remove layers from tube thickness then residual stress can be measured [66]. In this study, a heavy abrasive process on the

concave and convex surfaces was performed to remove layers and to obtain the flattened surfaces. Then a finer abrasive on these surfaces was applied to remove the stresses that can be generated due to the effect of the heavy abrasive process. This process continues until scores over the surface are minimized to near zero. *SiC* abrasive pads with grit sizes 180, 240, 400, 600, 800, 1000, 2000, and 3000 were used. Finally, after applying the 3000 grit abrasive, ethanol was applied to clean the surface. After preparation of the sample surfaces, each sample positioned in the X-Ray holder as featured in Fig. 3.35.

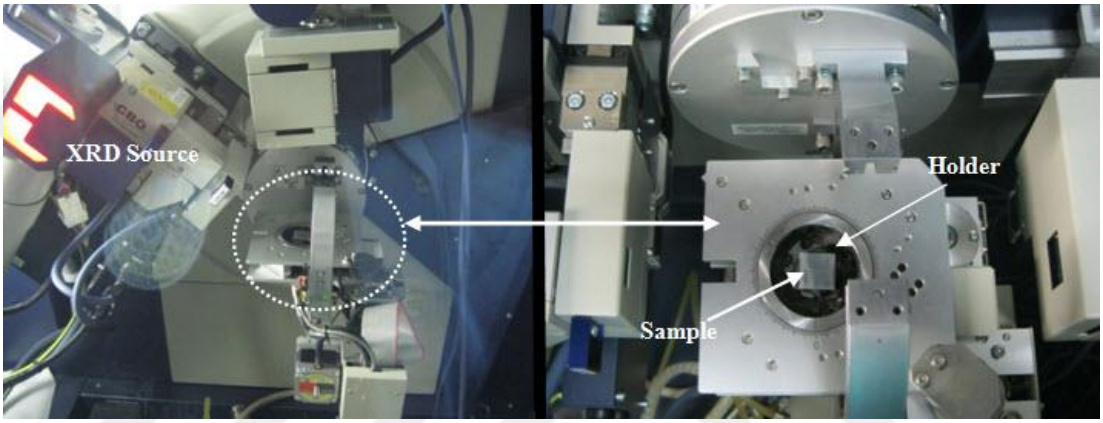


Figure 3.35 Sample positioned in the X-Ray holder machine

Because of the tube wall is 3 mm that leads to the difficulty in axial measurement, residual stress by hoop direction was only measured. The difference between spacing in the stressed and unstressed state is proportional to the magnitude of the residual stress. The residual stress was estimated by assuming a linear elastic distortion of the associated crystal lattice plane in proportion to the strain in the crystal lattice. The stress was then measured using the elastic constant. An energetic beam of particles or radiation aimed at a metallic target material produces the X-Rays. The metallic target conducts electrons and different materials are used for the X-Ray powder such as chromium (*Cr*) and Copper (*Cu*). These materials radiation ($K\alpha$), $K\alpha$ is 2.29 for *Cr* while 1.54 for *Cr*.

According to Fig. 3.36, (2θ) is a high diffraction angle from the surface of a stressed sample for two orientations of the sample relative to the x-ray beam and is termed peak angle while Ψ is termed tilt angle which is defined by the angle between the normal to

the diffracting lattice planes and sample surface. In Fig. 3.36, D is the X-Ray detector, S is x-ray source, and N is normal for the surface. In Fig. 3.36 (a) it can be seen that in the Ψ=0 orientation, there is a slight increase in the diffraction angle (2θ) while in Fig. 3.36 (b) the source of diffraction and detector were rotated and $\Psi \neq 0$. The tensile stress present on the surface increases as the lattice spacing over the stress-free state decreases (2θ).

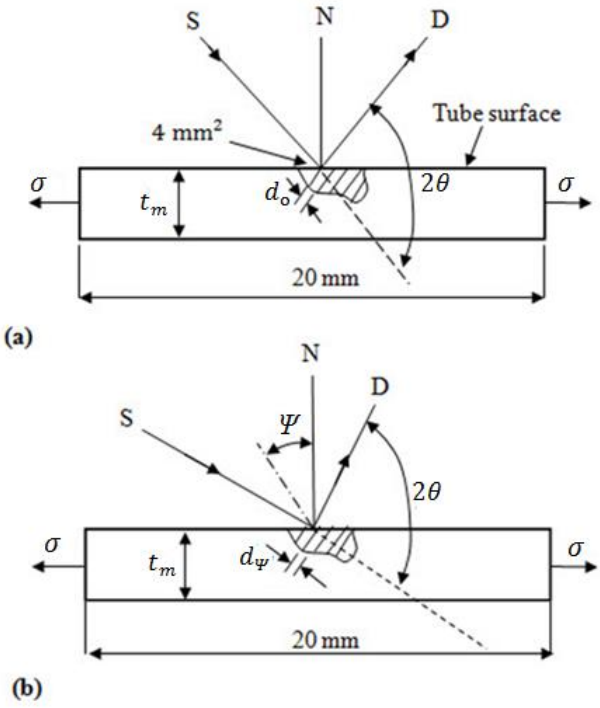


Figure 3.36 XRD stress measurement inside the tube wall. (a) Ψ=0, (b) $\Psi \neq 0$

The stress present in the sample surface lying in the plane of diffraction that includes the incident and diffracted X-Ray beams is calculated by the angle Ψ according to the change in measuring and the change in angular position of the diffraction peak of at least two orientations of the sample. The source of diffraction and detector are rotated about its normal surface to coincide with the direction of interest in the diffraction plane to measure the stress in different directions at the same point. The linear dimensions of the crystal lattice represent the strain as shown in Eq. 3.13.

$$\epsilon_{\emptyset\Psi} = \left[\frac{\Delta d}{d_o} = \frac{d_{\emptyset\Psi} - d_o}{d_o}\right] = \left[\frac{1+v}{E}(\sigma_\emptyset sin^2\Psi)\right] - \left[\left(\frac{v}{E}\right)(\sigma_1 + \sigma_2)\right] \qquad (\mathbf{3.13})$$

d_o is defines the stress-free lattice spacing, the spacing between the lattice planes measured $d_{\emptyset\Psi}$ with direction $\emptyset$ and Ψ, $\sigma_{\emptyset}$ represents the surface stress at any direction according to the angle Ψ to the strain ϵ, in the direction $(\emptyset, \Psi)$, the principal stresses (σ_1, σ_2) in the surface, E is Young's Modulus and v is Poisson's ratio. When the surface angle is zero ($\emptyset = 0$), $\epsilon_{\emptyset\Psi}$ can be calculated as indicated in Eq. 3.14, [68].

$$\epsilon_{\emptyset\Psi} = (\epsilon_{11} - \epsilon_{33}) sin^2\Psi + \epsilon_{33} \qquad (\mathbf{3.14})$$

ϵ_{11} is parallel strain and ϵ_{33} is strain out of plane perpendicular. In this study, the samples were not rotated in order to save time. Therefore, both the detector and source were rotated so that the surface angle was zero ($\emptyset = 0$). Table 3.3 refers to the rotations of $\Psi°$ and $2\theta°$ axes that were used during rotation of the source.

Table 3.3 Rotations of $\Psi°$and $2\theta°$ axes

$\boldsymbol{\Psi°}$	$\boldsymbol{sin^2\Psi}$	$\boldsymbol{2\theta°}$
-45.0	-0.5	136.736
-36.5	-0.354	136.736
-29.0	-0.235	136.738
-20.0	-0.117	136.722
0	0.00	136.716

The residual stress determined by the XRD is the arithmetic average stress in the area defined by the dimensions of the X-Ray beam. In this study, an irradiated area between 4-6 mm^2 was used for all measurements and position of measurement 150 mm from tube edge at R=16% and 90 mm from tube edge at R=23%. In order to determine the intensity at an accuracy of 1% at a single point on the diffraction peak, 10^{-4} x-rays must be counted, regardless of the time required. In this measurement, fixed time was applied equal 20 s for each measurement of the diffraction peak. The copper target metal $Cu\ K\alpha$ was chosen to measure strains. Measurement of residual stresses at different depths of the tube wall with different samples was performed. A multipurpose XRD system that was connected with a computer running the required software application was used. Appendix F demonstrates the specifications of the XRD device.

CHAPTER 4

FINITE ELEMENT SIMULATION BY ABAQUS

4.1 Introduction

This chapter addresses the simulation of a tube drawing process with a fixed mandrel (plug) using the FEM. In this chapter, the AFEM by ABAQUS 6.14-2 software is given in detail. Geometrical and material models were introduced according to the dimensions and mechanical properties of both the tools and a thin walled tube. The assembly of the model and steps were presented by explaining stable time increment to understand the efficiency dynamic analysis as well as arbitrary Lagrangin-Eulerian (ALE) adaptive meshing was shown. Interaction and boundary conditions were pointed out. Element and mesh were explained. 3DFEM according to the R=23% is displayed.

4.2 Axisymmetric Tube Drawing with a Fixed Plug Model

A tube drawing process with a fixed mandrel (plug) was modeled by the AFEM using ABAQUS 6.14-12 software to study the effect of the nib die and plug parameters with friction coefficients on drawing stress and to determine residual stress inside the tube wall. In the simulation of models for R=23%, semi die angles 5°, 7°, 10°, 12°, and 15° were selected while semi plug angles 0°, 1°, 2°, 3°, and 4° were chosen. The friction coefficients 0.1, 0.125, and 0.15 were applied between the material and the tool. Also, tube drawing with a fixed mandrel model was performed at reduction of area R=16%, semi die angle 15°, semi plug angle 0° and friction coefficient 0.1. Table 4.1 shows the SI units which are used in model simulation using ABAQUS.

Table 4.1 Simulation model units

Quantity	Length	Force	Mass	Time	Stress	Energy	Density
SI (mm)	mm	N	tonne (10^3 kg)	s	MPa (N/mm^2)	mJ (10^{-3} J)	tonne $/mm^3$

4.2.1 Geometrical and Material Model

The geometry of the tube drawing model with a fixed plug represents an entire circular solid. To accommodate for that, the AFEM was used. In simulation models, three main parts represent the tube drawing process with a fixed mandrel process. These parts are the nib die, the fixed plug, and the thin walled tube. Fig. 4.1 indicates the axisymmetric dimensions of the nib die.

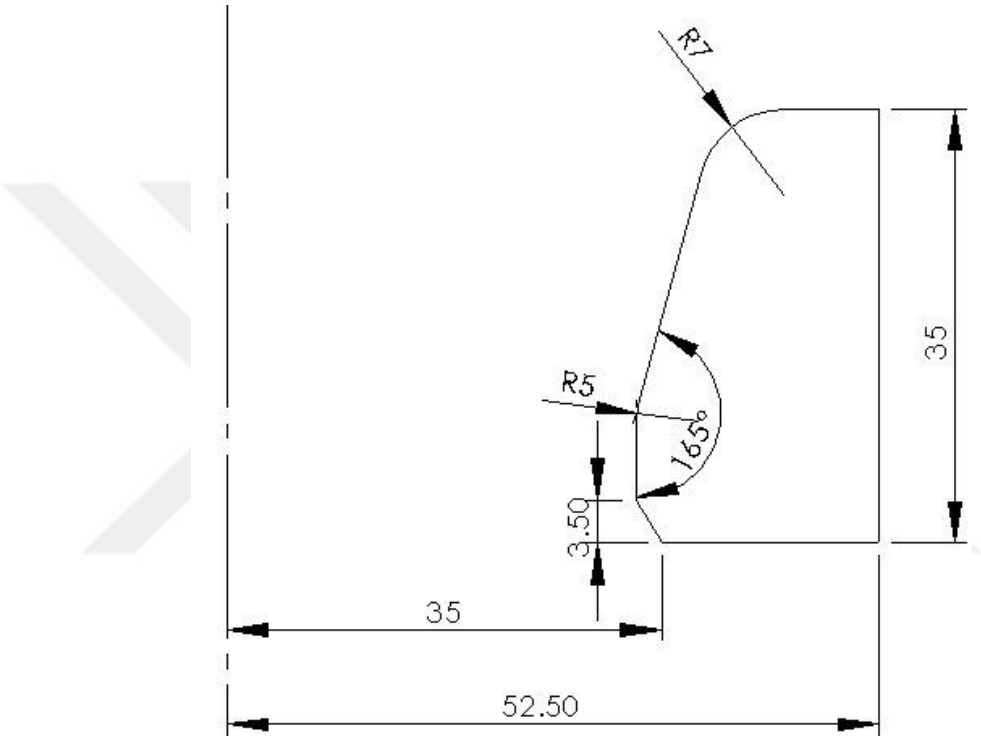


Figure 4.1 Axisymmetric dimensions of nib die by ABAQUS at R=23%

As shown in Fig. 4.1, the hole diameter of the nib die is 70 mm, the outer diameter of the nib die is 105 mm, the thickness of the nib die 35 mm, exit length of 3.5 mm, bearing length of 7 mm, die drawing angle of 30° (semi die angle 15°), and the radius of the nib die entry 7 mm.

Fig. 4.2 displays the dimensions of the fixed plug geometry; semi plug angle is zero, the outer diameter and the length of plug are 64 mm and 53.5 mm, respectively, and the diameter of hole of 30 mm where the rod of the mandrel was placed.

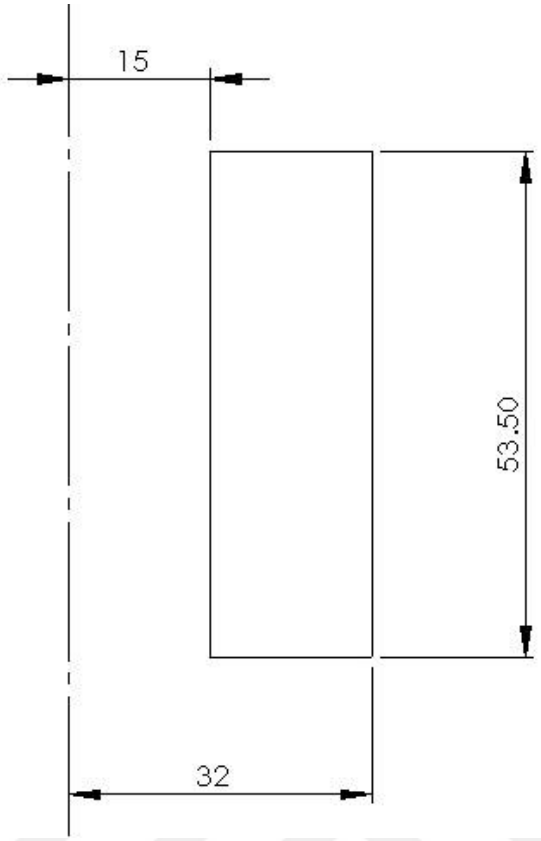


Figure 4.2 Axisymmetric dimensions of plug by ABAQUS at R=23%

Fig. 4.3 presents the initial tube dimensions, the outer diameter 78 mm, the thickness of 3.5 mm, the inner diameter of 71 mm, and the length of 300 mm.

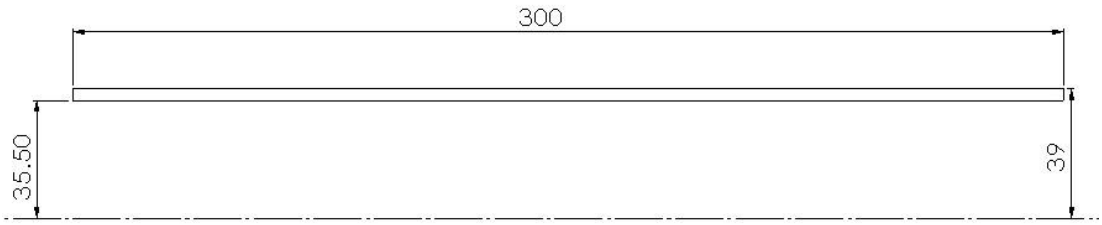


Figure 4.3 Axisymmetric dimensions of initial tube by ABAQUS

The material of the thin walled tube is AISI 1010 steel that has mechanical properties as shown in Table 4.2.

Table 4.2 Mechanical properties of AISI 1010 steel

Density (g/cm^3)	Young's Modulus (E) (GPa)	Poisson's Ratio	Yield Strength (YS) (MPa)	Ultimate Tensile Strength (UTS) (MPa)	Elongation%	Hardness
7.722	200	0.285	560	610.6014	20	132 HBW

Tensile test was performed at room temperature and engineering stress vs. engineering strain plot was determined. Then true stress vs. true total strain plot was calculated in order to determine true stress vs. effective plastic strain that should be used in the simulation.

$$\sigma_{true} = \sigma_{eng} \times [1 + e_{eng}] \quad (\mathbf{4.1})$$

$$(e_{true})_{total} = ln[1 + e_{eng}] \quad (\mathbf{4.2})$$

where σ_{true} and $(e_{true})_{total}$ are true stress and true total strain respectively while σ_{eng} and e_{eng} represent engineering stress and engineering plastic strain respectively. The effective plastic strain can be calculated by Eq. 4.3 where E_y is the modulus equal true stress at yield divided by the true total strain at yield. All magnitudes of stresses and strains are shown in Appendix G.

$$(e_{eff})_{plastic} = (e_{true})_{total} - \frac{\sigma_{true}}{E_y} \quad (\mathbf{4.3})$$

The material of the nib die and the plug was cemented carbide; mechanical properties are displayed in Table 4.3.

Table 4.3 Mechanical properties of cemented carbide

Density (g/cm^3)	Young's Modulus (E) (GPa)	Poisson's Ratio	Elastic Limit (MPa)	Tensile Strength (MPa)	Bulk Modulus (GPa)	Hardness
15.565	600-686	0.2-0.22	355-530	370-530	350-400	71 HRC

The mechanical properties of AISI 1010 steel and cemented carbide as well as elastic-plastic value for AISI 1010 steel are given in ABAQUS. For the thin walled tube, the material was defined as homogenous solid. The section name, section type and region associated with each section assignment were defined. The color green for a region indicates that the region has a section assignment.

4.2.2 Assembly of Model and Step

The assembly definition of the AFEM as shown in Fig. 4.4, the model includes three parts: the nib die, the plug, and the tube. The assembly was mated using the "dependent option" to assemble these three parts. The "translate instance option" was used to move parts to their correct positions.

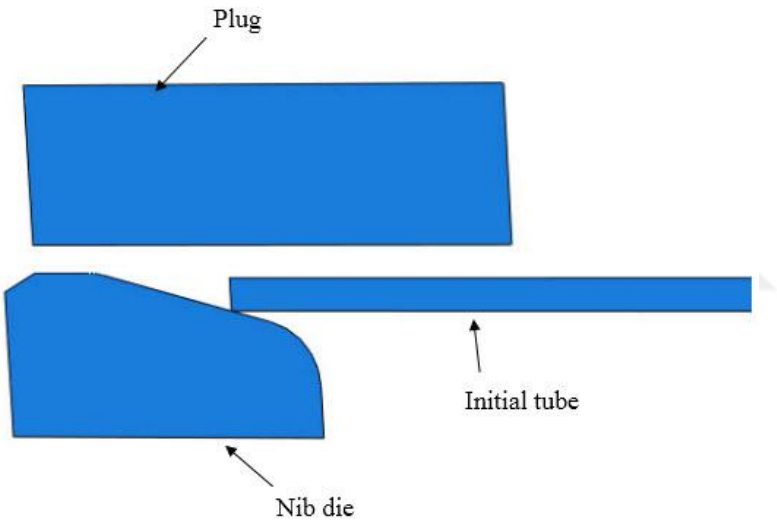


Figure 4.4 Assembly of the AFEM (the nib die, the plug and the initial tube)

A converged solution and nonlinear solution control can be obtained during the definition of a step with the appropriate time increment that gives the best simulation of a tube drawing with a fixed mandrel. In this model ABAQUS/explicit, dynamic was used since it has the ability to readily analyze problems involving complex contact interaction between many independent bodies. ABAQUS/explicit is particularly well-suited for analyzing the transient dynamic response of structures that are subject to impact loads and subsequently undergo complex contact interaction within the structure.

ALE adaptive meshing combines the features of pure Lagrangian analysis and pure Eulerian analysis. Therefore, it can be used with explicit/dynamic that allows maintaining a high-quality mesh throughout dynamic analysis and makes the mesh move independently of the material when a large deformation occurs or losses of material with the mesh topology remaining unchanged. Eulerian adaptive mesh domains are usually used to analyze steady-state processes involving material flow and the mesh covers the same material domain at all times. In ABAQUS/CAE, the option of ALE adaptive mesh domain was selected to add frequency of 10 and remeshing sweeps per increment of 3 as displayed in Fig. 4.5.

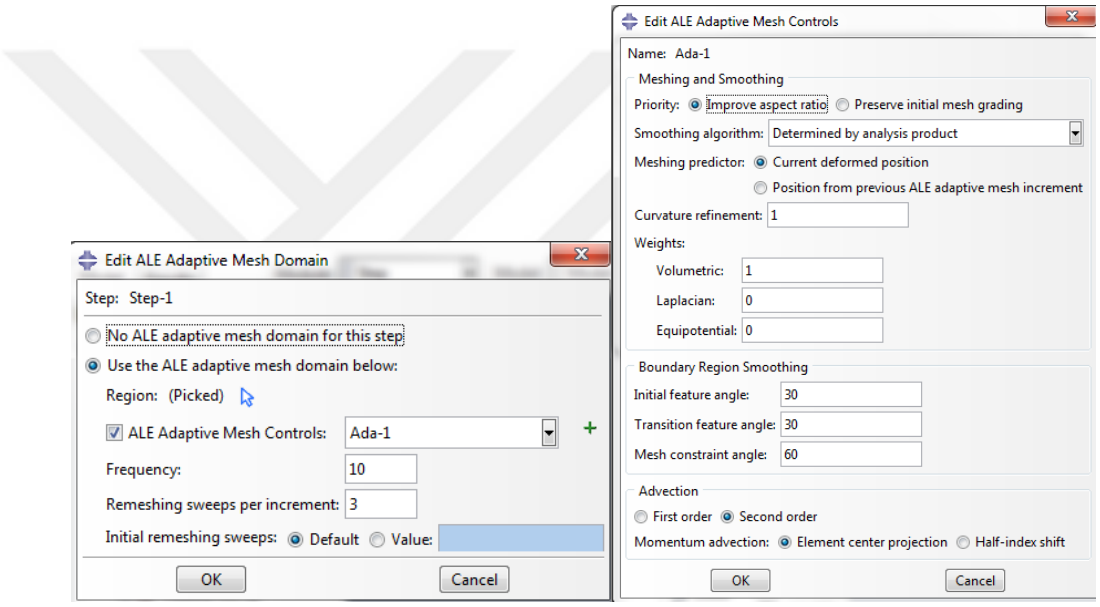


Figure 4.5 Adaptive mesh with adaptive mesh controls options in ABAQUS

In ABAQUS/explicit, an approximation to the stability limit can be used as the smallest time of a dilatational wave across any of element of the mesh [69].

$$\Delta t \approx \frac{L_{min}}{c_d} \qquad (\mathbf{4.4})$$

where L_{min} is the smallest element dimension in the mesh and c_d represents the dilatational wave speed in terms of $\lambda_o$and μ_o. In an isotropic, elastic material the effective Lamé's constants can be defined in terms of Young's modulus, *E*, and Poisson's ratio *v* by:

$$c_d = \sqrt{\frac{\lambda_o + 2\mu_o}{\rho}} \tag{4.5}$$

where ρ is the density of the material.

$$\lambda_o = \frac{Ev}{(1+v)(1-2v)} \tag{4.6}$$

$$\mu_o = \frac{E}{2(1+v)} \tag{4.7}$$

In most of cases, this estimate is not a conservation and it is just approximate. The actual stable time increment selected by ABAQUS/ Explicit is less than this estimate by a factor between $1/\sqrt{2}$ to 1 in a two-dimensional model and between $1/\sqrt{3}$ to 1 in a three-dimensional model. In this simulation, fully automatic stable time increment according to element by element was used to determine the stability limit. The stable time increment is equal 4.451×10^{-8} s (chosen by ABAQUS/ Explicit) while it was calculated 6.393×10^{-8} s as shown in Appendix H. The termination time is 1s.

4.2.3 Interaction and Boundary Conditions

In axisymmetric tube drawing with a fixed plug model, there are two surface contacts. First, the contact occurs between the inner surface of the nib die and the outer surface of the tube. Second, there is contact between the outer surface of the plug and the inner surface of the tube. The frictional constraints were defined in the interaction condition. In procedure of explicit/dynamic, surface-to-surface (explicit) was developed to create interaction. Finite sliding with the penalty contact method was selected for all contacts to resolve tangential behavior of mechanical contact. In this method, the compressive force is proportional to the penetration of the material, using the basic concept of the Coulomb friction model. Contact interaction property was selected to define normal behavior (hard contact) and tangential behavior with friction coefficients of 0.1, 0.125, and 0.15. Fig. 4.6 depicts three boundary conditions that were applied to move material between the nib die and the fixed plug. In the first, the initial boundary condition represents by the nib die and the fixed plug were fixed in directions (U1=0, U2=0) while the direction (UR3≠0). In the second initial boundary condition, initial velocity

was given on the head of the initial tube as 71 mm/s. In the third, the step that is moved the initial tube in the drawing direction, a velocity of 71 mm/s was used at the head of the tubes for all models, and the material was drawn in the drawing direction.

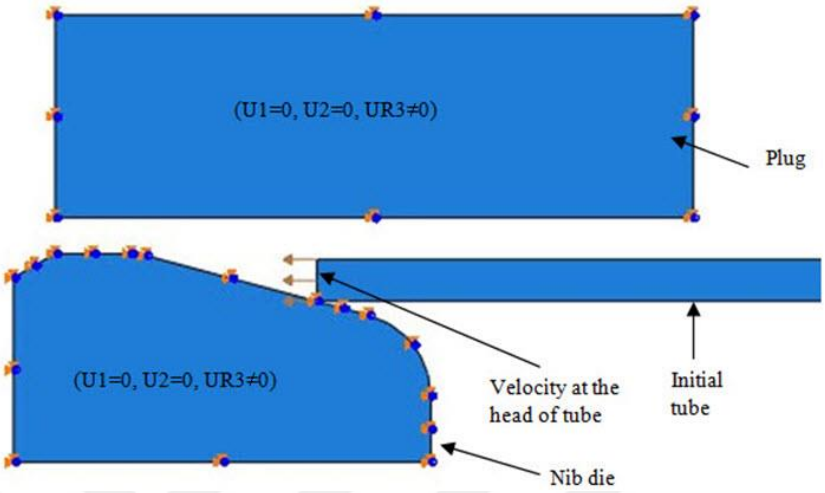


Figure 4.6 Boundary condition of the AFEM

4.2.4 Element and Mesh

A four node, bilinear axisymmetric element was selected. The initial tube was meshed with 1200 elements which represent the deformable part while the nib die with 362 elements and the fixed plug with 243 elements were meshed as shown in Fig. 4.7.

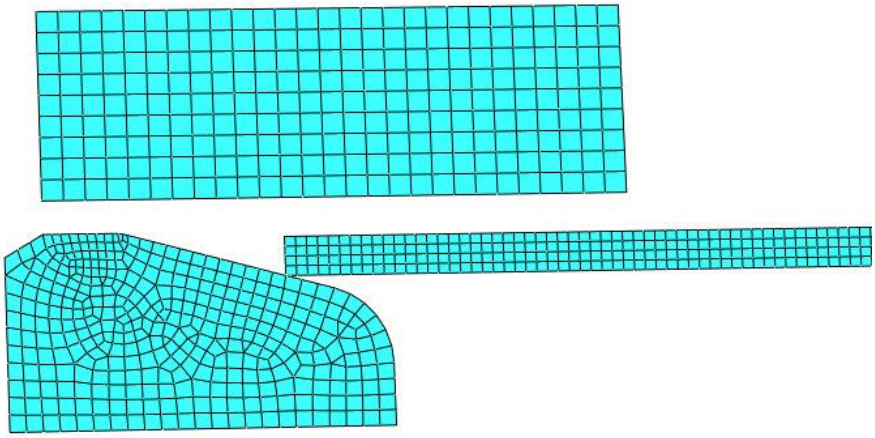


Figure 4.7 Finite elements meshing of the AFEM

Accuracy of the results depend on mesh size while a lot of the mesh elements leads to the increase in the analysis time. For this purpose, mesh sensitivity analysis of the thin walled tube was performed at fix time with specified critical location (fillet location for the tube) to find optimum mesh as pointed out in Fig. 4.8 and 4.9. The figures clearly indicate that the mesh converged and the element size was quite enough for simulation when the number of elements is 1200.

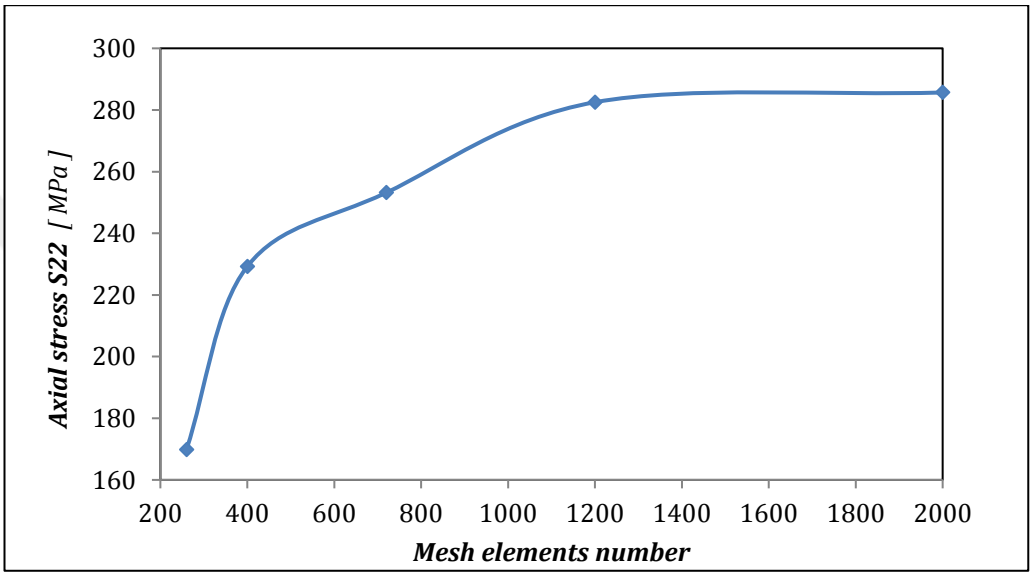


Figure 4.8 Mesh sensitivity analysis by the axial stress at 0.75s

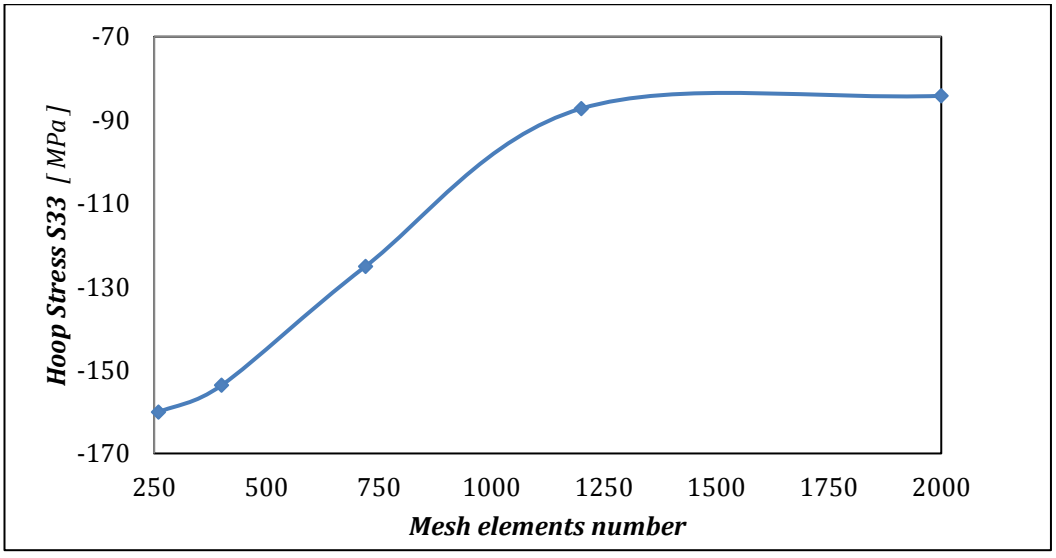


Figure 4.9 Mesh sensitivity analysis by the hoop stress at 0.75s

According to the ABAQUS/explicit for the analysis of the model with R=23%, the energy plots can be shown using history output option as presented in Fig. 4.10 and 4.11. More details for the models R=16% and 23% displaying the energy output are represented in Appendix I.

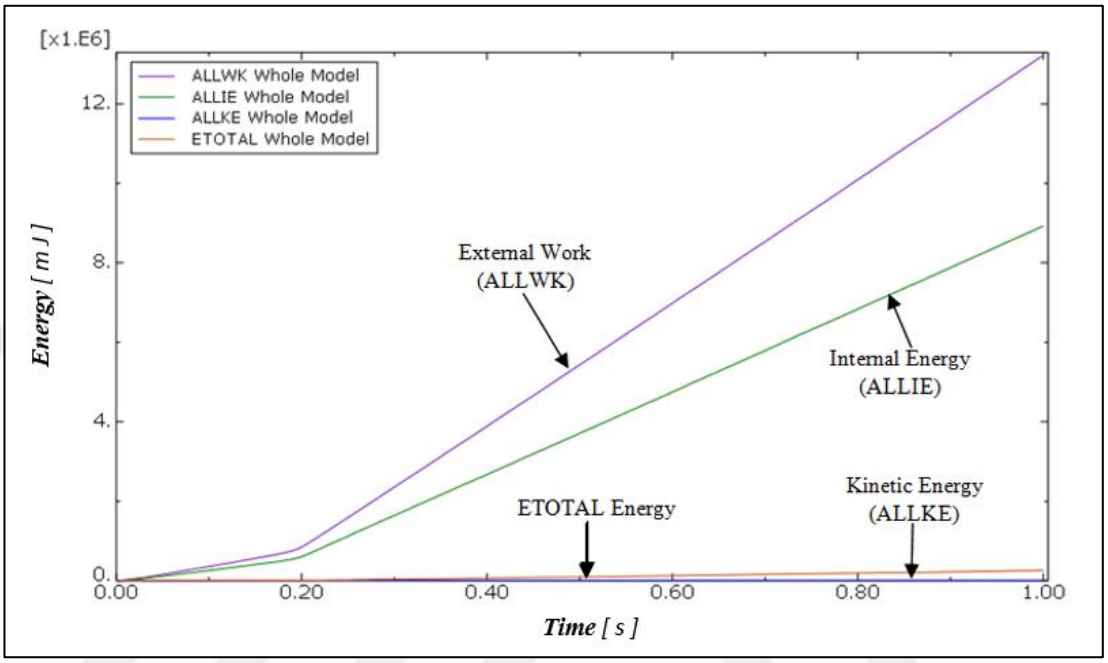


Figure 4.10 Energy output by ABAQUS for R=23%

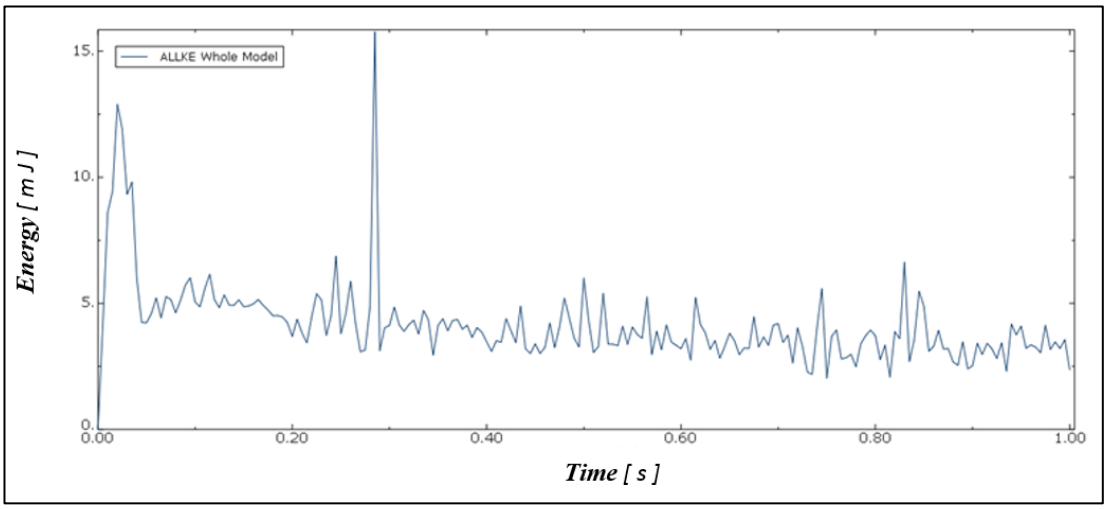


Figure 4.11 Kinetic energy by ABAQUS for R=23%

4.3 Three Dimension Tube Drawing with a Fixed Plug Model

The 3DFEM for the solid tube-drawing model was developed in order to compare with the AFEM model. The model was compared in only one case. The same geometry of the AFEM model with the semi die angle of 15°, semi plug angle of 0°, friction coefficient of 0.1, and reduction of area of 23% with the same dimensions were used for the 3DFEM. The material properties in Tables 4.2 and 4.3 were used. In the interaction step, interaction and boundary conditions were selected from the same AFEM. The mesh was applied as an 8-node linear brick element type. Fig. 4.12-14 display the three dimensional mesh for the nib die, the plug, and the initial tube, respectively.

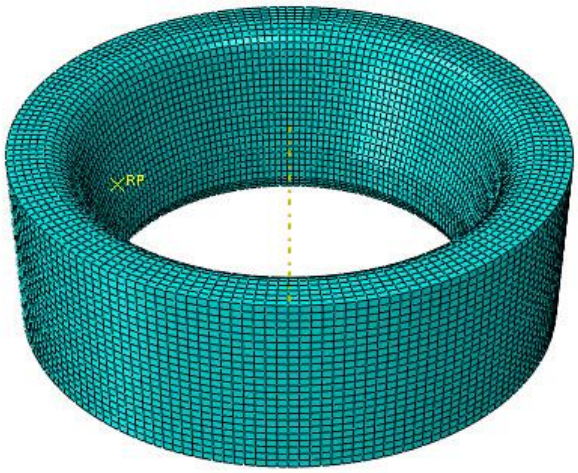


Figure 4.12 3DFEM meshing of the nib die at R=23%

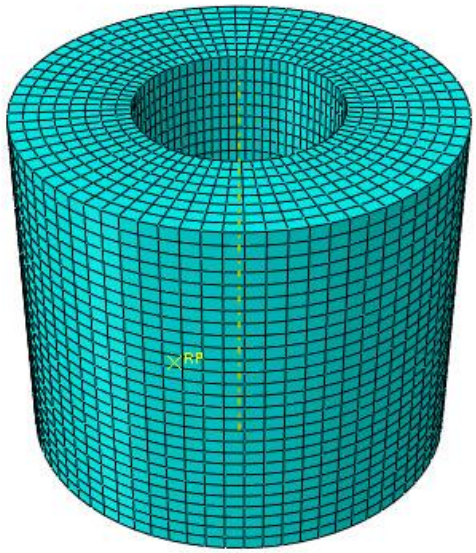


Figure 4.13 3DFEM meshing of the plug at R=23%

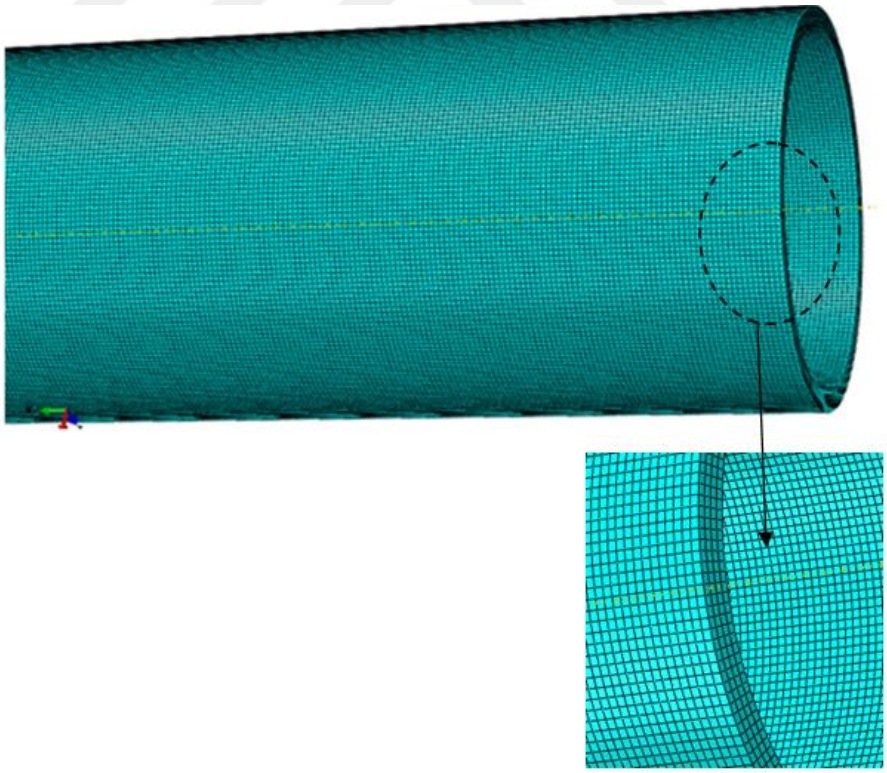


Figure 4.14 3DFEM meshing of the initial tube

CHAPTER 5

RESULTS AND DISCUSSION

5.1 Introduction

This chapter focuses on all the results and discussions that were experimentally and numerically obtained. Chemical compositions of the raw material (AISI 1010 steel tube) are shown. Mechanical properties of the initial tube and engineering stress vs. engineering strain, as well as true stress vs. effective plastic strain, are presented. Macro hardness results of the initial tube, the nib die, the plug, and the final tube, calibrated with R=16% and 23% are introduced. Compression force vs. displacement by the experimental method and the FEM at R=16% and 23% are given and discussed in detail as well as experimental and the FEM results are compared to each other. Drawing force vs. displacement plots for R=16% and 23% by FEM are shown. Residual stress results from the RLM inside the tube wall according to the axial and the hoop directions are displayed and explained extensively. SM results measuring hoop residual stress related to the depth of milled layers are introduced and put weight on. Hoop residual stresses below the tube surface and within the tube wall examined by XRD are presented and demonstrated. Results of axial and hoop residual stress estimations using the FEM are revealed. The comparison of results between the residual stresses that were measured by experimental and the numerical methods (RLM, SM, XRD, and FEM) are described. At the end, the results of the FEM by means of the different AFEM to identify optimum parameters for the tube drawing process with a fixed mandrel are depicted.

5.2 Chemical Composition Results

Table 5.1 introduces the results of chemical composition analysis for the raw material of AISI 1010 steel tube using the five samples that were checked using a spectrographic test. It can be seen that the average results for these samples were taken into consideration to determine the ratio of chemical composition for each element. These results are compared with the values given in Appendix G.

Table 5.1 Chemical composition of AISI 1010 steel tube

Ch.	S (1) Wt%	S (2) Wt%	S (3) Wt%	S (4) Wt%	S (5) Wt%	Avg. Wt%	A.S.D.	R.S.D.
C	0.124	0.109	0.112	0.117	0.115	0.116	0.0057	4.9
Si	0.175	0.181	0.182	0.162	0.168	0.174	0.0086	4.9
Mn	0.476	0.481	0.486	0.422	0.439	0.461	0.029	6.2
P	0.012	0.009	0.001	<0.001	0.021	0.009	-----	-----
S	0.006	0.004	<0.001	0.011	0.009	0.006	-----	-----
Cr	0.043	0.045	0.047	0.042	0.045	0.044	0.0019	4.4
Ni	0.037	0.038	0.037	0.037	0.038	0.037	0.00055	1.5
Mo	0.019	0.023	0.029	0.028	0.028	0.025	0.0043	16.8
Cu	0.023	0.024	0.023	0.024	0.024	0.024	0.00055	2.3
Ti	0.0022	0.0023	0.0019	0.0017	0.0018	0.0020	0.00026	13.2
Nb	<0.001	<0.001	0.002	0.002	0.004	0.002	-----	-----
Al	0.033	0.033	0.035	0.029	0.030	0.032	0.0024	7.6
V	<0.002	<0.002	<0.002	<0.002	<0.002	<0.002	-----	-----
Co	0.003	0.003	0.004	0.003	0.003	0.003	0.00045	13.6
W	0.020	0.025	0.029	0.026	0.025	0.025	0.0032	13.0
Pb	0.0007	0.0008	0.0012	<0.0005	<0.0005	0.0005	-----	-----
Sn	0.0037	0.0045	0.0040	0.0029	0.0042	0.0039	0.0006	15.8
B	<0.002	<0.002	<0.002	<0.002	<0.002	<0.002	-----	-----
Ca	0.0036	0.0028	0.0026	0.0024	0.0023	0.0028	0.0005	18.8
Ce	0.0025	0.0014	0.0067	0.0207	0.0093	0.0081	0.0077	95.0
La	0.0006	0.0006	0.0014	0.0043	0.0022	0.0018	0.0015	84.4
Bi	0.0012	0.0005	0.0012	<0.0005	<0.0005	0.0006	-----	-----
Sb	<0.001	<0.001	<0.001	<0.001	<0.001	<0.001	-----	------
As	0.002	<0.001	<0.001	<0.001	<0.001	<0.001	-----	------
Te	<0.0010	<0.0010	<0.0010	<0.0010	<0.0010	<0.0010	------	------
Ta	0.025	0.026	0.034	<0.001	0.009	0.019	------	-----
Se	<0.0030	<0.0030	<0.0030	<0.0030	<0.0030	<0.0030	------	-----
Zn	<0.001	<0.001	<0.001	<0.001	<0.001	<0.001	------	-----
Zr	<0.001	<0.001	<0.001	<0.001	<0.001	<0.001	------	-----
Fe	98.987	98.985	98.960	99.064	99.021	99.003	0.04	0.0

5.3 Tensile Test Results

The results of engineering stress vs. engineering strain plotting for the AISI 1010 steel tube were obtained as drawn in Fig. 5.1. Because the sample of the tensile test was sectioned from the initial tube sample, there is difficulty in the determine yield due to a high noise. The yield stress was estimated by the drawing 0.2% of strain and marked it on the strain (horizontal) axis. A line parallel to the stress vs. strain curve was drawn until it meets the curve at some point on the curve. Then the horizontal line from the meeting point was drawn until it meets the vertical stress axis. The yield stress was determined 560 MPa and ultimate stress 610.6014 MPa.

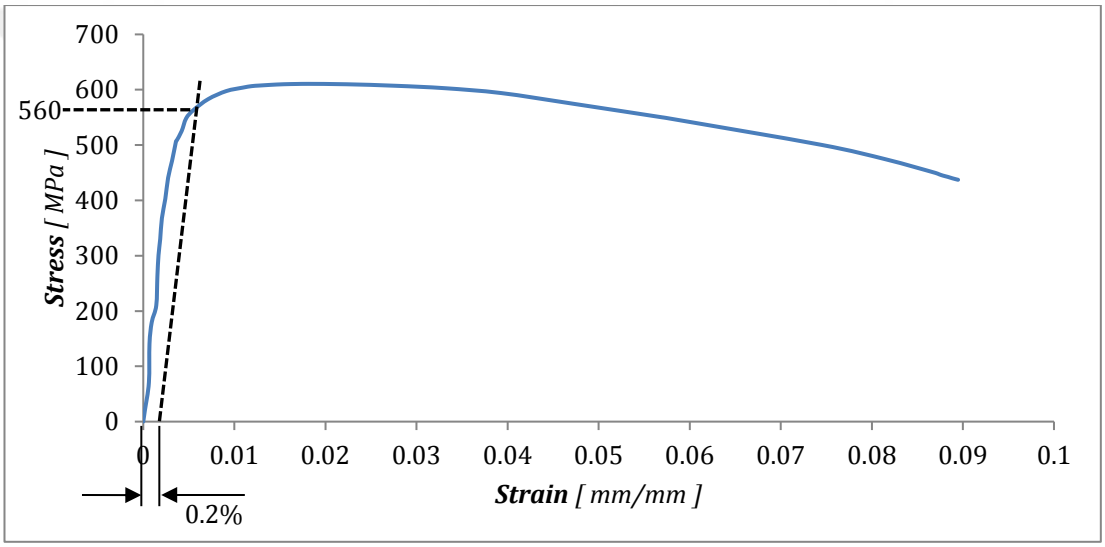


Figure 5.1 Eng. stress vs. eng. strain of AISI 1010 steel tube

From the engineering stress vs engineering strain, the true stress vs. true total strain and true stress vs effective plastic strain can be determined according to the Eq. 4.1, 4.2, and 4.3 that was presented in chapter four. The values of these curves were displayed in Appendix G. The magintudes of true stress vs. effective plastic strain are used in the simulations to define material properties. Fig. 5.2 describes the true stress vs. effective plastic strain plot.

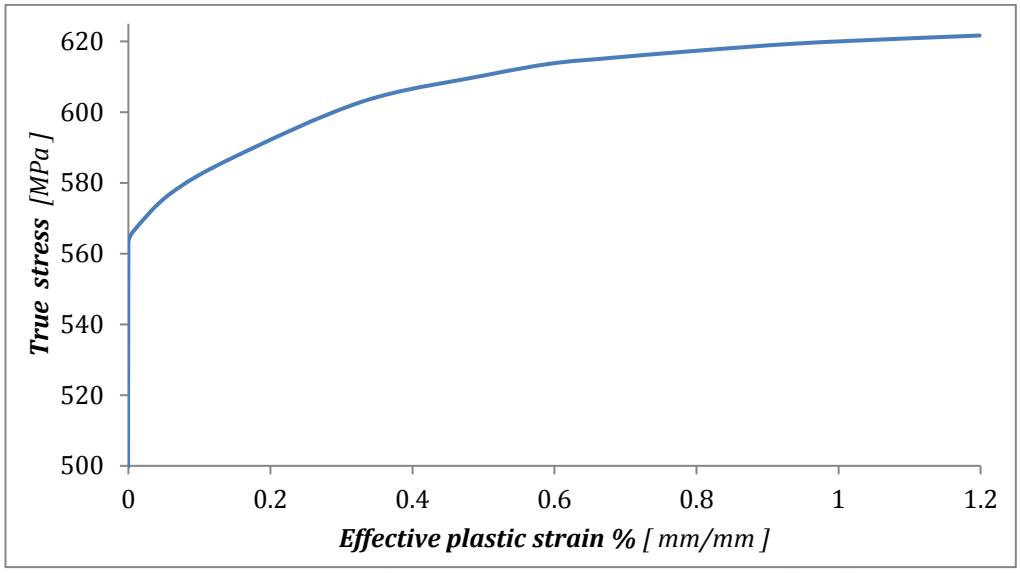


Figure 5.2 True stress vs. effective plastic strain plot of AISI 1010 steel tube

5.4 Macro Hardness Results

The results of the macro hardness tests for the nib die, the fixed plug, the initial tube, and the final tubes that were produced at R= 16 % and R=23% are displayed in Table 5.2. It is clear that the hardness of the final tube increases with increasing reduction of area due to the increase in strain hardening during the drawing process [70].

Table 5.2 Macro hardness results

Item	Test 1	Test 2	Test 3	average
Nib die and plug	71.10 HRC	71.53 HRC	71.53 HRC	71.386 HRC
Initial tube	131 HBW	133 HBW	133 HBW	132.333 HBW
Final tube produced with R=16%	184 HBW	186 HBW	187 HBW	185.67 HBW
Final tube produced with R=23%	208 HBW	203 HBW	206 HBW	205.67 HBW

5.5 Results of Compression and Drawing Force with Displacement

Results of force with displacement through the tube production with a fixed mandrel were experimentally and numerically determined using compression process with a constant semi die angle 15°, semi plug angle 0° at R=16% and 23%. The drawing force vs. displacement plots were numerically identified for R=16% and 23%.

5.5.1 Experimental and FEM Results of Force with Displacement by Compression Process

In this study, the compression test with low velocity was experimentally performed to measure force vs. displacement plots. FEM according to the AFEM using ABAQUS was also applied to simulate compression process for R=16% and 23% as shown in Fig. 5.3. In these simulations, the length of initial tube 70 mm and compression velocity 71 mm/s. Because the compression velocity for the experiments is very low (0.0286 mm/s for R=16% and 0.03 mm/s for R=23%), the effect of the velocity on the force during the forming process must be shown. In this study, the effect of velocity can be neglected. For more details, Appendix J displays the effect of the velocity on the force during the drawing process.

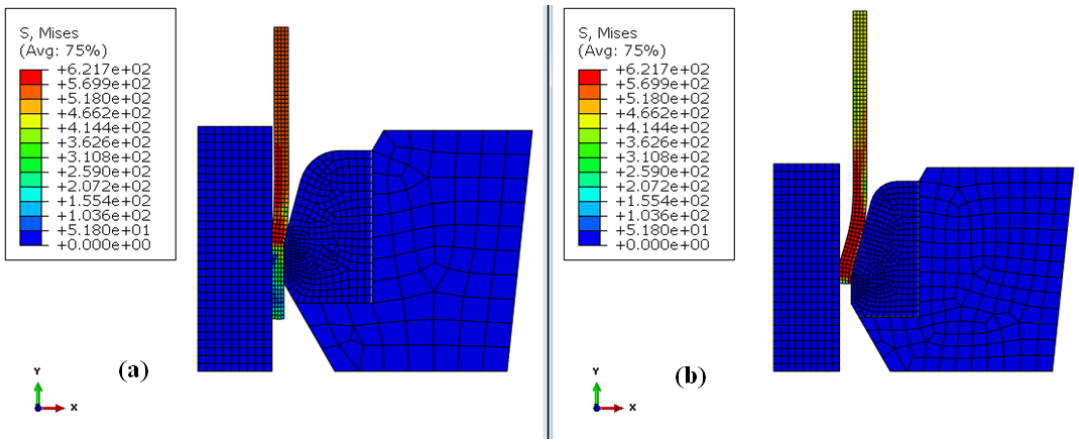


Figure 5.3 Von mises stress distribution by compression process (a) R=16% and (b) R=23%

The results of the experimental method and FEM were compared as pointed out in Fig. 5.4 and 5.5 at R=16% and 23%, respectively with a constant semi die angle of 15° semi plug angle of 0° and friction coefficient of 0.1. In Fig. 5.4, it is clearly seen that the experimental and the FEM results are reasonably close to each other. This good correlation indicates that the boundary conditions and initial conditions of the model are sufficiently accurate. Initially, the compression force was significant increased. After reaching the steady-state the force in the constant state with some increases and decreases in FEM results due to the explicit analysis that give some fluctuates. To decrease theses fluctuates filter output was applied. The external energy according to

the compression force and displacement of 20 mm for the experiment is 5.530 kJ while in FEM the external work is 5.907 kJ at displacement 20 mm. The calculation of external energy for experimental results and external energy plots are shown in Appendix K. From these results, it can be said that the model of compression process at R=16% was validated and the results are close to each other for both the experiment and FEM.

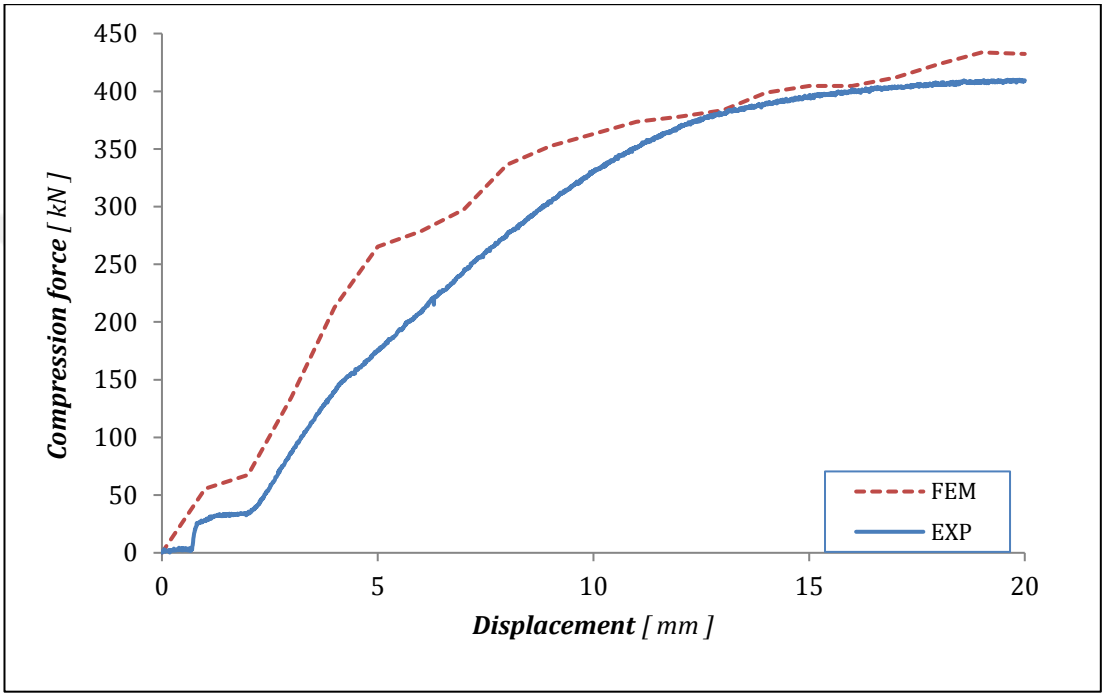


Figure 5.4 Comparison between the experiment and the FEA at R=16% for the compression process

In Fig. 5.5, the compression force is almost constant in the start of the process due to the space between the inner surface of the tube and outer surface of the plug. After the displacement of 12 mm, the compression force increases when the tube is fully in contact with the nib die and the fixed plug. In this test, the force was measured until the displacement reaches to 16.5 mm. After 16.5 mm, the tube will be subjected to the buckling due to the high reduction of area R=23%. Also, the energy according to the force and the displacement for the experiment was calculated 1.7209 kJ while in FEM the external work was determined 1.60019 kJ at a displacement of 16.5 mm as displayed in Appendix K. According to the results, there is a good agreement between experiment and FEM.

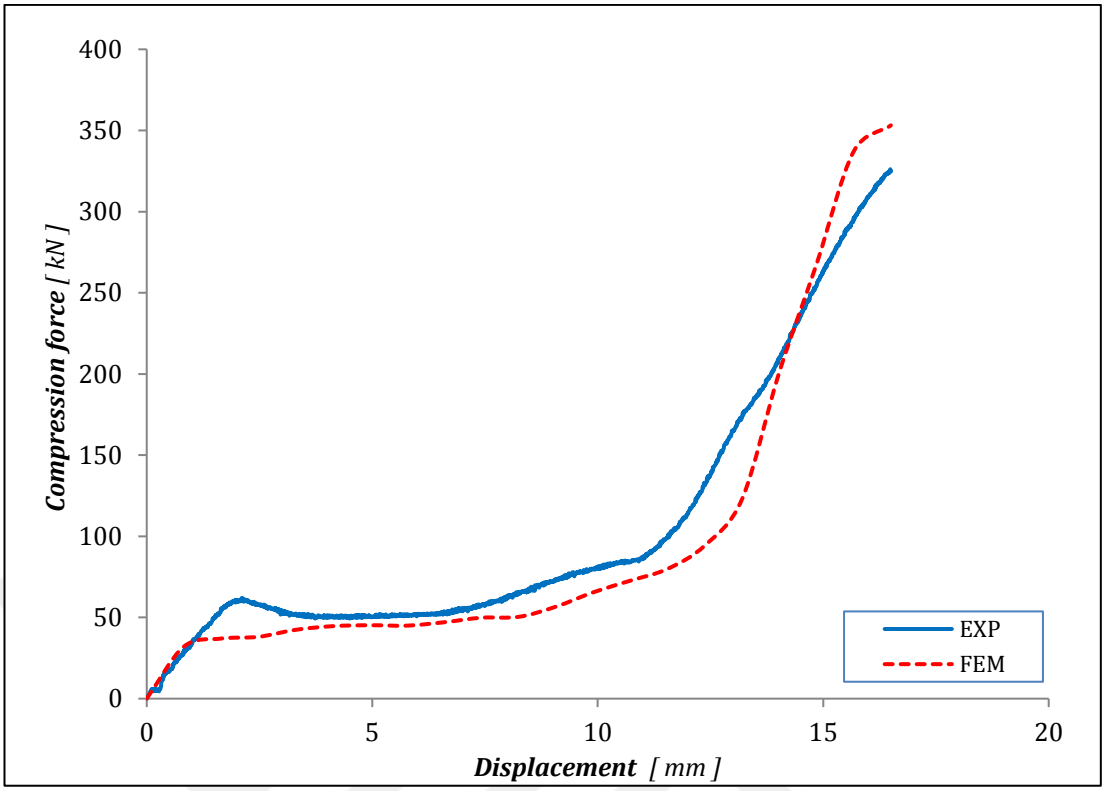


Figure 5.5 Comparison between the experiment and the FEA at R=23% for the compression process

Fig. 5.6 shows equivalent plastic strain for R=16 and 23% under compression load.

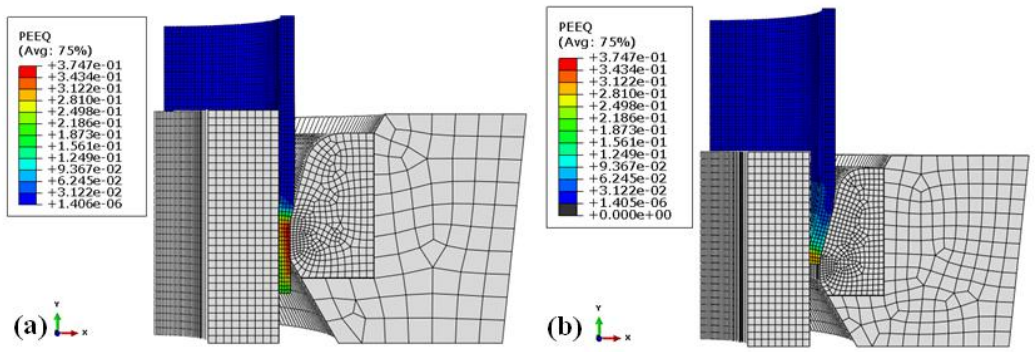


Figure 5.6 PEEQ contours by compression process (a) R= 16% and (b) R=23%

5.5.2 FEM Results of Force with Displacement by Drawing Process

The results of the FEM were recorded by simulating the AFEM. It is a great need to make a comparison between the results of the AFEM and the 3DFEM as shown in Fig. 5.7 and 5.8 that show the distribution contour of Max. and Min principal stress respectively. Because the 3DFEM needs a long time to complete the analysis, a velocity of 30 m/min was applied with a total time of 0.06s. These models were simulated with R=23%, semi die angle 15°, semi plug angle 0°, and friction coefficient of 0.1.

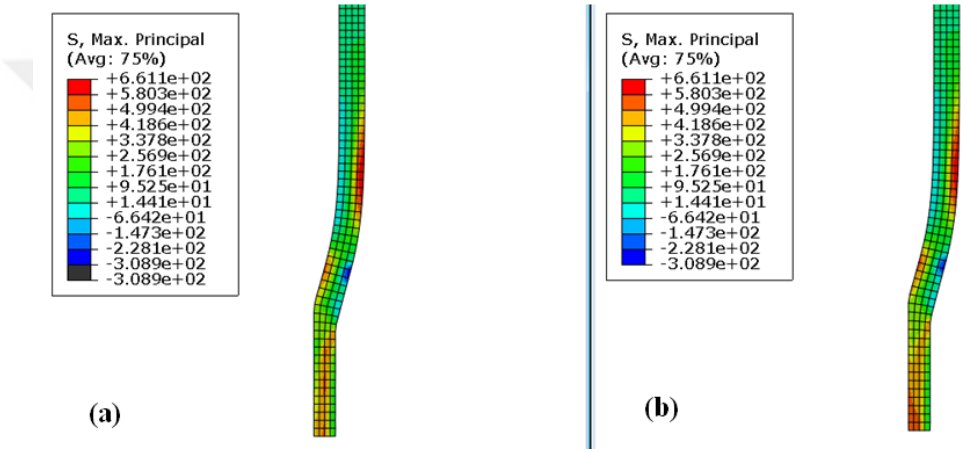


Figure 5.7 Max. principal stress distribution (a) AFEM and (b) 3DFEM

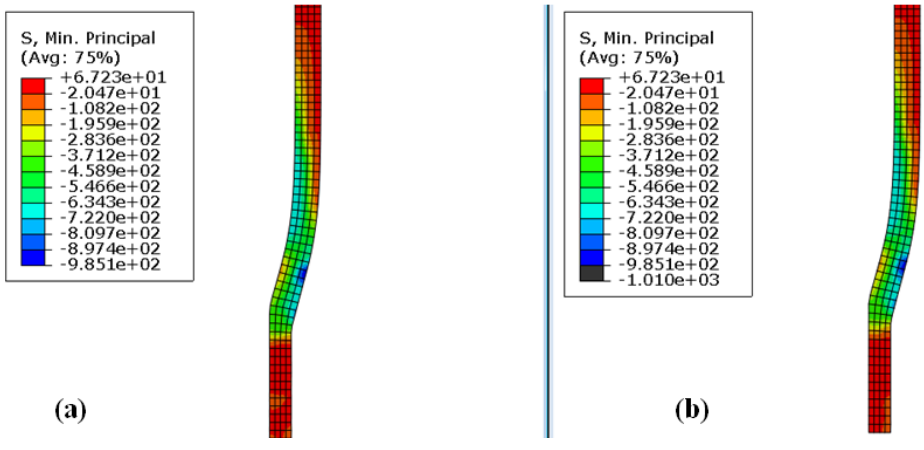


Figure 5.8 Min. principal stress distribution (a) AFEM and (b) 3DFEM

From Fig. 5.7 and 5.8, it is obvious that the distributions of Max. and Min. principal stresses are very close in the AFEM and the 3DFEM. AFEM can be used in tube drawing to reduce the computing time [5]. Since the number of elements is less, the most accurate mesh can be generated and convergence error will be reduced. Therefore, an accurate result will be obtained in AFEM.

Fig. 5.9 refers to the drawing force vs. displacement plots were determined by FEM at R = 16% and 23% when total displacement is 71 mm. At R=16%, the drawing force reached to 201.829 kN while at R=23%, the drawing force was determined 217.816 kN. It can be observed that the drawing pass with R=16% is small compared with R=23%. Therefore, the biggest reduction of area produces large drawing pass that leads to the increase in the size of forming zone then the drawing force will increase due to increase in plastic deformation [71]. Initially, the drawing force was significant increased. After reaching the steady state the force decreases and then almost constant. Eventually, the force needed for drawing was less than the maximum drawing force due to higher yield stress and strain hardening [72]. As expected, drawing force at R=23% was recorded as greater than R=16% due to the increase in overall plastic deformation. It is a well-known fact that hardening is increased with increasing plastic deformation.

From the Fig. 5.9, It can be seen that the behavior of drawing force is different between R=16% and 23% at the beginning of drawing process. For R=16%, the drawing force sharply increases due to the fully contact between the tube surfaces, the nib die and the fixed plug. For R=23%, the drawing force at the beginning of the process rapidly increases until 3.55 mm due to the first contact between the tube and the nib die then, the drawing force is almost constant until 10.65 mm. The drawing force again sharply increases due to the fully contact between the tube, the nib die, and the fixed plug.

The behavior of the drawing force and the displacement can be summed up in three stages. At the initial stage, the drawing force sharply raises (depend on the fully contact between the tube and the tool) because of the increase in plastic deformation. In the second stage, the force is almost constant as a result of a steady state forming that allows the force to be constant. In the final stage, the drawing force decreases when the tube exits the die.

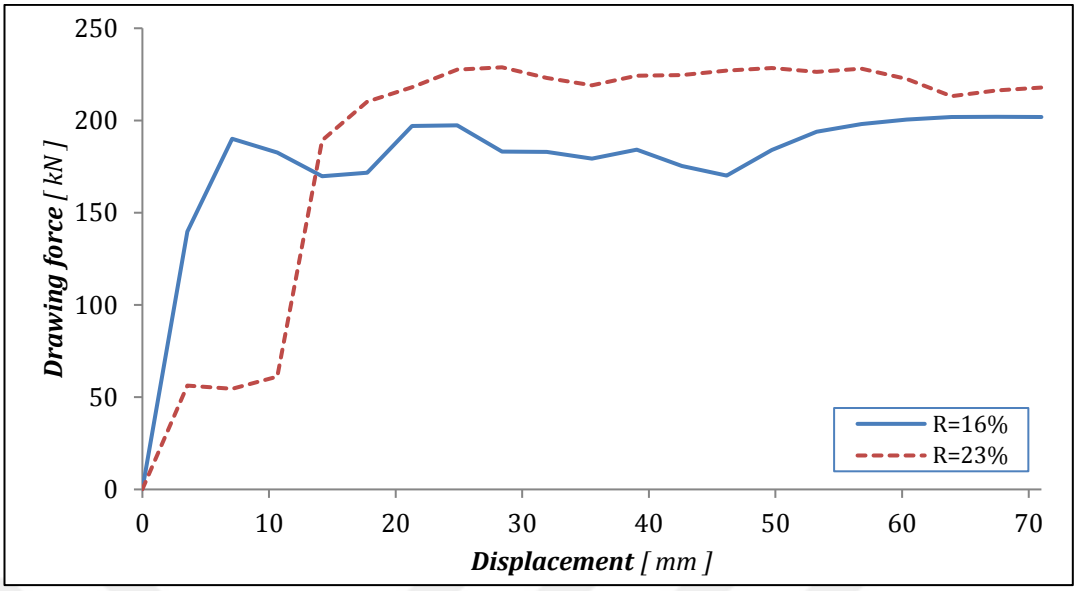


Figure 5.9 Plots of drawing force vs. displacement obtained numerically

Equivalent plastic strain (PEEQ) contours were plotted by ABAQUS as presented in Fig. 5.10. It can be seen that the plastic strain at R=23% is greater than R=16%. This leads to an increase in the drawing force. It is obvious that there is a clear difference in plastic deformation for (a) and (b) due to the change in reduction of area. The plastic deformation occurs as dislocation motions that result in a linear defect in the crystal lattice.

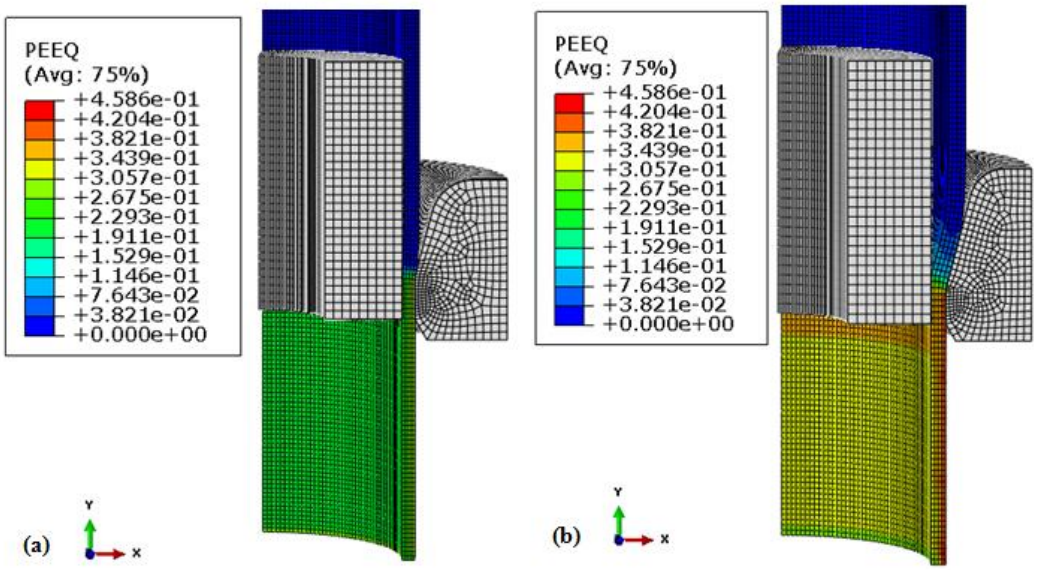


Figure 5.10 PEEQ contours by drawing process (a) R= 16% and (b) R=23%

5.6 Residual Stress Results within the Tube Wall

Residual stresses within the final tube wall that was formed with R=16% and 23% were measured. Various experimental methods were utilized to determine the average magnitude and state of residual stress along the tube wall. The results of the numerical method with the same reduction of areas were also obtained.

5.6.1 Results of Residual Stress by the RLM

The RLM using a milling process that represents the main contribution of this study was applied to determine longitudinal and circumferential residual stresses inside the tube walls. A milling process that is a destructive method was selected as the best and most suitable method for material removal in specimens of tubular shape. The removal of layers of the specimen material was also continuous rather than stepwise so that specimen deformation could be recorded continuously. The resolution of the residual stresses was measured, and hence the stress gradients are dictated by the number of increments made in the removal of material.

The relationship between microstrain and time is shown by the output of the results obtained by the TRSG. For the RLM, different samples were used to measure the axial and hoop residual stresses. For each sample, different measurements of residual strain inside the tube wall were performed and the average value of each measurement was calculated where after the average value for these samples at the thickness of each milled layer was determined. Finally, residual stress was estimated from the Young Modulus and measured strain.

For the tubes that were calibrated with R=16%, Tables 5.3-5.6 introduce the average of axial and hoop microstrain measurements that were obtained by three samples using the RLM. For each table, results of three samples are presented. Table 5.3 and 5.5 shows results of axial and hoop residual microstrain, respectively. External milling started from the outer surface of the tube until the wall thickness is reduced to 1.5 mm. In Table 5.4 and 5.6, results of axial and hoop microstrain are respectively revealed when the milling of layers begins from the inner surface of the tube until the wall

thickness is reduced to 1.5 mm. In the last column of these tables, the total average value for three samples is displayed.

Table 5.3 Results of average axial microstrain by the RLM from the outer to the inner surface for R=16%

Distance from the outer surface (mm)	Sample1 (average microstrain)	Sample2 (average microstrain)	Sample3 (average microstrain)	Total average microstrain
0.25	188.1239	207.545	160.7691	185.4793
0.5	143.7426	145.7529	151.6747	147.0567
0.75	119.9005	131.4227	131.4993	127.6075
1	105.7012	95.60871	92.68215	97.99735
1.25	65.72884	66.38496	72.9545	68.3561
1.5	26.79949	32.2369	30.87608	29.97082

Table 5.4 Results of average axial microstrain by the RLM from the inner to the outer surface for R=16%

Distance from the inner surface (mm)	Sample1 (average microstrain)	Sample2 (average microstrain)	Sample3 (average microstrain)	Total average microstrain
0.25	-548.235	-553.672	-501.235	-534.381
0.5	-420	-395.39	-367.015	-394.135
0.75	-252.987	-270.571	-260.962	-261.507
1	-210.864	-185.283	-205.866	-200.671
1.25	-91.8563	-80.192	-105.636	-92.5614
1.5	31.2623	34.7247	24.0481	30.0117

Table 5.5 Results of average hoop microstrain by the RLM from the outer to the inner surface for R=16%

Distance from the outer surface (mm)	Sample1 (average microstrain)	Sample2 (average microstrain)	Sample3 (average microstrain)	Total average microstrain
0.25	195.7906	196.595	158.8058	183.7305
0.5	158.9202	152.0002	158.7892	156.5699
0.75	104.6393	123.8778	109.6284	112.7152
1	73.0627	70.6437	61.89435	68.53358
1.25	30.44831	30.6069	41.40933	34.15485
1.5	-9.94209	-11.4356	-12.9253	-11.4343

Table 5.6 Results of average hoop microstrain by the RLM from the inner to the outer surface for R=16%

Distance from inner surface (mm)	Sample1 (average microstrain)	Sample2 (average microstrain)	Sample3 (average microstrain)	Total average microstrain
0.25	-166.094	-164.264	-149.586	-159.981
0.5	-137.551	-143.949	-135.41	-138.97
0.75	-121.376	-131.008	-127.482	-126.622
1	-71.7693	-61.3068	-88.4579	-73.8447
1.25	-55.2697	-49.6847	-60.7938	-55.2494
1.5	-13.4333	-10.115	-6.72	-10.0894

For the tubes that were formed with R=23%, Tables 5.7-5.10 indicate the average of axial microstrain that was measured by different samples by means of the RLM. For each table, results of three samples were reported. Table 5.7 and 5.9 refer to the measuring results of axial and hoop residual microstrain respectively by external milling that started from the outer surface of the tube until the wall thickness is reduced to 1.5 mm. In Table 5.8 and 5.10, results of axial and hoop microstrain are respectively pointed out at the milling of layers beginning from the inner surface of the tube until

the wall thickness is reduced to 1.5 mm. The total average value for three samples was put in the last column of the tables.

Table 5.7 Results of average axial microstrain by the RLM from the outer to the inner surface for R=23%

Distance from the outer surface (mm)	Sample1 (average microstrain)	Sample2 (average microstrain)	Sample3 (average microstrain)	Total average microstrain
0.25	-676.06	-706.428	-645.966	-676.151
0.5	-593.371	-652.584	-668.11	-638.022
0.75	-479.75	-426.73	-472.526	-459.669
1	-251.141	-237.894	-248.662	-245.899
1.25	-58.0229	-66.0482	-74.4509	-66.174
1.5	116.784	122.017	120.0596	119.6202

Table 5.8 Results of average axial microstrain by the RLM from the inner to the outer surface for R=23%

Distance from the inner surface (mm)	Sample1 (average microstrain)	Sample2 (average microstrain)	Sample3 (average microstrain)	Total average microstrain
0.25	-53.5511	-23.7921	-10.007	-29.1167
0.5	-12.0847	-10.978	-7.28913	-10.1173
0.75	1.615268	-5.547	13.6854	3.251223
1	18.56912	5.899673	2.885904	9.118232
1.25	77.45049	86.65361	108.5149	90.873
1.5	115.635	89.06526	141.0027	115.2343

Table 5.9 Results of average hoop microstrain by the RLM from the outer to the inner surface for R=23%

Distance from the outer surface (mm)	Sample1 (average microstrain)	Sample2 (average microstrain)	Sample3 (average microstrain)	Total average microstrain
0.25	-31.6447	-45.5367	-38.4022	-38.5279
0.5	-9.04819	-13.5652	-18.0706	-13.5613
0.75	-12.3429	-5.00498	-5.17362	-7.50717
1	0.830092	8.32603	6.739895	5.298672
1.25	11.14115	6.187739	6.352804	7.893898
1.5	36.54698	33.77592	30.07207	33.46499

Table 5.10 Results of average hoop microstrain by the RLM from the inner to the outer surface for R=23%

Distance from the inner surface (mm)	Sample1 (average microstrain)	Sample2 (average microstrain)	Sample3 (average microstrain)	Total average microstrain
0.25	33.7731	47.23158	50.39611	43.80026
0.5	18.46368	26.00798	24.92263	23.13143
0.75	6.721082	3.460023	1.023327	3.734811
1	-27.0221	-6.03	-20.8378	-17.9633
1.25	-27.2718	-11.4245	-20.1245	-19.6069
1.5	-24.4809	-24.2634	-13.5041	-20.7495

The results show that the measurement of microstrains both of the axial and the hoop directions at near the outer and the inner surfaces are high compared with core the tube wall due to the change in tube dimensions after the drawing process by the nib die and the fixed plug. While in middle the tube wall, there are a little impact for tool geometry. This phenomenon agreed with bar section that presented by Rocha [73].

From the tables that show average microstrain, axial, and hoop residual stress measurements within the wall along the area that milled can be plotted. These measurements start from a distance of 0.25 mm to 2.75 mm (from the outer to the inner surfaces). Fig. 5.11 depicts the relationship between residual stress measurement within the tube wall by means of the RLM at R=16%. It can be seen that both axial and hoop residual stresses in tension state near the outer surface of the tube while they are in compression state near the inner surface of the tube. Axial residual stresses greater than hoop residual stresses were recorded especially near the inner surface of the tube due to the high impact of the fixed plug in the axial direction.

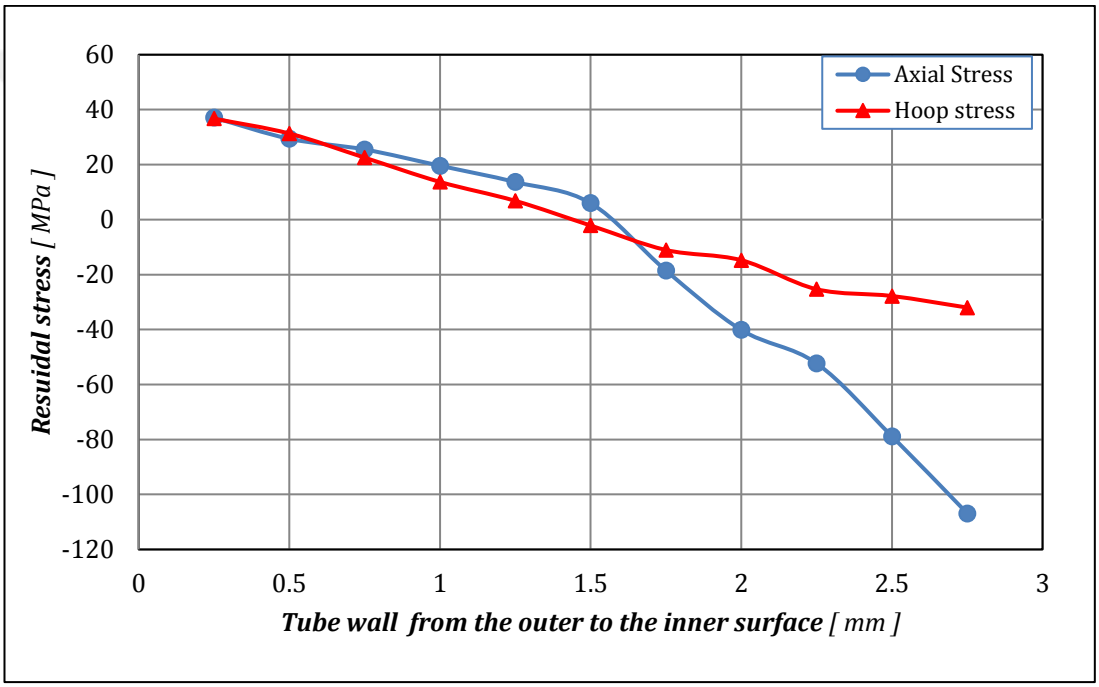


Figure 5.11 Residual stress measurement of final tube by the RLM at R=16%

The relationship between residual stress measurements and distance from the outer to the inner surfaces of the final tube that was calibrated with R=23% is described in Fig. 5.12. The results of axial and hoop residual stress indicate a compression state near the outer surface of the tube. Moreover, the axial residual stress near the outer surface was found to be larger than the hoop residual stress due to the high impact of the nib die in the axial direction. At the middle of the wall (1.5 mm), the state of the axial and the hoop residual stresses became in tension then returned to the compression state near the inner surface.

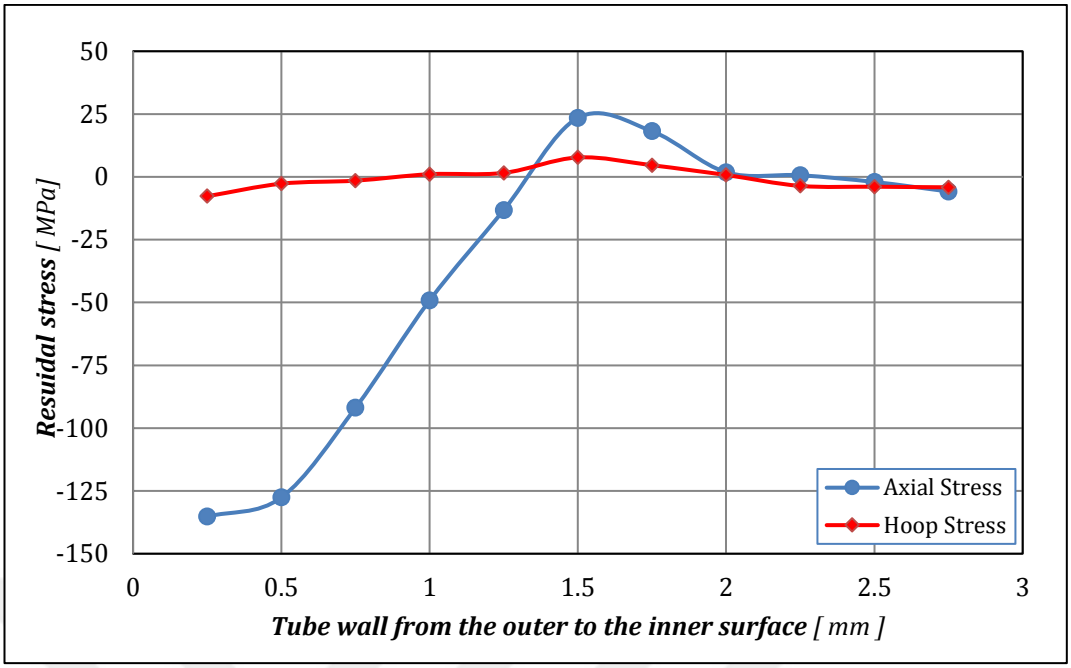


Figure 5.12 Residual stress measurement of final tube by the RLM at R=23%

5.6.2 Results of Residual Stress by the SM

Tube products which are calibrated at R=16% and 23% were also examined by the SM to measure the hoop residual stress inside the tube wall. The SM was applied through a milling process to make a slot of 4 mm width on the upper surface of the tubes while measuring the investigated hoop strains on the bottom surface.

Table 5.11 reports the results of average microstrain measurements by hoop direction for three samples according to the distance from the outer to the inner surfaces of the tube that was formed at R=16%. For these three samples, the total average for each measurement was calculated as displayed in the last column of the table.

Table 5.11 Results of average hoop microstrain by the SM for R=16%

Distance from the outer surface (mm)	Sample1 (average microstrain)	Sample2 (average microstrain)	Sample3 (average microstrain)	Total average microstrain
0.3	280.264	230.226	241.0625	250.5175
0.6	197.0864	197.8361	177.95	190.9575
0.9	117.2759	114.778	98.51758	110.1905
1.2	91.57826	81.92552	79.35079	84.28486
1.5	-25.5247	-19.9292	-23.282	-22.912
1.8	-106.619	-100.799	-88.6211	-98.6797
2.1	-132.792	-119.442	-135.316	-129.183
2.4	-206.629	-211.157	-175.772	-197.853
2.7	-267.231	-267.811	-248.048	-261.03

For the other three samples that were formed with R=23%, table 5.12 introduces the average microstrain measurements by the hoop direction using the SM related to the distance from the outer to the inner surfaces. Total average for three samples was also determined as pointed out in the last column of the table.

Table 5.12 Results of the average hoop microstrain by the SM for R=23%

Distance from the outer surface (mm)	Sample1 average microstrain	Sample2 average microstrain	Sample3 average microstrain	Total average microstrain
0.3	-22.9304	-22.1905	-30.1934	-25.1048
0.6	-9.51883	-5.23767	-14.2791	-9.67853
0.9	4.884193	14.57804	2.254453	7.238895
1.2	17.41276	9.488114	54.40825	27.10304
1.5	55.46525	48.79713	64.48923	56.25054
1.8	55.79665	35.15281	59.5954	50.18162
2.1	-1.51516	6.06177	2.293947	2.280186
2.4	-17.1419	-2.06372	-5.57222	-8.25928
2.7	-52.8974	-36.3954	-40.7759	-43.3562

According to Tables 5.11 and 5.12, the relationship between the hoop residual stress measurements and distance from the outer to the inner surfaces of the final tube by the SM were identified at R=16% and at R=23% as drawn in Fig. 5.13. It can be observed that the hoop residual stress in high level near the outer and the inner surfaces was recorded when R=16% while the behavior of hoop residual stress is completely different when R=23%. It can be said that the high and low reduction of area produced different behavior of residual stresses [74]. It is clear that the state of the hoop residual stresses of the final tube that was produced at R=16% are in tension near the outer surface and in compression near the inner surface. The state of residual stresses of the final tube that was formed at R=23% are in compression level near both the outer and inner surfaces while in tension around the core of tube thickness.

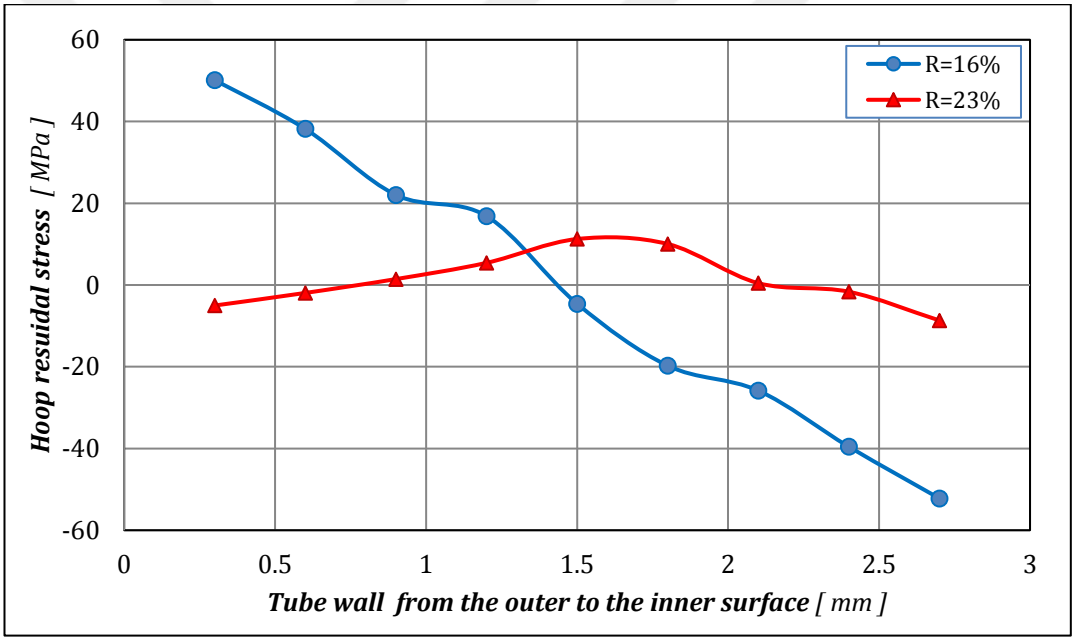


Figure 5.13 Hoop residual stress measurement of final tube by the SM

5.6.3 Results of Residual Stress by the XRD

Hoop residual stress measurements were also made by the XRD in the five orientations. Fig. 5.14 indicates a XRD residual stress measurement of -50.57 MPa with a reliability of $\pm$16.19 MPa at R=16% when the measurement was done just below the inner surface of the tube.

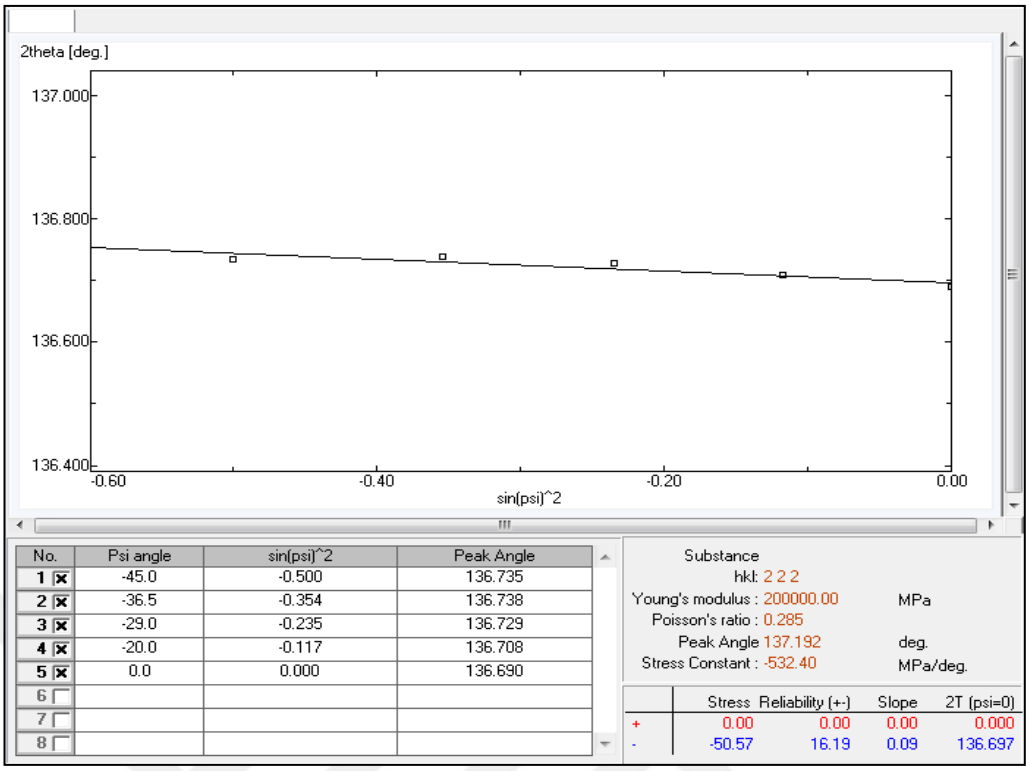


Figure 5.14 Hoop residual stress measurements by the XRD below of the inner surface of the tube at R=16%

In Fig. 5.15, the XRD reveals residual stress of -29.89 MPa with a reliability of $\pm$11.34 MPa at R=23% when the measurement was done just below the inner surface of the tube. In both of Fig. 5.13 and 5.14, the values of residual stress accroding to the relationship between peak location ($2\theta°$) and different orientations ($\Psi°$) were recorded. This means that the magnitude of residual strain related to average values that were obtained in five orientations and residual stress according to Young's modulus and Poisson's ratio was determined.

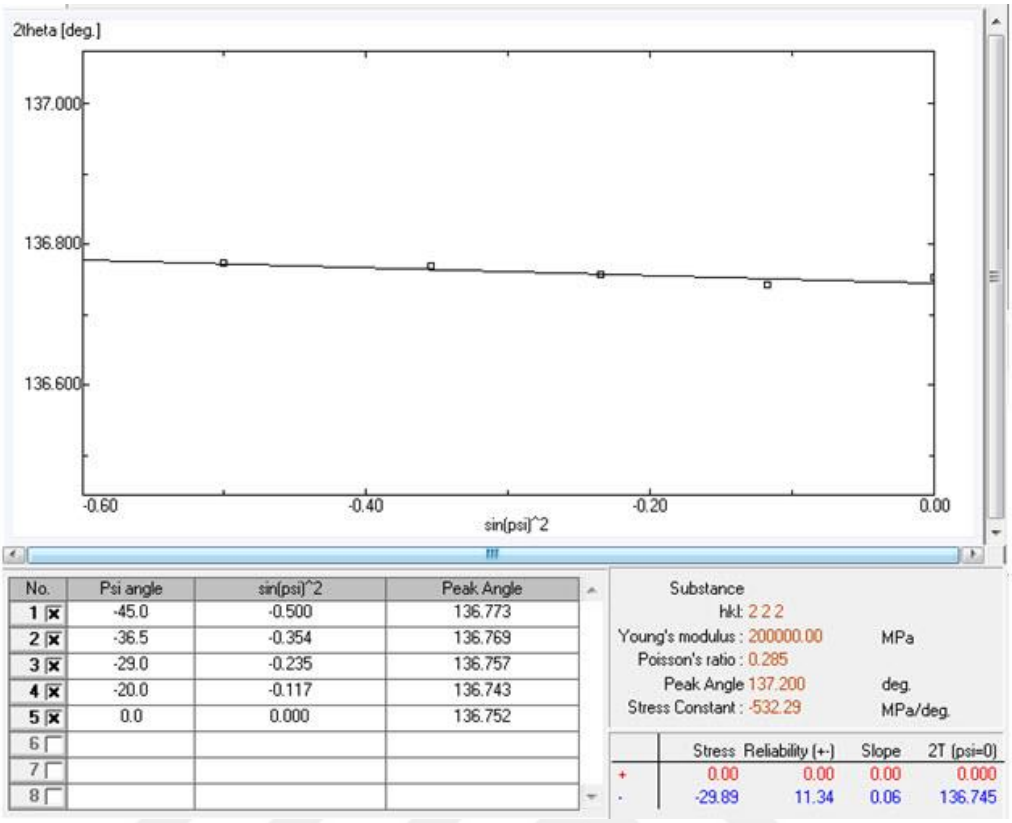


Figure 5.15 Hoop residual stress measurements by the XRD below of the inner surface of the tube at R=23%

Fig. 5.16 shows the average results of residual stress measurement below the tube surface obtained in five orientations by the XRD for both R=16 % at position (150 mm form tube edge) and R=23% at position (90 mm form tube edge). In general, the increase in the reduction of area leads to the increase in the drawing force because of the increase in the relative energy consumption from the plastic deformation in the forming zone. The residual stresses strongly depend on the shape of the deformation zone that is mainly based on the reduction of area due to the change in the tube dimensions.

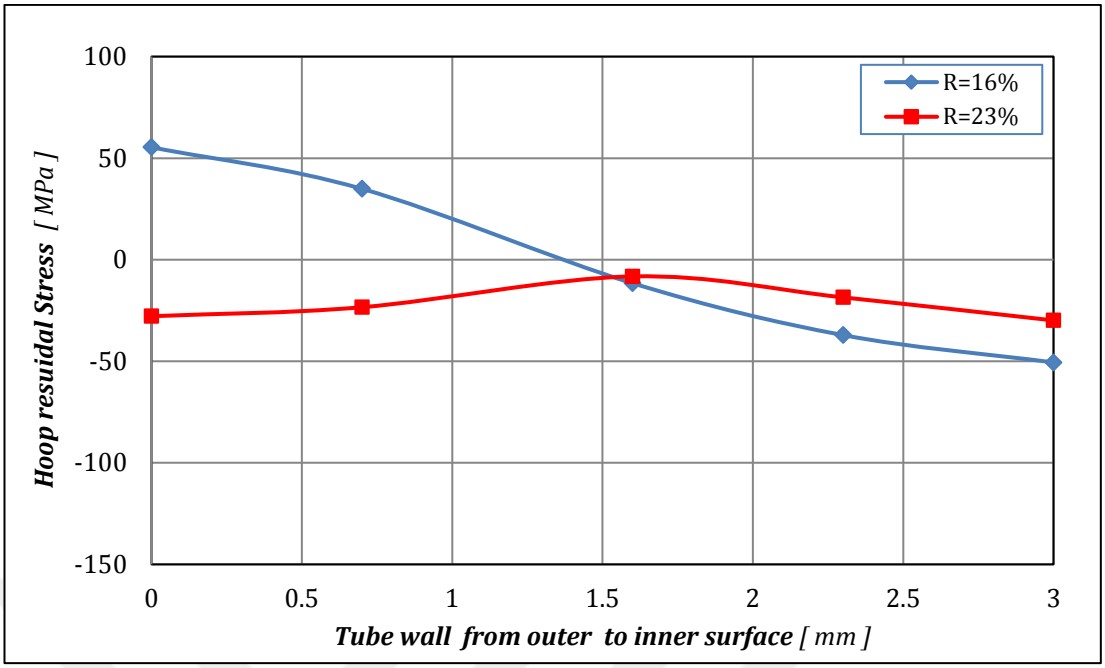


Figure 5.16 Residual stress measurements of final tube by the XRD

5.6.4 Results of Residual Stress by the FEM

The FEM was investigated by means of the AFEM models to determine axial and hoop residual stress within the tube wall as well as residual stresses in different orientations. Fig. 5.17 and 5.18 present distribution of axial and hoop stress respectively in a tube drawing process at R=16 %.

As shown in Fig. 5.17 and 5.18 at R=16%, the internal stresses begin to appear when the outer surface of the tube contacts with the nib die. By increasing drawing force, the internal stresses are generated in the tube near the nib die at the outer surface that is positive (tension), and negative (compression) near the inner surface, as the tube wall is bent downward [56]. When the inner surface of the tube contacts the outer surface of the fixed plug, the state of internal stresses change as the tube wall is bent upward due to the effect of the plug. Internal stresses become negative near the outer surface and positive near the inner surface. Full contact occurs between the tube with the nib die and the plug in the forming region. The tube wall was bent in an inverse way then the stress is positive near the outer surface and negative near the inner surface

for the final tube because the plug does not exit and tension generated by drawing force is small at the die exit.

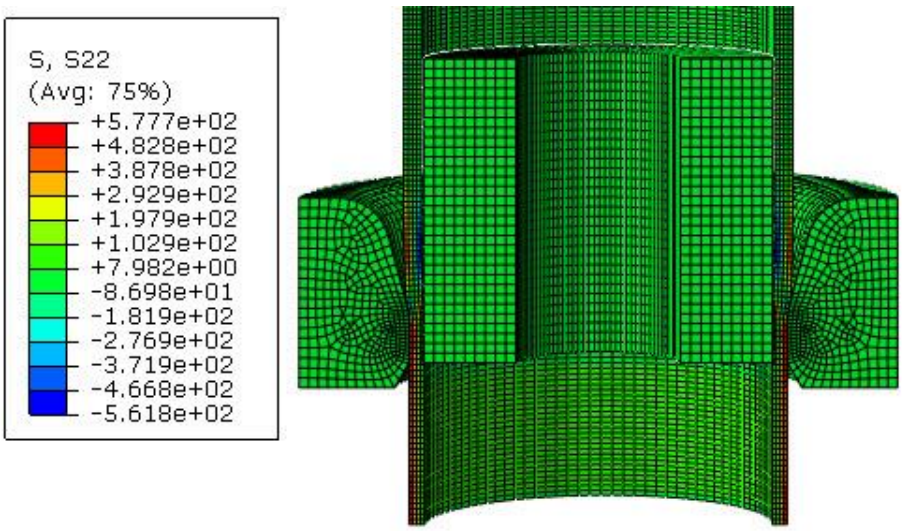


Figure 5.17 Distribution of the axial stress during the drawing process at R=16% by the FEM

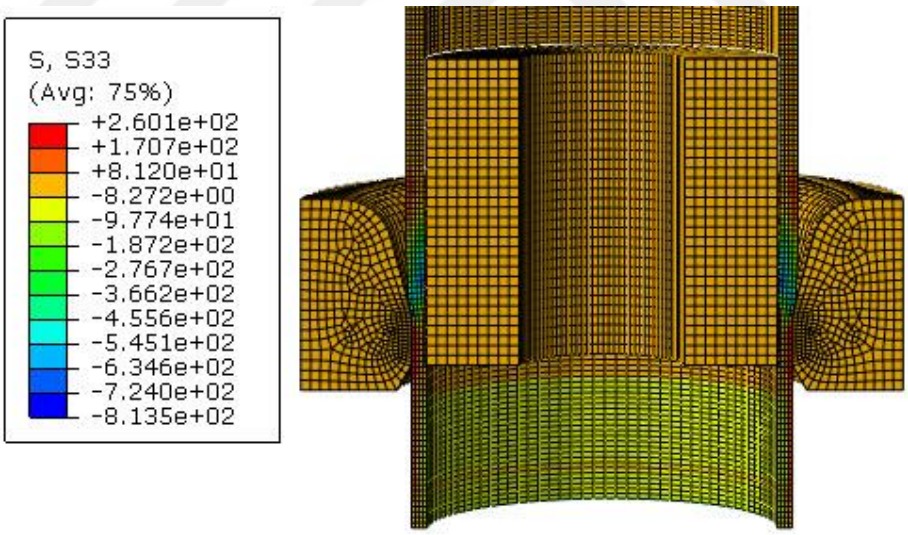


Figure 5.18 Distribution of the hoop stress during the drawing process at R=16% by the FEM

Fig. 5.19 and 5.20 describe the distribution of axial and hoop stress respectively during the tube drawing process by the AFEM at R=23 % by the FEM.

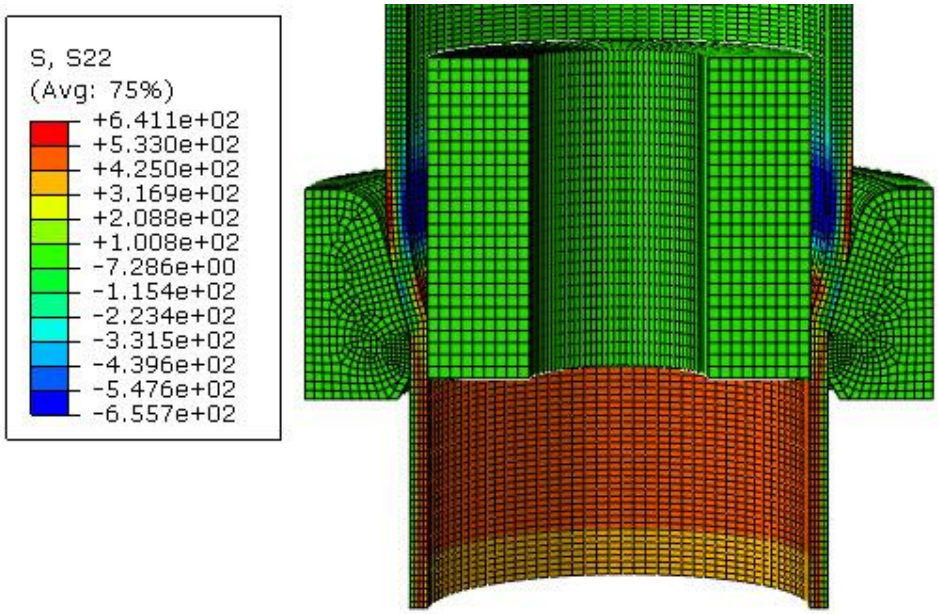


Figure 5.19 Distribution of the axial stress during the drawing process at R=23% by the FEM

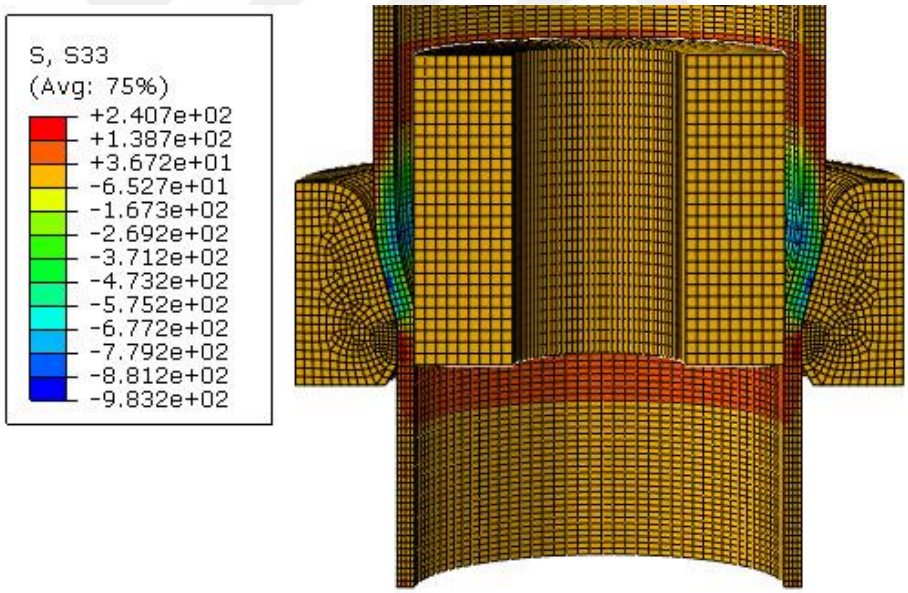


Figure 5.20 Distribution of the hoop stress during the drawing process at R=23% by the FEM

From Fig 5.19 and 5.20 at R=23%, the internal stresses also start to appear when the tube contacts with the nib die. Due to the effect of the drawing force, internal stresses that are induced in the contact area near the nib die at the outer surface are negative. The amount of reduction the inner diameter at R=23% is larger than R=16% so the

amount of drawing force at R=23% is larger than R=16% as mentioned previously, therefore the distribution of internal stresses were changed. It can be seen that the residual stresses near the outer surface of the tube are in a compression state since a large tension is forced upon the front portion of the tube at the nib die exit due to the fixed plug. This phenomenon agreed with the tension in the solid bar by Akiyama and Kouboki [75].

The average axial and hoop residual stress along the tube 142.89 mm for R= 16% and 155.67 mm for R= 23%. The residual stress within the tube wall was determined after the final tube had been fully produced. Fig. 5.21 introduces the axial and hoop residual stress inside final tube wall at R=16% while Fig. 5.22 indicates the axial and the hoop residual stresses in the final tube wall at R=23%.

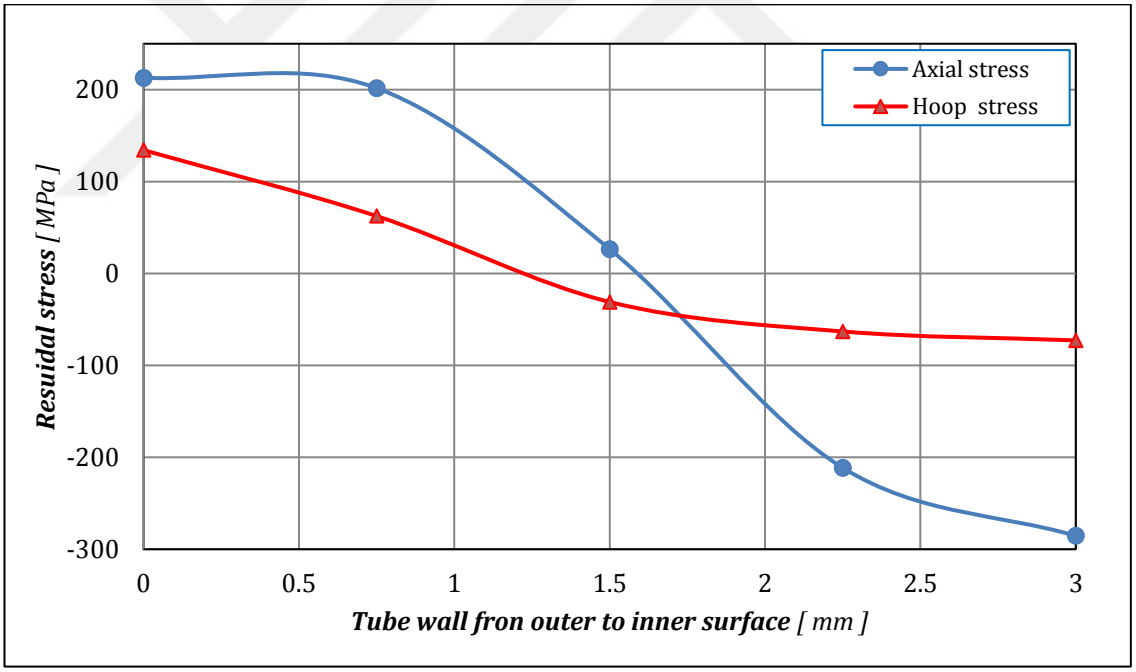


Figure 5.21 Residual stress of final tube by the FEM at R=16%

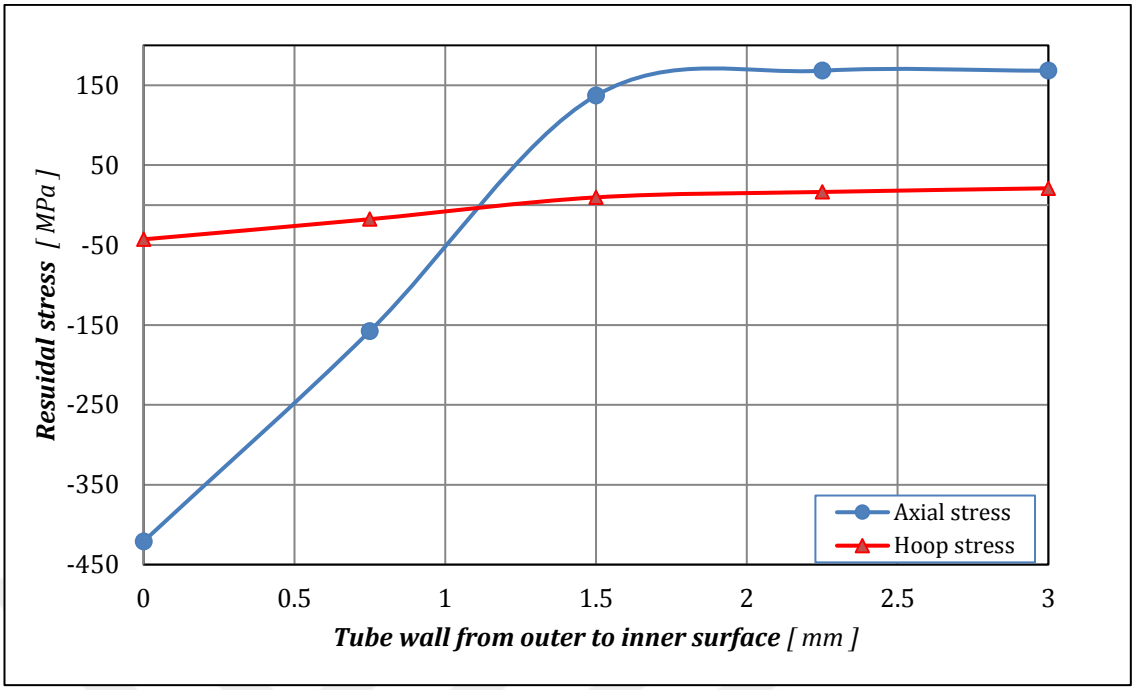


Figure 5.22 Residual stress of final tube by the FEM at R=23%

5.7 Comparison of Residual Stress Results

The measurement results of residual stress within the final tube wall of tubes that was calibrated at R=16% and 23% were compared using the RLM, the SM, the XRD, and the FEM.

5.7.1 Axial Residual Stress by the FEM and the RLM

The comparison between the RLM and the FEM demonstrated the relationship between longitudinal (axial) residual stresses and distance from the outer to the inner surfaces of the final tube wall thickness at R=16 % and 23% as displayed in Fig. 5.23 and 5.24 respectively.

Fig. 5.23 describes the comparison between the FEM and the RLM at R=16% according to the axial residual stress that was measured from the outer to the inner surface. It is clear that the results of the residual stress states gave divergence in the results between the FEM and the RLM because the initial tube subjects to a high temperature during the preparing process. This process leads to the formation of initial residual stresses inside of the initial tube. These initial residual stresses have strong

effect in decreasing or increasing (tension and compression states) on the residual stresses which are generated after the drawing process. In FEM, initial residual stresses are zero within the initial tube wall, so that the residual stresses are high after the drawing process.

The state of residual stress can be shown during the explanation of the behavior. Near the outer surface of the tube when the distance of measurement was precisely 0.25 mm, a state of axial residual stress in tension for both the FEM and the RLM was recorded. This state continued in tension until a distance of about 1.5 mm was reached then the state began to change into the compression until reaching the inner surface of the tube.

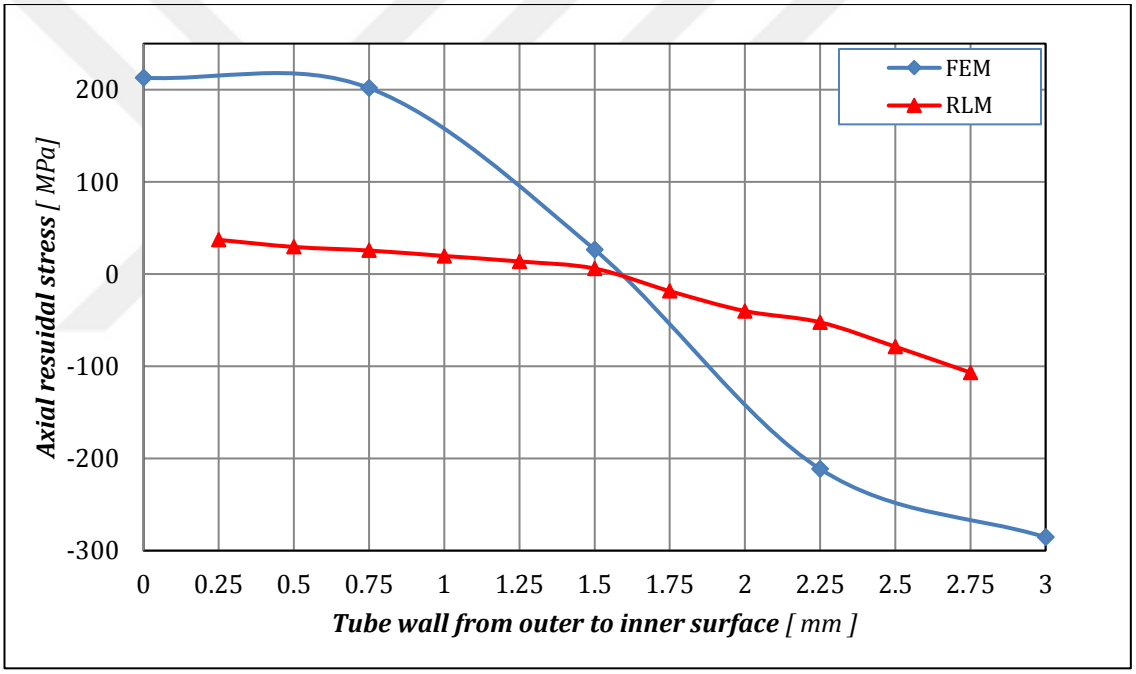


Figure 5.23 Comparison between the FEM and the RLM according to the axial residual stress at R=16%

The behavior of axial residual stress within the tube wall at R=23% is depicted in Fig. 5.24. It can be seen that the state of axial residual stress near the outer surface of the tube is in compression while the state of axial residual stress in the middle and around the core of the tube wall is in tension.

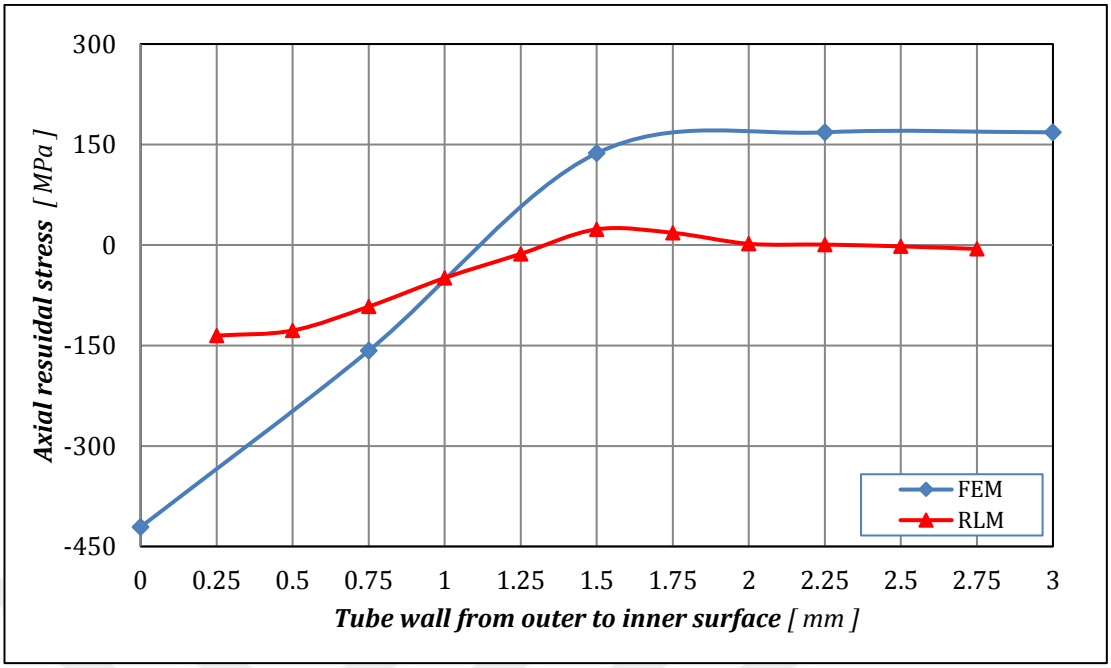


Figure 5.24 Comparison between the FEM and the RLM according to the axial residual stress at R=23%

In both comparisons at R=16% and 23% that shown in Fig. 5.23 and 5.24 respectively, there is a discrepancy in the results at magnitudes at some points especially near the outer and the inner surfaces of the final tube. In fact, this discrepancy can be explained and divided into two reasons. First, the results of internal stresses obtained from the FEM were generated as uniform plastic deformations in forming region while they are non uniform in reality. Second, the results of residual stress measurements obtained by the RLM were average along the area that were milled from tube wall for each layer while in FEM, the average value was determined according to the number of nodes along of the tube wall and assumed without initial residual stresses.

5.7.2 Hoop Residual Stress by the FEM, the SM, the RLM and the XRD

By utilizing the RLM, the SM, the FEM and the XRD, the circumferential (hoop) residual stresses inside the final tube wall were compared at R=16% and 23% as presented in Figs. 5.25 and 5.26 respectively.

Fig. 5.25 introduces the comparison between the FEM, the SM, the RLM and the XRD with the hoop residual stress of a final tube produced at R=16%. As indicated in the

figure, the results showed a good agreement in state of residual stress with discrepancy in values near the outer and the inner surfaces according to the FEM. The SM, the RLM and the XRD results are close to each other. This good correlation indicates that the initial setups for residual stress measurements are sufficiently good. The FEM, the SM, the RLM and the XRD have the same behavior that agreed with residual stress behaviors that introduced in Refs. [59] and [61].

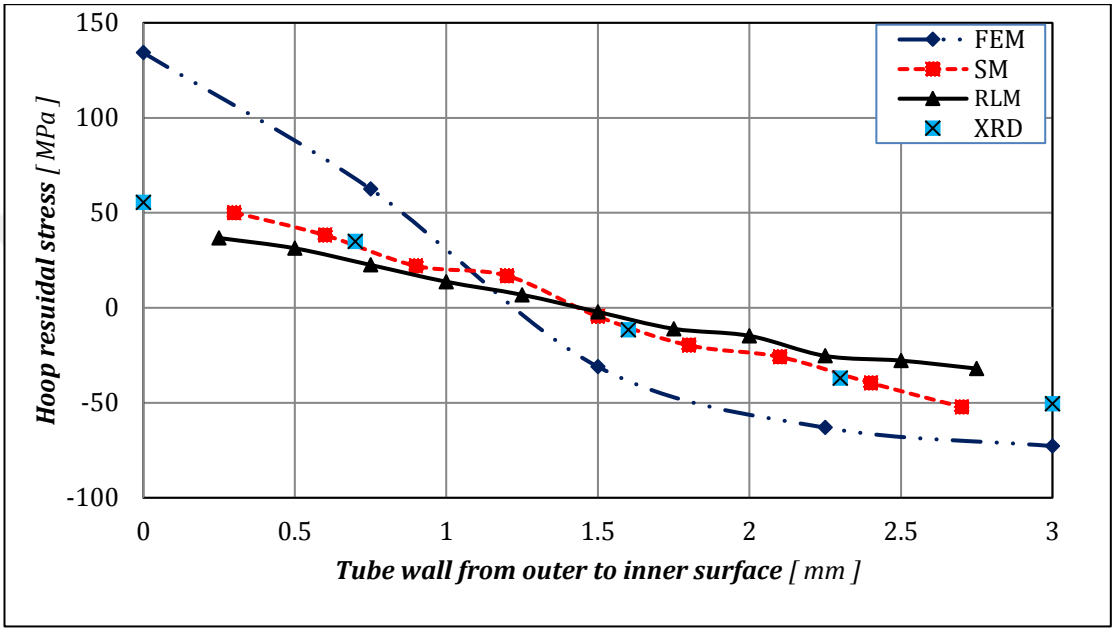


Figure 5.25 Comparison between the FEM, the SM, the RLM, and the XRD according to the hoop residual stress at R=16%

For R=23%, the results of the hoop residual stress measurements were compared between the FEM, the SM, the RLM and the XRD. There is a convergence result, especially between the SM and the RLM. The behaviors of residual stresses were in good agreement while some differences in the results were due to the amount of cross section area that was milled. Using RLM, a layer was removed from the whole surface of the tube wall and strains were measured while using SM, the strains were recorded by milling a part of the layer from the surface of the tube. The results of the XRD and FEM have discrepancy due to the reasons that were mentioned above.

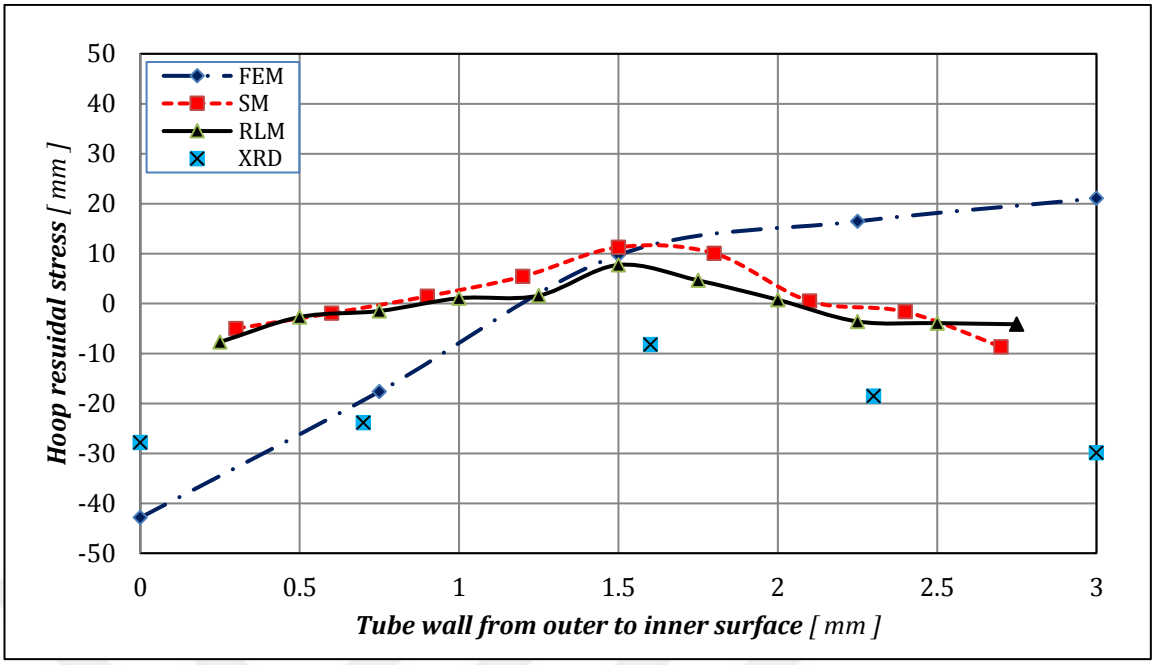


Figure 5.26 Comparison between the FEM, the SM, the RLM and the XRD according to the hoop residual stress at R=23%

There was a discrepancy in the results when the RLM was compared with the FEM and the XRD. However, the behaviors of residual stresses states were similar near at the outer surface of tube wall. In residual stress comparisons, it is natural that there is a divergence between experimental, real-world measuring methods (RLM, SM and XRD) and numerical method (FEM). For discrepancy between RLM and SM, the area milled to measure residual stress by RLM is bigger than the area that was removed by SM. For the divergence between RLM and FEM, plastic deformations are uniform in FEM while they are non uniform in reality as well as initial residual stresses not been taken into consideration for FEM. For the XRD results, the average value for the five orientation was considered as well as there is a reliability in results and accurate measurement for the depth of residual stress.

5.8 Results of Optimum Parameters for Drawing Process by the FEM

Optimum parameters of the tube drawing process with a fixed mandrel that give minimum drawing stress were successfully determined using the FEM by the AFEM.

5.8.1 Effect Semi Die/Plug Angles on Plastic Deformations

Figs. 5.27 and 28 show PEEQ distribution inside tube wall. In Fig. 5.27, semi die angle is 12°, semi plug angle is 0°, and coefficient of friction is 0.1 while in Fig. 5.28, semi die angle is 7°, semi plug angle is 4°, coefficient of friction is 0.1, and drawing velocity 4.25 m/min. It is obvious that there is a clear difference in the plastic deformation for the two figures due to the change in semi die/plug angles. The plastic deformation occurs as a result of dislocation motions that become a linear defect in the crystal structures. A preferred orientation is produced since the crystallographic directions gradually rotate toward more stable orientations that represent the drawing direction and this leads to isotropic material transformation into anisotropic [11]. The effect of semi die angle is larger than the effect of semi plug angle on plastic deformations due to the increase in plasticity (higher dislocation density) that takes place in the contact region.

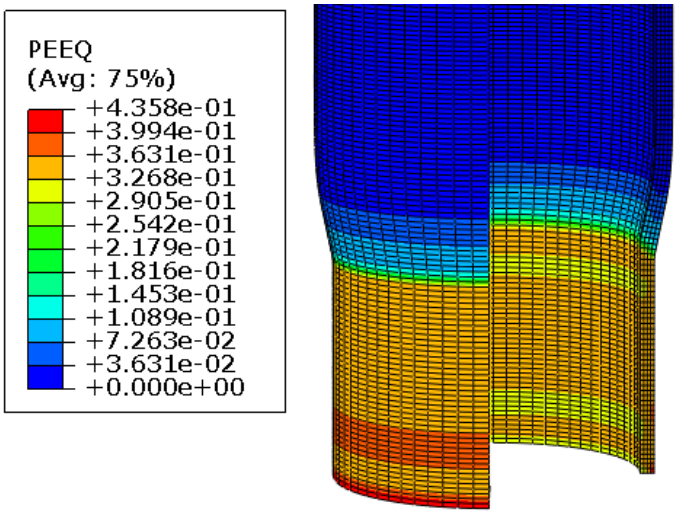


Figure 5.27 PEEQ axisymmetric finite element model at semi die angle of 12° and semi plug angle of 0°

In Fig. 5.27, it can be seen that the plastic deformation of the outer surface of the tube is larger than the inner surface of the tube due to the high effect of semi die angle. In Fig. 5.28, it can be observed that the effect of the semi plug angle is larger than the semi plug angle. So that, the plastic deformation at the surface of the tube is the largest.

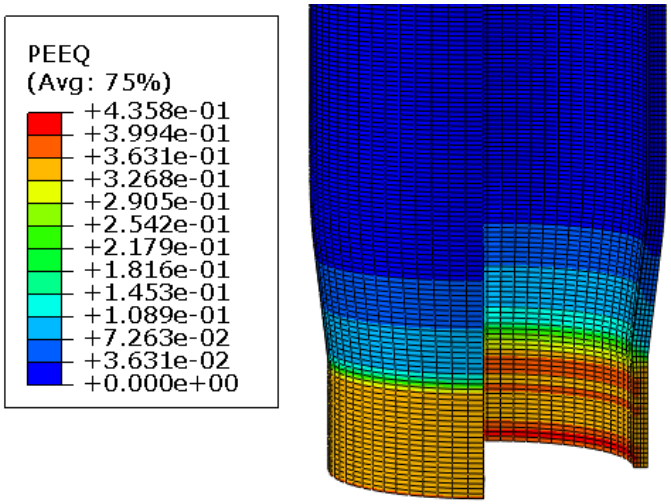


Figure 5.28 PEEQ axisymmetric finite element model at the semi die angle of 7° and the semi plug angle of 4°

5.8.2 Effect Semi Die Angle on Drawing Force

Drawing force vs. displacement at different semi die angles were plotted in Fig. 5.29. The figure shows the effect of the semi die angle on drawing force vs. displacement plot for the case of semi plug angle of 0° and coefficient of friction of 0.1. The behaviors of all semi die angles were similar while drawing passes are different. The drawing force when the semi die angle was equal to 10° was recorded to be less than at semi die angles of 5° and 7° because of the decrease in plastic deformation in contact areas [76]. It can be clearly seen that the drawing force sharply raises when the tube is fully in contact with nib die and with fixed plug due to the increase in plastic deformation, after which the drawing force is almost constant because a steady forming state is reached that allows a constant drawing force. Finally, the drawing force is decreased when the tube exits the die.

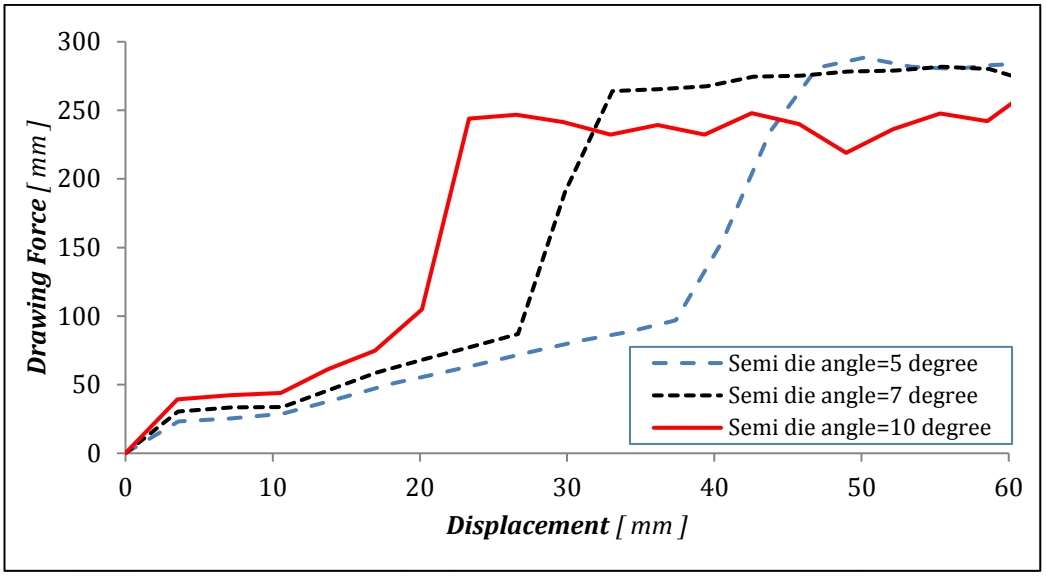


Figure 5.29 Relationship between drawing force and displacement at different semi die angles

5.8.3 Effects Semi Die Angle on Drawing Stress at Different Coefficients of Friction

The drawing stress was measured when the tube exit from the bearing length. The effect of the semi die angle on the drawing stress with a constant semi plug angle of 0°at different friction coefficients were plotted in Fig. 5.30. The figure indicates that the drawing stress corresponding to the semi die angles of 5° and 7° were recorded larger than other semi die angles because of the increase in dislocation density. A Semi die angle produces differences in friction, as well as having the effect of redundant plastic deformation [76]. The redundant deformation represents both friction and shear deformation and it is a radial strain. Therefore, it can be concluded that the semi die angle has a strong effect on drawing stress. The minimum drawing was determined at a semi die angle of $12° - 15^{\circ}$and semi plug angle 0° with friction coefficients of 0.1, 0.125, and 0.15 correspondingly. The relative drawing stress σ_r can be determined by dividing drawing stress (σ_d) by yield stress (σ_o) should be less than 1. If the relative drawing stress is larger than 1, this means that the tube subjected to the high stresses larger than yield stress. Table 5.13 shows all results for all models that simulated in this study.

$$\sigma_r = \frac{\sigma_d}{\sigma_o} \leq 1 \qquad (\mathbf{5.1})$$

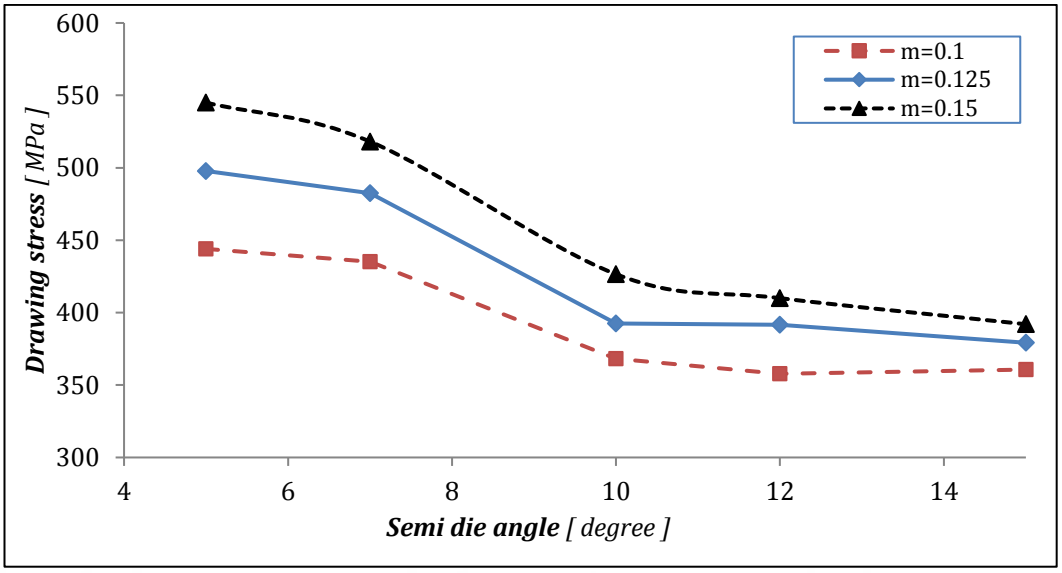


Figure 5.30 Relationship between the drawing stress and the semi die angle at different friction coefficients

Table 5.13 Results of relative drawing stress for all simulations

α (degree)	αp (degree)	μ	F_{dr} (N)	σ_d (MPa)	σ_r
5	0	0.1	280230	444.006	0.792
		0.125	314920	498.970	0.891
		0.15	344271	545.474	0.974
7	0	0.1	274643	435.153	0.777
		0.125	304454	482.387	0.861
		0.15	327005	518.118	0.925
10	0	0.1	232373	368.179	0.657
		0.125	247732	392.515	0.700
		0.15	269207	426.540	0.761
12	0	0.1	225804	357.771	0.638
		0.125	247216	391.697	0.699
		0.15	258732	409.943	0.732
15	0	0.1	227520	360.490	0.643
		0.125	231424	366.676	0.654
		0.15	247.826	392.664	0.701
7	1	0.1	303621	481.067	0.859
		0.125	327803	519.382	0.927
		0.15	344751	546.235	0.975
7	2	0.1	297427	471.253	0.841
		0.125	322905	511.621	0.913
		0.15	337302	534.432	0.954
7	3	0.1	280631	444.641	0.794
		0.125	300005	475.338	0.848
		0.15	318300	504.325	0.900
7	4	0.1	276800	438.571	0.783
		0.125	301506	477.716	0.853
		0.15	319256	505.840	0.903

5.8.4 Effects Semi Plug Angles on Drawing Stress at Different Coefficients of Friction

Fig. 5.31 presents the relationship between semi plug angle and drawing stress at a constant semi die angle of 7° at different friction coefficients. The minimum drawing stress was found with semi plug angle of 0° and 4°. The maximum drawing stress was estimated with a semi plug angle of 1° because of the increase in plastic deformation at the inlet and the outlet of the dies. There is the possibility to use a semi plug angle between 2° to 4° with the semi die angle 7° that can a give very good surface finish on the internal surface of the tube [77].

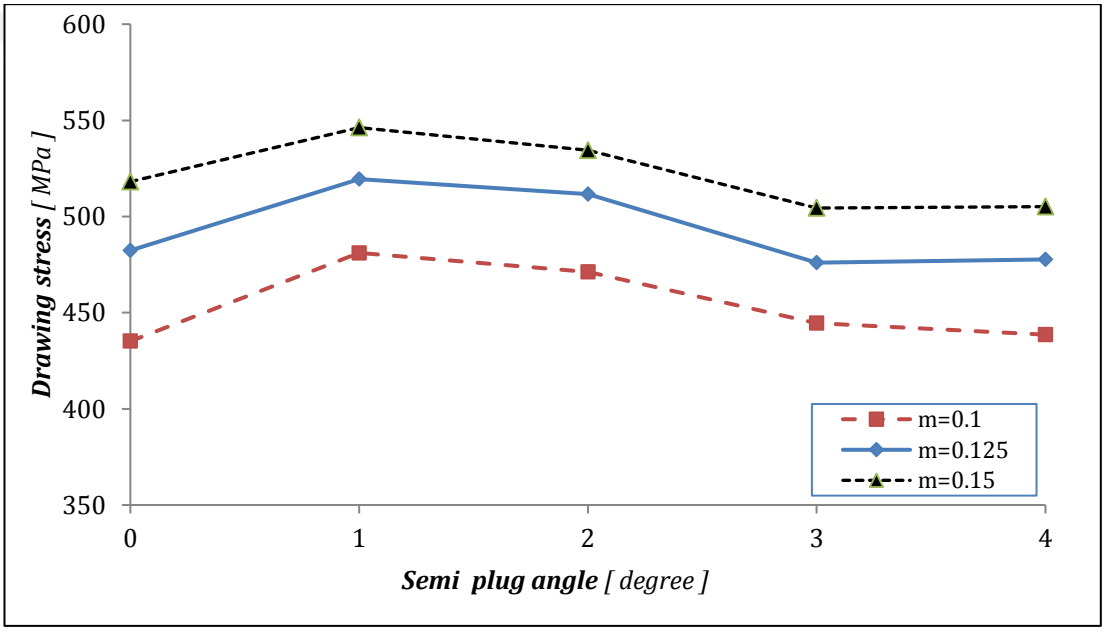


Figure 5.31 Relationship between the drawing stress and the semi plug angle at different friction coefficients

CHAPTER 6

CONCLUSION AND FUTURE WORKS

6.1 Conclusion

In this study, two main objectives have been investigated. First, experimental and numerical determination of force vs. displacement by compression process and analysis of a tube drawing process with a fixed mandrel numerically were performed. Second, behaviors of residual stresses within the final tube wall were efficiently measured and studied using the experimental and numerical approach.

AISI 1010 steel tube was drawn by two different dimensions using two dies and mandrels that showed a high efficiency for the tube production. Residual stresses within the tube wall experimentally and numerically were determined. Experimental study was conducted to measure residual stresses inside the tube wall for two reduction of areas R=16% and 23%. For each reduction of area 9 samples were used. Numerical method was investigated with R=23% to study the effect different parameters on drawing stress. Semi die angles ($5^{\circ}, 7^{\circ}, 10^{\circ}, 12^{\circ}, 15^{\circ}$) were studied with constant semi plug angle 0°. Semi plug angles ($0^{\circ}, 1^{\circ}, 2^{\circ}, 3^{\circ}, 4^{\circ}$) were studied with constant semi die angle 7°. The friction coefficients of 0.1, 0.125, and 0.15 were chosen for all models. In this Ph.D. thesis, following conclusions were drawn.

- According to the compression force vs. displacement plots with R=16% and 23%, the results of the experimental and FEM approaches revealed in a good agreement with a minimum discrepancy.

- The drawing force depends on the amount of the reduction in the outer and the inner diameters of the tube that give various drawing pass. For that reason, the plastic deformations are different.

- The results of the RLM, SM, XRD, and FEM were in high acceptability in the describing the behavior of hoop residual stresses inside the tube wall. For

R=16%, the results of the RLM, the SM and the XRD are close to each other compared with the FEM. For R=23%, the results of the RLM and the SM were close to each other compare with the XRD and FEM.

- The fundamental point that was demonstrated in this study that the RLM using milling machine is the most appropriate method to measure residual stresses inside the tube wall since it has ability to measure residual stress along tube surface with the axial and the hoop directions at the same time.

- The reduction of area has a strong effect on the behavior of residual stress. The behavior of the axial and the hoop residual stress are in different states for R=16% and 23% because the deformation zone depends largely upon the reduction of area due to the change in the reduction of the tube dimensions.

- A semi die angle of $12°$ and $15°$ gave minimum drawing stress for all coefficients of friction 0.1, 0.125, and 0.15.

- A semi plug angle between 2° and 4° should be used in a tube drawing process with a conical fixed plug when the semi die angle is equal to 7^{o}.

- Drawing stress increases with increasing coefficients of friction for all semi die/plug angles because of the increase in energy consumption due to the friction between tools and material during the drawing process.

- The minimum relative drawing stress (0.638) was determined when the semi die angle 12°, semi plug angle 0°, and friction coefficient 0.1 while the maximum relative drawing stress (0.975) was founded with semi die angle 7°, semi plug angle 1° and friction coefficient 0.15.

The present study covered all objectives that planed in the starting of the work. However, some points appeared during the experimental works can be improved or achieved as a future works.

6.2 Future Works

The future works can be divided into two areas. The first one is tube drawing process with a fixed mandrel. The second is to improve performance of the residual stress measurements using RLM and SM by means of a milling process. The recommendations for future works can be summarized as follows:

- Studying the influence of the tube drawing parameters (the nib die geometry, the plug geometry, and the reduction of area) are very important in determining residual stress distributions inside the tube wall. It can produce the tubes with different semi die angle at a constant semi plug angle then residual stresses are measured to estimate the optimum semi die angle that can give minimum residual stress near the outer surface of the tube wall. On the other hand, utilizing various semi plug angle allow choosing the best angle that generates minimum residual stress close the inner surface of the final tube wall. Reduction of area (R %) represents the amount of the reduction in inner and outer diameters of the tube. Therefore, it is necessary to study the effect reduction area on the residual stress distribution according to the change in dimension of the outer diameter and the tube thickness at the constant reduction in inner diameter.

- The most important recommendations are with respect to improving the RLM. Two parameters should be studied when the residual stresses using the RLM are measured by means of the milling process for the tube layers. These parameters are the cutting speed and the feed rate that have impact effect in identified the measurement time. Moreover, there is a possibility to predict accurate results with minimum noise that happens through the residual strain measurements.

- By utilizing the SM, there is an urgent need to study the effect cutter diameter that has a range between 2-4 mm on the results of residual stresses measurement.

- Using the RLM to measure residual stresses inside the tube wall that produced with different semi die angle and semi plug angle.
- Measuring the initial residual stresses inside the initial tube wall by using RLM and the SM to compare with the FEM.
- Using the hole drilling method to determine residual stresses at the same distance inside tube wall with different positions, then the average value is calculated to compare results with the RLM.
- Determining the residual stresses inside the tube wall using FEM with different reduction of area, semi die angle, semi plug angle, and friction coefficient.

REFERENCES

[1] J. N. Harris, "Mechanical Working of Metals: Theory and Practice", International Series on Materials Science, Vol. 36, 1983.

[2] R. H. Tood, D. K. Allen, and A. Altind, "Manufacturing Processes Reference Guide", Industrial Press Inc. New York, 1994.

[3] H. Tschaetsch, "Metal Forming Practices", Originally German Edition by ViewegVerlag, Wiesbaden, 2005.

[4] Showcase Demonstration, "Improving the Efficiency of Tube Drawing Bench ", Program of the U.S. Department., 1997.

[5] D. S. Chapman, "Effect of Process Variables on the Tube Drawing Process and Product Integrity", Master Thesis, Texas Tech University, 1991.

[6] J. K. Jabbar, "*Calculations of Relative Extrusion Pressure for Circular Section by Local Coordinates System by Using Finite Element Method F.E.M*", Diyal Journal of Engineering Sciences, Vol. 03, No. 02, pp. 80-96, 2010.

[7] C. Linardon, "Precision Tube Drawing for Biomedical Applications: Theoretical, Numerical, and Experimental Study", Ph.D Thesis, Grenoble University, 2006.

[8] T. Yong, O. Dong-shong, W. Zhen-ping, L. Long-shong, and L. Bin, "*Influence of Drawing Process Parameters on Forming of Micro Copper Tube with Straight Grooves*", Transactions of Nonferrous Metal Society of China, Vol.21, pp. 2264-2269, 2011.

[9] M. T. P. Aguilar, E. C. E. Correa, R. F. Silva, and P. R. Cetlin, "*The Evaluation of Redundant Deformation Factors in Axi-Symmetric Bar Drawing of Austenitic Stainless Steel*", Journal of Materials Processing Technology, 125-126, pp. 323-325, 2002.

[10] G. E. Dieter, H. A. Kuhn, and S. L. Semiatin, "Handbook of workability and process design", ASM International, Chapter 19: p. 278-290, 2003.

[11] J. Chakrabarty, "Theory of plasticity" Third Edition,Texas: Butterworth-Heinemann, 2006.

[12] L. Lazzarotto, L. Dubar, A. Dubois, P. Ravassard, and J. Oudin, "*Identification of Coulomb's Friction Coefficient in Real Contact Conditions Applied to a Wire Drawing Process*", Wear Journal, Vol. 211, pp. 54-63, 1997.

[13] M. S. Joun, H. G. Moon, I. S. Choi, M. S. Lee, and B. Y. Jun, "*Effects of Friction Laws on Metal Forming Process*", Tribology International, Vo. 42, pp. 311-319, 2009.

[14] L. Wang, and H. Yang, "*Friction in Aluminum Extrusion-Part 2: A Review Friction Models for Aluminum Extrusion*", Tribology International, Vol. 56, pp. 99-106, 2012.

[15] G. Ravichandran, A. J. Rosakis, J. Hodowany, and P. Rosakis, "*On the Conversion of Plastic Work into Heat During High-Strain-Rate Deformation*", In Shock Compression of Condensed Matter, pp. 557-562, 2001.

[16] W. T. Wu, J. T. Jinn, and C. F. Fischer, " Handbook of Workability and Process", ASM International, Chapter 15, p. 220-229, 2003.

[17] K. K. Um, and D. N. Lee, "*An Upper Bound Solution of Tube Drawing*", Journal of Materials Processing Technology, Vol. 63, pp. 43-48, 1997.

[18] N. Schwarzer, H. Djabella, F. Richter, R.D. Arnell, "*Comparison between Analytical and FEM Calculations for the Contact Problem of Spherical Indenters on layered Materials*", Journal Thin Solid Films, Vol. 270, pp. 279-282, 1995.

[19] S. I. Oh, "*Finite Element Analysis of Metal Forming Processes with Arbitrarily Shaped Dies*", International Journal Mechanical Science, Vol. 24, pp. 479-493, 1982.

[20] A. F. Hassan, and A. S. Hashim, "*Three-Dimensional Finite Element Analysis of Wire Drawing Process*", Universal Journal of Mechanical Engineering, Vol. 3, pp. 71-82, 215.

[21] A. Khennane, "Introduction to Finite Element Analysis Using Matlab and ABAQUS", Taylor & Francis Group, LLC, 2013.

[22] M. Cebron, F. Kosel, J. Kopac, "*Effect of Cutting on Surface Hardness and Residual Stress for 12Mn Austenitic Steel*", Journal of Achievements in materials and Manufacturing Engineering, Vol. 55, pp. 80-89, 2012.

[23] G. S. Schajer, "*Destructive Methods for Measuring Residual Stresses: Techniques and Opportunities*", SEM Annual Conference, 2010.

[24] G. S. Schajer, "Practical Residual Stress Measurement Methods", Wiley & Sons Ltd, 2013.

[25] M. R. Hill, M. D. Olson, "*Repeatability of the Contour Method for Residual Stress Measurement*", Journal of Experimental Mechanics, Vol. 54, pp. 1269-1277, 2014.

[26] W. Cheng, I. Finnie, "*Residual Stress Measurement and Slitting Method*", Springer Science-Business Media, LIC, 2007.

[27] Y. H. Zhang, S. Simith, L. Wei, C. Johnston, "Residual Stress Measurement and Modelling", TWI LTd, 2012.

[28] K. Farahaninia, "Experimental Measurement of Residual Stresses in Cold-Drawn Aluminum Tubes", Master Thesis, Texas Technical University, 1990.

[29] A.A. Garcia-Granada, D. J. Smith, and M. J. Pavier, "*A New Procedure Based on Sach's Boring for Measuring Non Axisymmetric Residual Stresses*", International Journal of Mechanical Sciences, Vol. 42, pp. 1027-1047, 2000.

[30] H. Kitano, S. Okano, M. Mochizuki, "A study for High Accuracy Measurement of Residual Stress by Deep Hole Drilling Technique", IOP Publishing Ltd, Conference Series 379, 2012.

[31] C. Garza, D. J. Smith, A. Shterenlikht, and M. J. Pavier, " *Advances in Deep-Hole Drilling Technique for Residual Stress Measurement in Composite Laminates*", V ECCOMAS Thematic Conference on the Mechanical Response of Composites, 2015.

[32] G. S. Schajer, "*Hole-Drilling Residual Stress Measurements at 75: Origins, Advances, Opportunities*", SEM Annual Conference, 2009.

[33] G. Petrucci, and M. Scafidi, "*A New Procedure for the Evaluation of Residual Stresses by the Hole Drilling Method Based on Newton-Raphsion Technique*", JCPDS-International Center for Diffraction Data, pp. 643-650, 2009.

[34] F. L. Cincinnati, Oh, "Measurement of Residual Stresses Using Ring-Core Technique", Lambda Technologies, No.31, 2005.

[35] D. Y. Ju, R. Mukai, N. Minakawa, Y. Morii, A. Moriai, "*A Measurement Method of Residual Stress in Quenched Steel by Neutron Diffraction*", Journal of Engineering Materials, Vols. 270-273, pp. 139-146, 2004.

[36] J. R. Hervias, J. M. Atienza, M. Elices, "*Synchrotron Strain Scanning for Residual Stress Measurement in Cold-Drawn Steel Rods*", Journal Strain Analysis, Vol. 46, pp. 627-637, 2011.

[37] R. B. Ceglias, J. M. Maria, R. B. Botelho, E. B. Junior, I. C. Santos, N. C. Moraes, R. V. Oliveira, S. B. Diniz, L. P. Brandao, "*Residual Stress Evaluation by X-Ray Diffraction and Hole-Drilling in an API 5L X70 Steel Pipe Bent by Hot Induction*", Journal of Materials Research, Vol. 5, pp. 1176-1179, 2016.

[38] M. E. Fitzpatrick, A. T. Fry, P. Holdway, F. A. Kandil, J. Shackleton, and L. Suominen, "Determination of Residual Stresses by X-ray Diffraction - Issue 2", National Physical Laboratory NPL, 2005.

[39] F. Uzun, and A. N. Bilge, "*Investigation of Total Welding Residual Stress by Using Ultrasonic Wave Velocity Variations*", Gazi University Journal of Science, Vol. 24, pp. 135-141, 2011.

[40] S. Abuku, and B. D. Cullity, "*A Magnetic Method for the Determination of Residual Stress*", Experimental Mechanics, pp. 217-223, 1971.

[41] F. O. Neves, S. T. Button, C. Caminage, and F. C. Gentile, "*Numerical and Experimental Analysis of Tube Drawing with Fixed Plug*", Journal of the Brazilian Society of Mechanical Sciences and Engineering, Vol. XXVII, No. 4, pp. 426-431, 2005.

[42] S. W. Kim, Y. N. Kwon, Y. S. Lee, and J. H. Lee, "*Design of Mandrel in Tube Drawing Process for Automotive Steering Input Shaft*", Journal of Material Processing Technology, 187-188, pp. 182-186, 2007.

[43] S. K. Lee, D. C. Ko, B. M. Kim, J. H. Lee, S. W. Kim, and Y. S. Lee, "*A Study on Monobloc Tube Drawing for Steering Input Shaft*", Journal of Materials Processing Technology, Vol. 191, pp. 55-58, 2007.

[44] L. P. Morcira, G. Rodrigues, and L. C. Lopes, "*Finite Element Analysis of The Tube Flow Forming Process*", International Journal Mechatronics and Manufacturing, Vol. 1, Nos. 2/3, pp. 218-231, 2008.

[45] J. Danckert, and B. Endelt, "*LS-DYNA Used to Analysis the Drwaing of Precision Tubes*", 7th European LS-DYNA Conference, 2009.

[46] J. F. Beland, M. Faford, A. Rahem, G. D. Amours, and T. Cote, "*Optimization on the Cold Drawing Process of 6063 Aluminum Tubes*", Applied Mathematical Modelling, Vol. 35, pp. 5302-5313, 2011.

[47] R. Bihamta, Q. H. Bui, M. Guillot, G. Amours, A. Rahem, and M. Fafard, "*A New Procedure for Production of Variable Thickness Aluminum Tubes: Numerical and Experimental Studies*", Journal of Materials Processing Technology, Vol. 211, pp. 578-589, 2011.

[48] Q. H. Bui, R. Bihamta, M. Guillot, G. Amours, A. Rahem, and M. Fafard, "*Investigation of the Formability Limit of Aluminum Tubes Drawn with Variable Wall Thickness*", Journal of Materials Processing Technology, Vol. 211, pp. 402-414, 2011.

[49] R. Bihamta, Q. H. Bui, M. Guillot, G. Amours, A. Rahem, and M. Fafard, "*Application of a New Procedure for the Optimization of Variable Thickness Drawing of Aluminum Tubes*" CIRP Journal of Manufacturing Science and Technology, Vol. 5, pp. 142-150, 2012.

[50] M. Palengat, G.Chagnon, D.Favier, H.Louche, C.Linardon, and C.Plaideau, "*Cold Drawing of 316L Stainless Steel Thin-Walled Tubes: Experiments and Finite Element Analysis*", International Journal of Mechanical Sciences, Vol. 70, pp. 69–78, 2013.

[51] C. Linardon, D. Favier, G. Chagnon, and B. Gruez, "*A Conical Mandrel Tube Drawing Test Designed to Assess Failure Criteria*", Journal of Materials Processing Technology, Vol.214, pp. 347– 357, 2014.

[52] J. Sheu, S. Lin, and C. Yu, "*Optimum Die Design for Single Pass Steel Tube Drawing with Large Strain Deformation*", Procedia Engineering, Vol. 81, pp. 688 – 693, 2014.

[53] E. Trana, A. Rotariu, P.Lixandru, L.Matache, C.Enache, and T.Zecheru, "*Experimental and Numerical Investigation on 6082 0 Temper Aluminum Alloy Cartridge Tubes Drawing*", Journal of Materials Processing Technology, Vol. 216,pp. 59–70, 2015.

[54] P. Casari, F. Jacquemin, and P. Davies, "*Characterization of Residual Stresses in Wound Composite Tubes*", Composites: Part A: Applied Science and Manufacturing, Vol. 37, pp. 337–343, 2006.

[55] V.V. Balalov, V.S. Pisarev, and V.G. Moshensky, " *Combined Implementing the Hole-Drilling Method and Reflection Hologram Interferometry for Residual Stresses Determination in Cylindrical Shells and Tubes*", Optics and Lasers in Engineering, Vol. 45, pp. 661–676, 2007.

[56] T. Kuboki, K. Nishida, T. Sakaki, and M. Murata, "*Effect of Plug on Levelling of Residual Stress in Tube Drawing*", Journal of Materials Processing Technology, Vol. 204, pp. 162-168, 2008.

[57] P. Le Grogneca, P. Casari, and D. Choqueuse, "*Influence of Residual Stresses and Geometric Imperfections on the Elasto plastic Collapse of Cylindrical Tubes Under External Pressure*", Marine Structures, Vol. 22, pp. 836–854, 2009.

[58] G. R. Delgadillo, F. Fiorentini, L. D. Rodrigues, J. L. F. Freire, and R. D. Vieira, "*Measurement of Stresses in Pipelines Using Hole Drilling Rosettes*", Conference Proceedings of the Society for Experimental Mechanics Series pp 175-183, 2011.

[59] T. Pirlinga, A. Carrad, and H. Palkowski, "*Residual Stress Distribution in Seamless Tubes Determined Experimentally and by FEM*", Procedia Engineering, Vol. 10, pp. 3080–3085, 2011.

[60] G.H. Farrahi, G. Z. Voyiadjis, S.H. Hoseini, and E. Hosseinian, "*Residual Stress Analyses of Re-Autofrettaged Thick-Walled Tubes*", International Journal of Pressure Vessels and Piping, Vol. 98, pp. 57-64, 2012.

[61] H. Palkowski, S. Brück, T. Pirling, and A. Carradò, "*Investigation on the Residual Stress State of Drawn Tubes by Numerical Simulation and Neutron Diffraction Analysis*", Materials, Vol. 6, pp. 5118-5130, 2013.

[62] O. Shekoofa, J. Wang, J. Qi, J. Zhang, and Z. Yin, "*Analysis of Residual Stress for Mismatch Metal–Glass Seals in Solar Evacuated Tubes*", Solar Energy Materials & Solar Cells, Vol. 128, pp.421–426, 2014.

[63] F. Foadian, A. Carradó, and H. Palkowski, "*Precision Tube Production: Influencing the Eccentricity and Residual Stresses by Tilting and Shifting*", Journal of Materials Processing Technology, Vol. 222, pp. 155–162, 2015.

[64] F. Foadian, A. Carradó, T. Pirling, and H. Palkowski, "*Residual Stresses Evolution in Cu Tubes, Cold Drawn with Tilted Dies –Neutron Diffraction Measurements and Finite Element Simulation*", Materials and Design, Vol. 107, pp. 163-170, 2016.

[65] C.U. Ansel and K. F. Saul, "Advanced Mechanics of Materials and Applied Elasticity", 5th Ed., 2012.

[66] " Dewe-43 Technical Reference Manual"

[67] S. Prevey, "X-Ray Diffraction Residual Stress Techniques", Metals Handbook. 10 Metal Park: American Society for Metals, 380-392, 1986.

[68] P. Rangaswamy, M. B. Prime, M. Daymond, M.A.M. Bourke, B. Clausen, H. Choo, and N. Jayaraman, "*Comparison of Residual Strains Measured by X-ray and Neutron Diffraction in a Titanium (Ti–6Al–4V) Matrix Composite*", Materials Science and Engineering, Vol. A259, pp. 209–219, 1999.

[69] "Abaqus Analysis User's Manual", Dassault System SIMULA Corp, Vol. II, 2016.

[70] F. O. Sonmez, A. Demir, "*Analytical Relations between Hardness and Strain for Cold Formed Parts*", Material Processing Technology, Vol. 186, pp. 163-167, 2007.

[71] Y. H. Moon, D. H. Lee, C. J. Van Tyne, "*Optimum Distribution of the Drawing Strains in the Two-Pass Tube Drawing*", Journal Engineering Manufacture, Vol. 219, pp. 595-602, 2005.

[72] S. O. Onuh, M. Ekoja, and M. B. Adeyemi, "*Effect of Die Geometry and Extrusion of Aluminum and Leads Alloys*", Journal of Materials Processing Technology, Vol.132, pp. 274-285, 2003.

[73] A. S. Rocha, R. M. Nunes, T. Hirsch, "*Change in the Axial Residual Stresses in AISI 1045 Steel Bar Resulting from a Combined Drawing Process Chain*", Journal Engineering Manufacture, Vol. 226, pp. 459-465, 2011.

[74] Z. Wang, B. Gong, "Residual stress in the forming of material", Handbook of Residual Stress Deformation of Steel, ASM, 2002.

[75] M. Akiyama, and T. Kuboki, "*Optimization of Method for Reducing Residual Stresses After Cold Bar Drawing*", Ironmaking& Steelmaking, Vol. 29, pp. 101-106, 2002.

[76] T. Z. Blazynski, "Design of Tools Deformation Processes" Elsever Applied Science Publishers LTD, England, 1986.

[77] G. E. Dieter, H. A. Kuhn, and S. L. Semiath, "Handbook of Workability and Process Design", ASM International, 2003.

APPENDICES

Appendix A: S9 Atlantis Device for the Spectral Test.

Appendix B: Macro Hardness Tester with Cross Slide (Q250).

Appendix C: Reduction of Areas Calculations.

Appendix D: Tee Rosette Strain Gage (TRSG).

Appendix E: Data Logger Device (Dewe 43 A).

Appendix F: Multipurpose XRD System (Ultima IV).

Appendix G: Material Properties of AISI 1010 Steel.

Appendix H: Stable Time Increment Calculation.

Appendix I: Energy Output Using ABAQUS.

Appendix J: Effect the Velocity on Drawing Force.

Appendix K: External Work Calculations for the Compression Process.

Appendix A - S9 Atlantis Device for the Spectral Test

S9 Atlantisis one of the most advanced spark emission spectrometers system and is considered as the top laboratory metal analyzer. It has improved analytical performances, high flexibility and it has very wide range of analytical tasks. It can be used for either routine analysis or research and development needs. Optical system combines the specific advantages of both photomultiplier tubes and CCD detector systems. The spectrometer can mount a cooled table stand and an ultra-vacuum optic by an additional turbo-molecolar pump able to grant the highest sensibility for trace elements analysis such as nitrogen, oxygen, phosphorous and boron in steels, copper, aluminum and titanium alloys. MetalLab32 software, operating in windows environment is used. Operator can apply all the spectrometer's functions in a flexible way and cover all requirements.



Figure (A) S9 Atlantis

Appendix B - Macro Hardness Tester with Cross Slide (Q250)

Q250 is used for the standard hardness test according to Vickers, Rockwell, and Brinell for the fully automatic determination of hardness value. The specifications are described in table A

Table (A) Specifications of Q250

Test load range	0.5-250 kg
Test height	310/310 mm
Software	Qpix control via 19" monitor and external PC
Testing table	Motorized XY cross sledge
Distance X/Y	400×260 mm
Interfaces	3× USB, 1×RS232C, 1× ethernel
Weight basic unit	450 kg
Max. workpiece weight	100 kg
Power supply	230-1/N/PE, 110-1/N/PE
Maximum input	1200 W



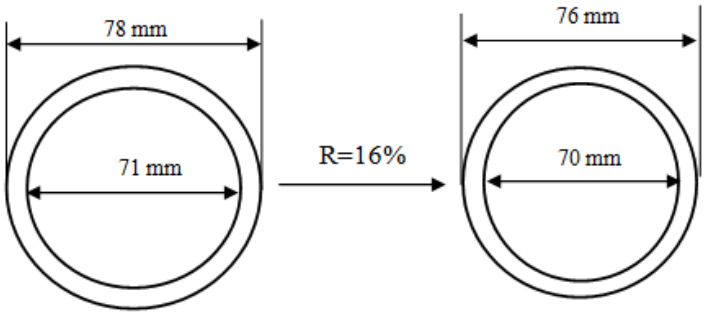
Figure (B) 250Q Macro hardness tester

Appendix C - Reduction of Areas Calculation

$$R\% = 1 - \frac{D_i^2 - (D_i - 2t_i)^2}{D_o^2 - (D_o - 2t_o)^2}$$

Outer diameter of initial tube $D_o = 78\ mm$, Thickness of initial tube $t_o = 3.5\ mm$

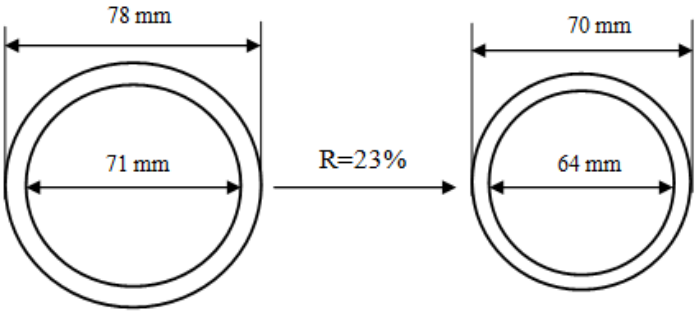
R=16%



Outer diameter of final tube $D_i = 76\ mm$, Thickness of final tube $t_i = 3\ mm$

$$R\% = 1 - \frac{76^2 - (76 - (2\times3))^2}{78^2 - (78 - (2\times3.5))^2} = 16\%$$

R=23%



Outer diameter of final tube $D_i = 70\ mm$, Thickness of final tube $t_i = 3\ mm$

$$R\% = 1 - \frac{70^2 - (70 - (2\times3))^2}{78^2 - (78 - (2\times3.5))^2} = 23\%$$

Appendix D - Tee Rosette Strain Gage (TRSG)

Two element 90° tee rosette is used for general purposes. Exposed solder tab area is 2.5×1.8 mm. Table (B) depicts TRSG specifications.

Table (B) Specifications of TRSG

Resistance	120 ±0.4 Ω
Gage designation	CEA-XX-125UT-120
Gage length	3.18 mm for each section
Overall length	8.26 mm complete pattern
Grid width	4.19 mm for each section
Overall width	9.27 mm complete pattern
Matrix length	10.7 mm
Matrix width	11.4 mm
Strain range	±5%
Temperature range	-75° to +175°C

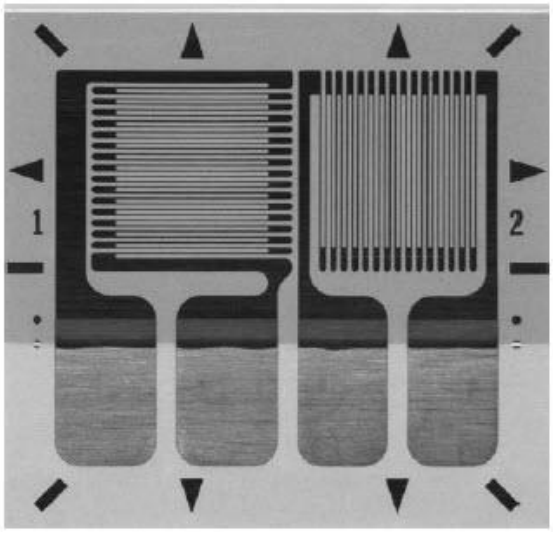


Figure (C) TRSG

Appendix E - Data Logger Device (Dewe 43 A)

Dewe 43 A is used to measure the resistance that can convert to strain using bridge. Table (C) presents specification of Dewe 43 A [67].

Table (C) Specifications of Dewe 43 A

Number of Channels	8
Inputs	Voltage, bridge (IEPE, temperature with adapter)
ADC Type	24 bit sigma delta with anti-aliasing filter
Sampling rate	Simultaneous 200Ks/Sec sampling rate
Input type	Differential
Input ranges	± 10V, ± 1V, ± 100 mV, ± 10 mV
Sensor supply	12V, 400 mA sensor supply ±5V±0.1% bridge sensor supply
Overvoltage protection	±70V input protection
Dynamic range	107 dB@ ± 10V range
DC Accuracy **10 V range** **1 V range** **100 mV range** **10 mV range**	0.05% of value +1 mV 0.05% of value +0.2 mV 0.05% of value +0.1 mV 0.05% of value +0.1 mV
CMRR	>80 dB
Maximum common mode voltage	± 13V
Signal to noise **0.1 kS/s to51.2 kS/s** **51.2 kS/s to 102.4 kS/s** **102.4 kS/s to 200 kS/s**	 105 dB 100 dB 75 dB
Channel to channel phase Mismatch	<0.1 deg@ 5kHz
Phase to phase Mismatch	-0.6 deg@ 1kHz

Appendix F - Multipurpose XRD System (Ultima IV)

The Ultima IV represents the state-of-the-art in multipurpose X-Ray diffraction (XRD) systems. Incorporating Rigaku's patented cross beam optics (CBO) technology for permanently mounted, permanently aligned and user-selectable parallel and focusing geometries, the Ultima IV X-Ray diffractometer can perform many different measurements fast. With a multipurpose diffractometer, performance is measured by not only how fast you perform an experiment but also how fast you can switch between different types of experiments. Individual experiments are optimized with accessories like the D/teXUltra high-speed position sensitive detector system, but the speed between experiments is radically improved with the combination of the automated alignment and CBO. The Ultima IV is the only XRD system on the market today that incorporates fully automatic alignment. When coupled with CBO and the in-plane arm, the automatic alignment capability makes the Ultima IV X-Ray diffractometer the most flexible system available for multipurpose applications. In the Ultima IV XRD system, CBO technology eliminates time spent switching geometries, enables everyday users to run both sets of experiments without the need to reconfigure the system, and reduces wear and possible optic damage associated with the recurrent switching process. CBO and automatic alignment combine for the ultimate in functionality for: micro-crystalline diffraction, thin-film diffraction, small angle scattering, and in-plane scattering. The features of Ultima can be divided into:

- Full automated alignment under computer control.
- Optional in-plane diffraction arm for in-plane measurements without reconfiguration.
- Focusing and parallel beam geometries without reconfiguration.
- SAXS capabilities.
- Optional D/teXUltra high-speed, position-sensitive detector system.

Table (D) Specifications of Ultima IV

X-ray generator	Maximum rated output	3 KW
	Rated tube voltage	20-60 kV
	Rated tube current	2-60 mA
	Target	Cu (others: optional)
	Focus size	0.4 x 12 mm (others: optional)
Goniometer	Scanning mode	θs/θd coupled or θs, θd independent
	Goniometer radius	285 mm
	2θ measuring range	-3 to 162° (maximum)
	Minimum step size	0.0001°
Optics	Divergence slit	Fixed or automatic variable
	Scattering slit	Fixed or automatic variable
	Receiving slit	Fixed or automatic variable
	Optics alignment	Automatic alignment of tube height, goniometer, optics and detector
	Monochromator	Dual position graphite diffracted beam monochromator for Cu (others: optional)
Detector	Detector	Scintillation counter (others: optional)
Dimensions	H x W x D	1600 x 1100 x 800 mm
	Sample height	1050 mm



Figure (D) Ultima IV

APPENDIX G - Material Properties of AISI 1010 Steel

Table (E.1) Chemical composition of the AISI 1010 carbon steel

Element	Carbon (C)	Phosphorous (P)	Sulfur (S)	Manganese (Mn)	Iron (Fe)
Content%	0.08-0.13%	≤0.040 %	≤0.050 %	0.30-0.60 %	99.18-9.62 %

Table (E.2) Mechanical properties of the AISI 1010 carbon steel

Density	7.722 g/cm3
Tensile strength	610.6014 MPa
Yield strength	560 MPa
Elastic modulus	190-210 GPa
Bulk modulus	140 GPa
Shear modulus	80 GPa
Poisson's ratio	0.27-0.3
Elongation at break (in 50 mm)	20%
Reduction of area	40%
Hardness, Brinell	105
Hardness, Knoop (converted from Brinell hardness)	123
Hardness, Rockwell B (converted from Brinell hardness)	60
Hardness, Vickers (converted from Brinell hardness)	108

Table (E.3) Thermal properties of the AISI 1010 carbon steel

Thermal expansion co-efficient	12.2 µm/m°C
Thermal conductivity	49.8 W/mK

Table (E.4) True stress, true total strain and effective plastic strain of the AISI 1010 carbon steel

Engineering stress (Mpa)	Engineering strain (mm/mm)	True stress (MPa)	True total strain (mm/mm)	Effective plastic strain (mm/mm)
Raw data	Raw data	------	------	------
0	0	0	0	0
560 (yield)	0.00541	563.0296	0.0053954	0
563.3059965	0.005518353	566.4145179	0.005503183	7.53454E-05
573.4345238	0.006138393	576.9544903	0.006119629	0.000590789
583.0440917	0.007130456	587.2014622	0.007105155	0.00147812
597.5460758	0.009114583	602.9924593	0.009073296	0.00329494
603.7464727	0.010912698	610.3349758	0.010853584	0.005004866
606.5022046	0.011904762	613.7224689	0.011834457	0.005953277
607.5011023	0.012710813	615.2229355	0.012630708	0.006735149
608.7067901	0.013888889	617.1610511	0.013793322	0.007879191
609.9468695	0.015438988	619.3638319	0.015321019	0.009385779
610.3946208	0.016927083	620.7268214	0.016785416	0.010837115
610.6014109	0.018105159	621.6564464	0.017943212	0.011986002
609.877866	0.022321429			
607.156746	0.027715774			
602.6785714	0.033172123			
593.9636243	0.039310516			
574.8800705	0.047123016			
550.0784832	0.056981647			
549.0108025	0.057415675			
500.3031305	0.074466766			
474.1580688	0.081535218			
449.5976631	0.086991567			
447.255291	0.087363591			
444.8095238	0.087797619			
442.3983686	0.088355655			
439.8148148	0.088851687			
437.162478	0.089471726			

APPENDIX H - Stable Time Increment Calculation

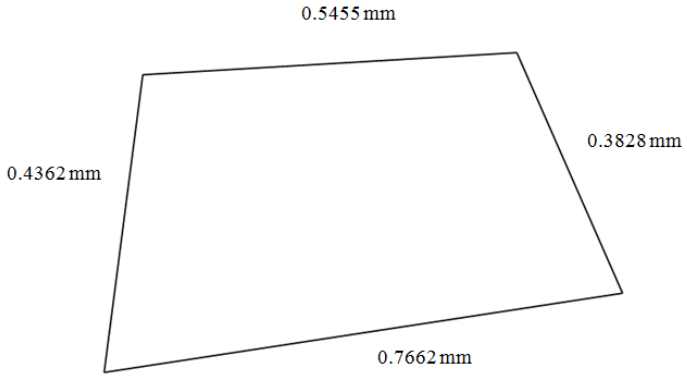


Figure (E) Smallest element dimension for R=23% model

$$\Delta t \approx \frac{L_{min}}{c_d}$$

$$c_d = \sqrt{\frac{\lambda_o + 2\mu_o}{\rho}}$$

$L_{min} = 0.3828$ mm

$\rho = 7.722\times10^{-9}$ tonne/mm^3

E=200000 MPa

v= 0.285

$$\lambda_o = \frac{Ev}{(1+\mathrm{v})(1-2\mathrm{v})} = \frac{200000\times0.285}{(1+0.285)(1-(2\times0.285))} = 103158.0582 \text{ MPa}$$

$$\mu_o = \frac{E}{2(1+\mathrm{v})} = \frac{200000}{2(1+0.285)} = 77821.01167 \text{ MPa}$$

$$c_d = \sqrt{\frac{\lambda_o + 2\mu_o}{\rho}} = \sqrt{\frac{103158.0582 + (2\times77821.01167)}{\rho = 7.722\times10^{-9}}} = 5987060{,}245 \text{ mm/s}$$

$$\Delta t \approx \frac{L_{min}}{c_d} = \frac{0.3828}{5987060{,}245} = 6.393\times10^{-8}\ \text{s}$$

Stable time increment chosen by ABAQUS/Explicit is 4.451×10^{-8} s (fully automatic)

$$\frac{\text{Stable time increment chosen by ABAQUS}}{\text{Stable time increment estimate}} = \frac{4.451\times10^{-8}}{6.393\times10^{-8}} = 0.7$$

Factor is $1/\sqrt{3}$ to 1 that equal 0.58 to 1 0.7 within range factor.

APPENDIX I - Energy Output Using ABAQUS

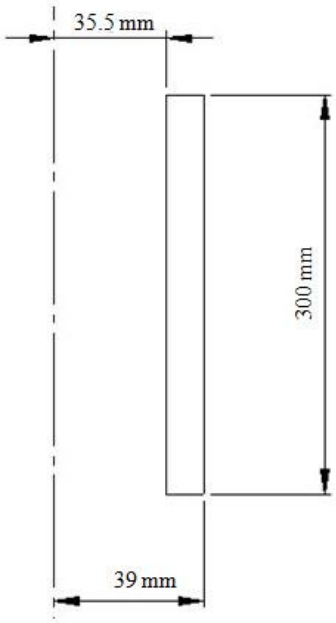


Figure (F.1) Dimensions of axisymmetric for the initial tube

$m = \rho \times \mathrm{V}$

$\mathrm{V} = A \times L = 818.755 \times 300 = 245626.5\ mm^2$

$m = 7.722 \times 10^{-6} \times 245626.5 = 1.8967\ \mathrm{kg}$

$\mathrm{ALLKE} = \frac{1}{2} mV^2 = 0.5 \times 1.8967 \times 71^2 \times 10^{-6}$

$= 4.78 \times 10^{-3}\ \mathrm{kJ} = 4.78\ \mathrm{mJ}$

Energy Output for Tube Drawing at R=16%

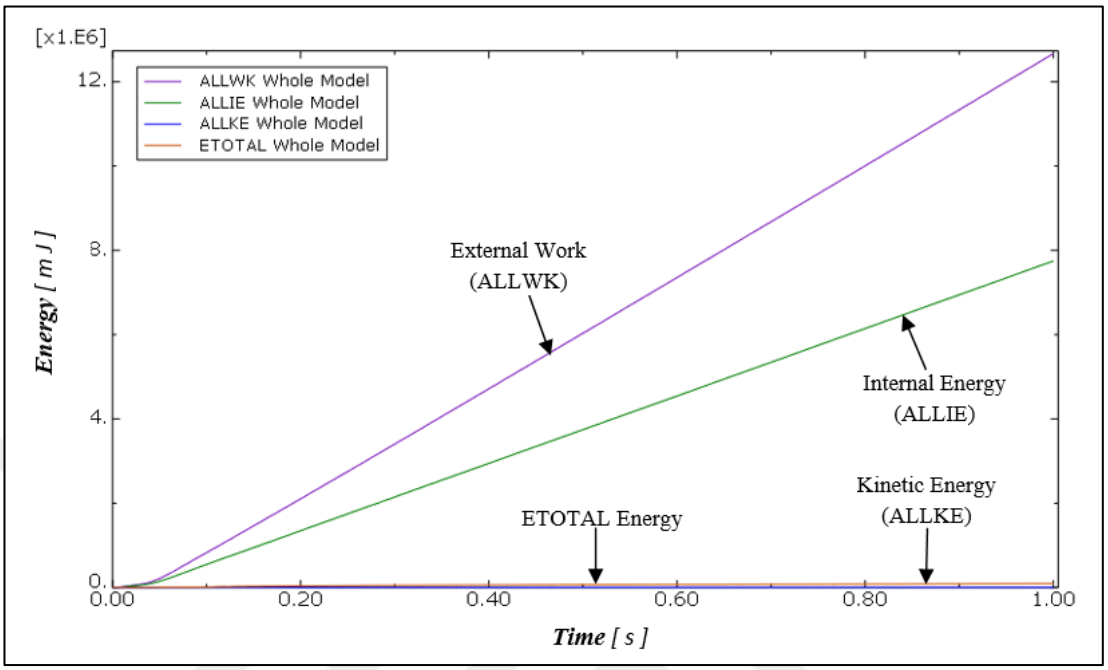


Figure (F.2) Energy output for R=16%

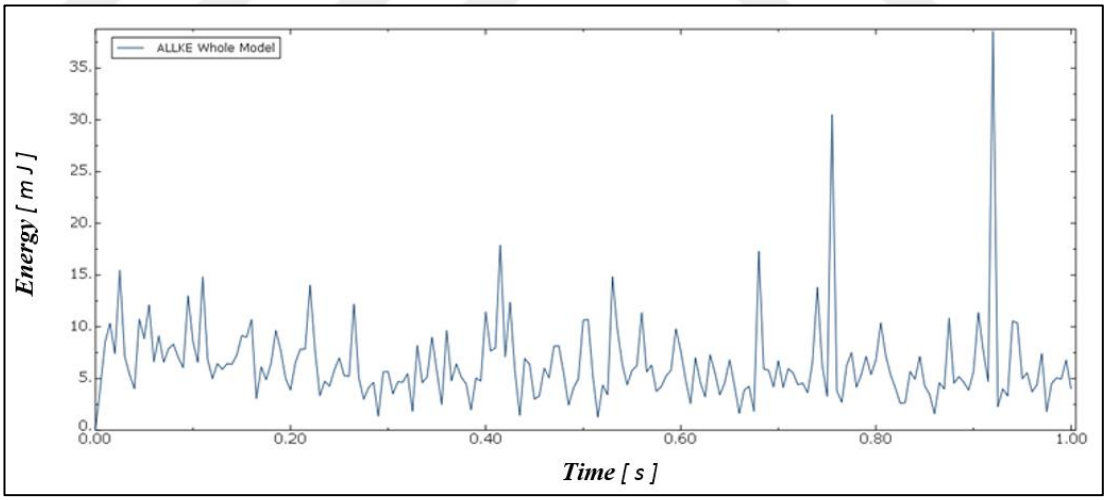


Figure (F.3) Kinetic energy for R=16%

According to the ABAQUS, the energy obtained by integration force and displacement was compared with the external work. The energy 12.6659 kJ was determined by external work Fig. F.4 while the energy 12.7963 kJ was calculated by integration force

and displacement as displayed in Fig. F.5 The convergence between them equal to 99 %.

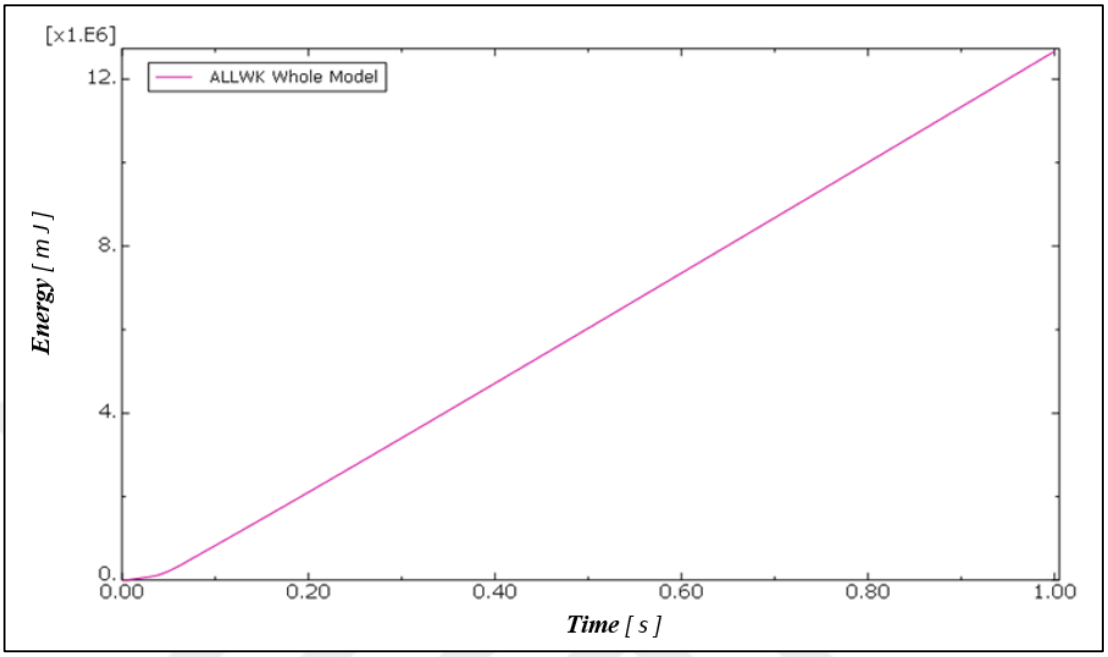


Figure (F.4) External work for R=16%

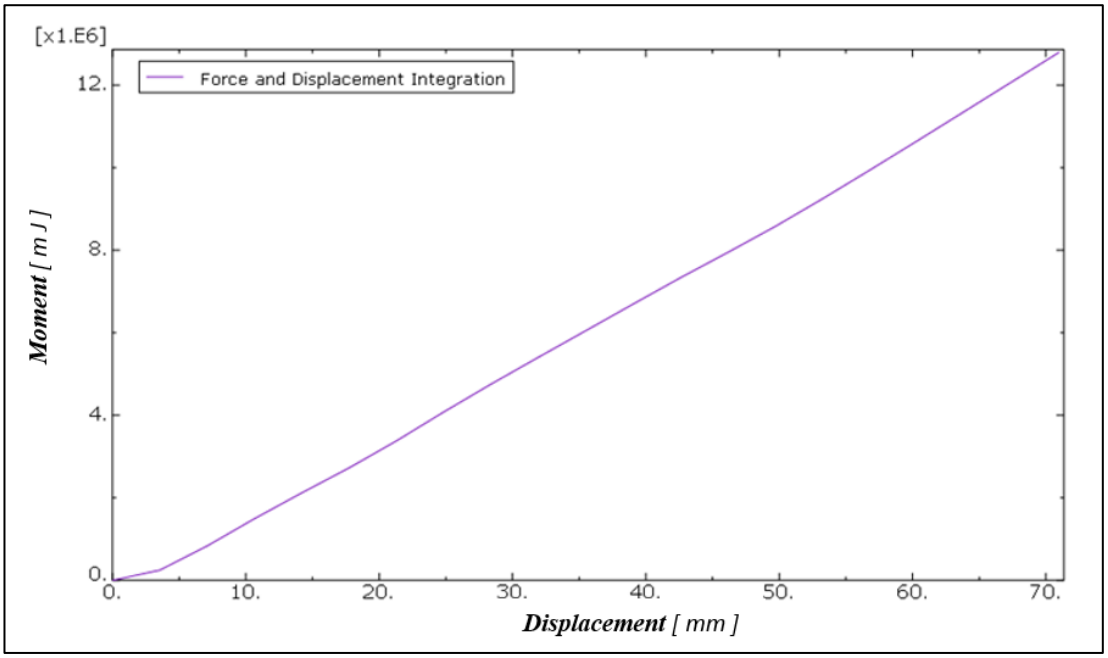


Figure (F.5) Energy obtained by force and displacement integration for R=16%

Energy Output for Tube drawing at R=23%

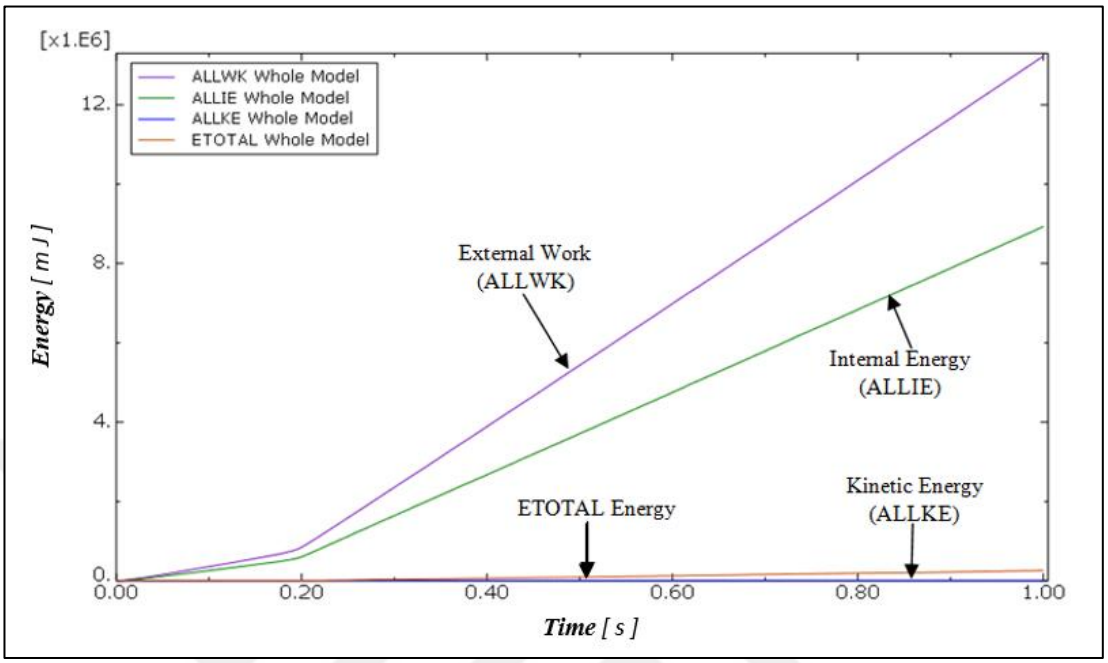


Figure (F.6) Energy output for R=23%

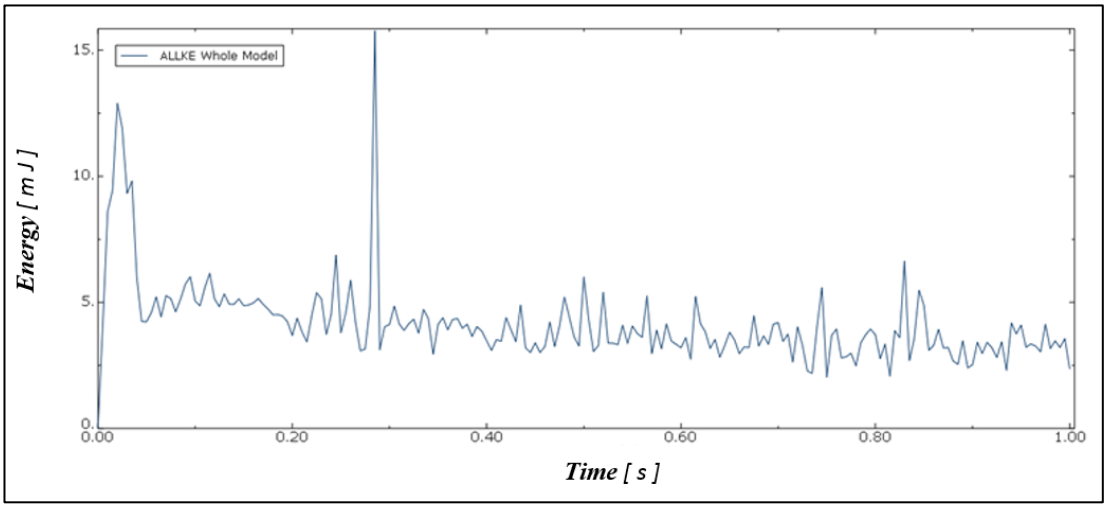


Figure (F.7) Kinetic energy for R=23%

According to the ABAQUS, energy determined by integration force and displacement was also compared with the external work. The energy of 13.32281 kJ was determined by external work as presented in Fig. F.8 while the energy of 13.5176 kJ was calculated

by integration force and displacement as displayed in Fig. F.9. The convergence between them represents 98.5%.

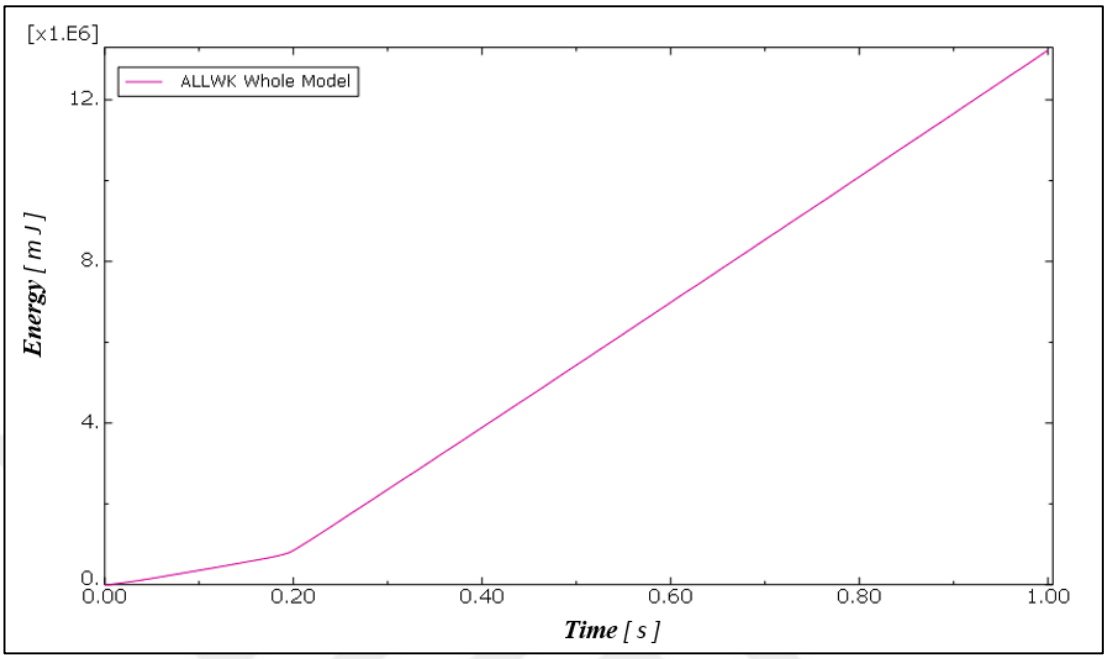


Figure (F.8) External work for R=23%

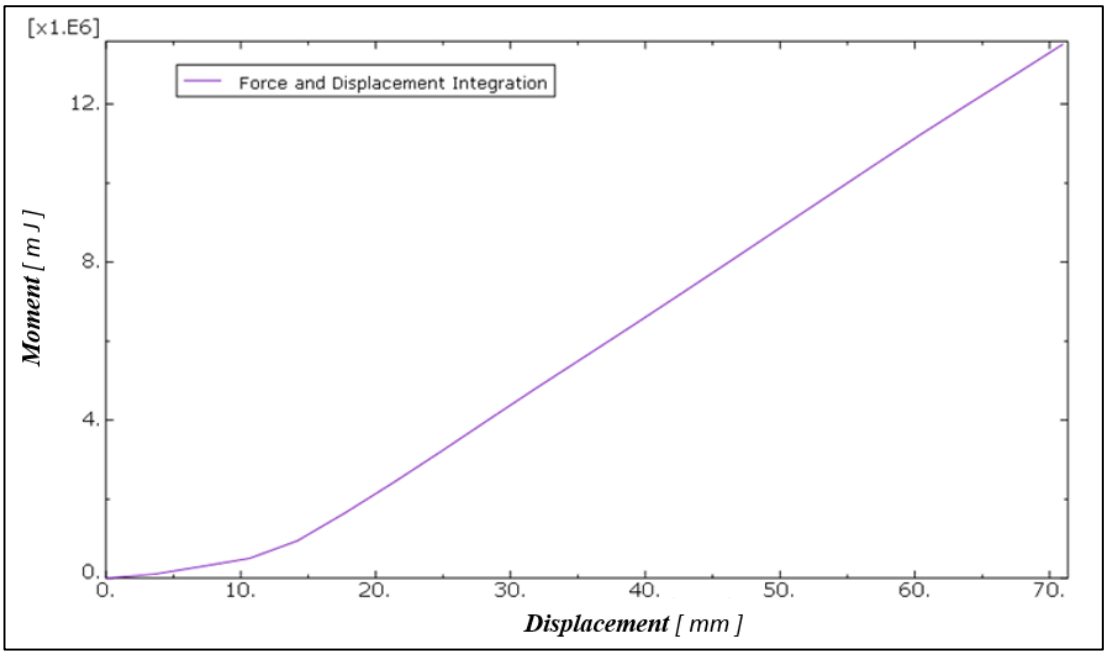


Figure (F.9) Energy obtained by force and displacement integration for R=23%

APPENDIX J - Effect the Velocity on Drawing Force

Fig. G presents the effect of the drawing velocity on the drawing force for R=16%. Because the velocity is very low and drawing displacement 20 mm, the analysis of the model using explicit dynamic needs very long time. So that ABAQUS/ Standard was applied to the analysis of the velocity effect on the drawing force at semi die angle 15°, semi plug angle 0°, and friction coefficient 0.1. From the figure, it can be seen that the drawing force was matched for all velocities. Therefore, the effect of the velocity can be neglected.

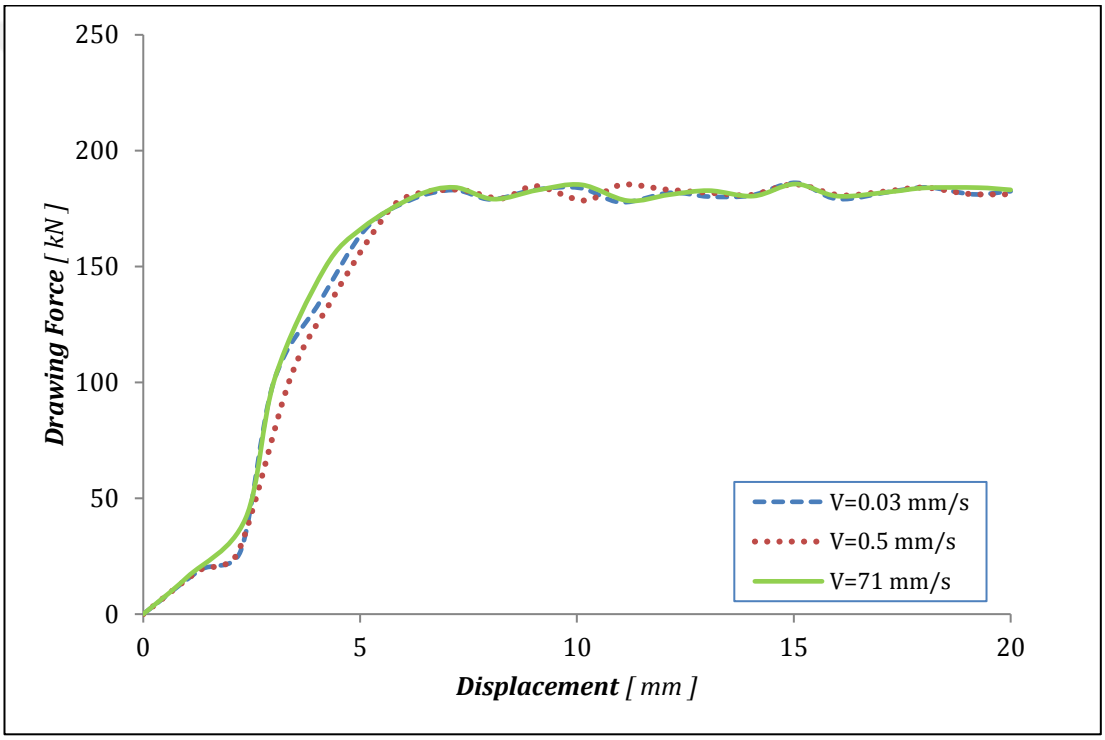


Figure (G) Effect the velocity on drawing force for R=16%

APPENDIX K – External Work Calculations for the Compression Process

The work done or external work is the area under curve as shown in Fig. H.1. It can be calculated by integration of force and displacement.

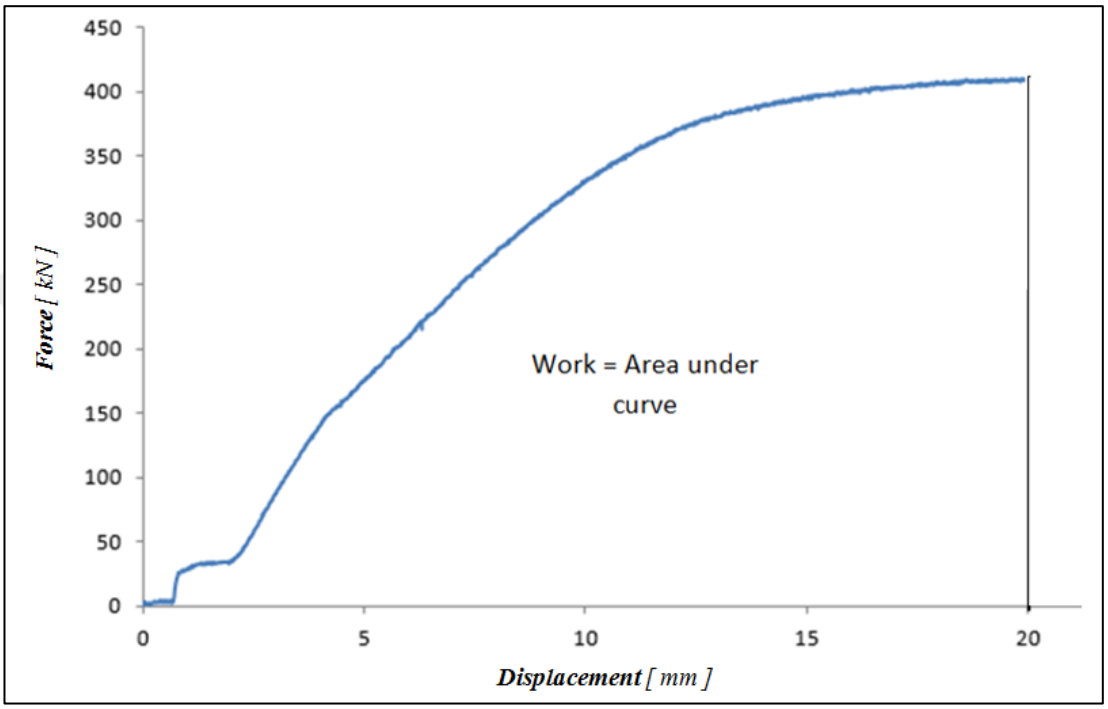


Figure (H.1) Force vs. Displacement of R=16 % obtained experimentally by compression process

Method (1)

Because there are a lot of values that obtained from experimental procedure, five points were selected to determine the external work as reported in table F.

Table (F) Force and displacement values for five point

Force (kN)	Displacement (mm)
F1=0	S1=0
F2=174.9	S2=5
F3=330	S3=10
F4= 396.5	S4=15
F5=409.44	S5=20

$$W = \int_{S_a}^{S_b} F\, ds$$

$$= \int_{S_1}^{S_2} \left(\frac{F_1 + F_2}{2}\right) ds + \int_{S_2}^{S_3} \left(\frac{F_2 + F_3}{2}\right) ds + \int_{S_3}^{S_4} \left(\frac{F_3 + F_4}{2}\right) ds + \int_{S_4}^{S_5} \left(\frac{F_1 + F_2}{2}\right) ds$$

$$W = \left[\left(\frac{0 + 174.9}{2}\right)(5 - 0)\right] + \left[\left(\frac{174.9 + 330}{2}\right)(10 - 5)\right]$$

$$+ \left[\left(\frac{330 + 396.5}{2}\right)(15 - 10)\right] + \left[\left(\frac{396.5 + 409.44}{2}\right)(20 - 15)\right]$$

$$W = 55306\ \text{J} = 5.5306\ \text{kJ}$$

To obtaine more accurate results Microsoft Excel was used to integrate all points and the external work was caclulated 5.3067 kJ.

Method (2)

The second method depends on the equation of the curve. Because there are a lot of values, there is diffculty in the determine the equation of the curve. WolframAlpha mathmtical appliction or Microsoft Excel can be applied to estimate the equation of the curve. In this study, Microsoft Excel was used.

From the Microsoft Excel equation of curve is $F(s) = 21.967(S) + 57.025$

$$W = \int_{S_a}^{S_b} F(s)\, dS$$

$$F(s) = 21.967(S) + 57.025$$

$$W = \int_{0}^{20} (21.967(S) + 57.025)\, dS$$

$$= \left[21.967\left(\frac{S^2}{2}\right) + 57.025(S)\right]_0^{20} = \left[21.967\left(\frac{20^2 - 0^2}{2}\right) + 57.025(20 - 0)\right]$$

$$W = 4393.4 + 1140.5 = 5533.9\ \text{J} = 5.5339\ \text{kJ}$$

Fig. H.2 displays the comparsion between FEM and EXP at R=16% according to the external work. The results show that both of FEM and EXP are close to each other. For FEM the external work is 5.907 kJ and for EXP the external work is 5.530 kJ.

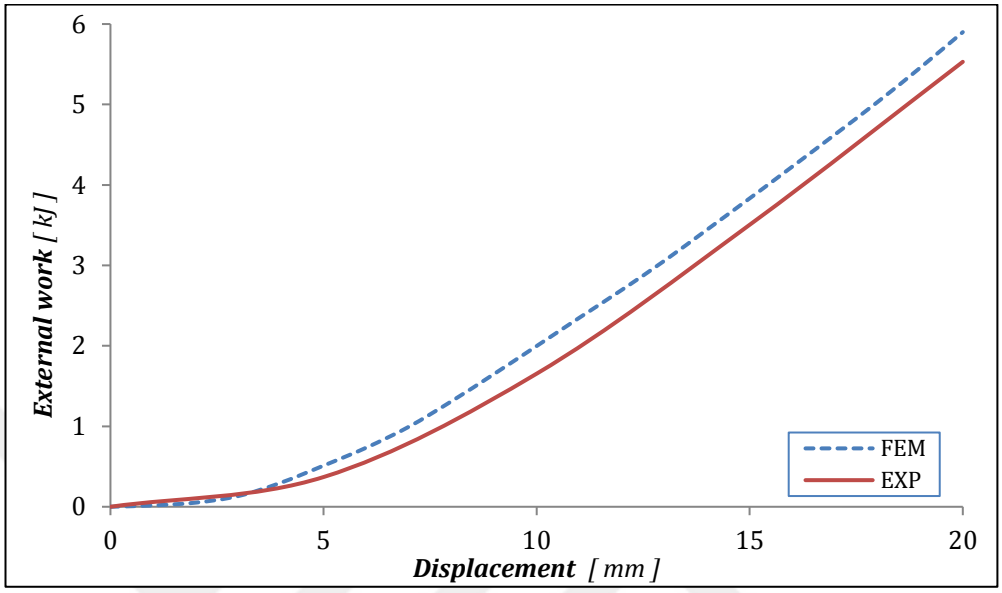


Figure (H.2) Comparsion between FEM and EXP according to the external work at R=16%

Fig. H.3 presents the comparsion between FEM and EXP at R=23% according to the external work. The results show that both of FEM and EXP are close to each other. For FEM the external work is 1.60019 kJ and for EXP the external work is 1.7209 kJ.

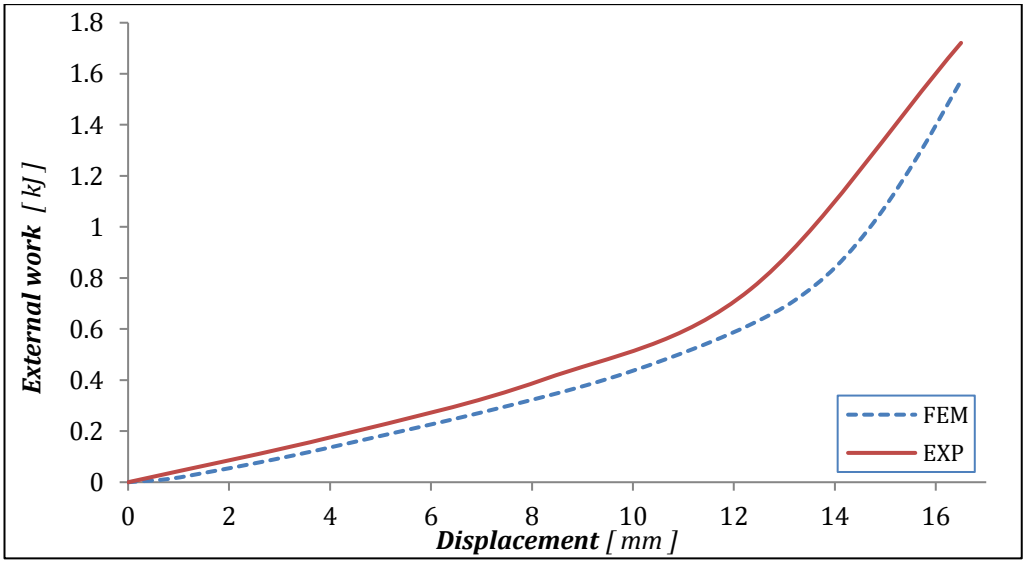


Figure (H.3) Comparsion between FEM and EXP according to the external work at R=23%

CURRICULUM VITAE (CV)

PERSONAL INFORMATION

Surname, Name**:** GATTMAH**,** Jabbar

Nationality: Iraq

Date and Place of Birth: 19 Jun 1974, Diyala

Marital Status: Married

msc_jgj_katma7@yahoo.com

EDUCATION

Degree	Institution	Year
M.Sc.	University of Technology Baghdad	2002
B.Sc.	Technical College Baghdad	1998
Technical Diploma	Technical Institute Baa'quba	1995

WORK EXPERIENCE

Year	Place	Enrollment
2002-2006	Ministry of Communication	Mechanical Engineer
2006-Present	Dialya University/ Mech. Dept.	Lecturer

LANGUAGES

Native Language: Arabic

Foreign Language: English & Turkish

HOBBIES

Traveling, Swimming, computers and internet.